UNIVERSITY OF OKLAHOMA

GRADUATE COLLEGE

CALIBRATING SEISMIC FRACTURE PREDICTION USING BOREHOLE IMAGE LOGS, APPLICATION TO THE MISSISSIPPIAN LIMESTONE

A THESIS

SUBMITTED TO THE GRADUATE FACULTY

in partial fulfillment of the requirements for the

Degree of

MASTER OF SCIENCE

By

STEPHANIE RENEE COOK
Norman, Oklahoma
2016

CALIBRATING SEISMIC FRACTURE PREDICTION USING BOREHOLE IMAGE LOGS, APPLICATION TO THE MISSISSIPPIAN LIMESTONE

A THESIS APPROVED FOR THE
CONOCOPHILLIPS SCHOOL OF GEOLOGY AND GEOPHYSICS

BY

_____
Dr. Kurt Marfurt, Chair

_____
Dr. R. Douglas Elmore

_____
Dr. Matthew Pranter

Dedication

I dedicate this thesis to my husband and very best friend, Bradley Cook, who has been a constant source of love, support, and encouragement throughout the pursuit of my Master's degree and always.

Acknowledgements

I would like to humbly thank Chesapeake Energy for supporting my education and for providing data for this thesis.

Thank you to the ConocoPhillips School of Geology and Geophysics for the opportunity to learn from their excellent geophysics and geology program. I would like to thank Dr. Kurt Marfurt for his geophysical insight, advice, and for his commitment to working with me on this project. I would like to acknowledge Dr. Matthew Pranter and Dr. Doug Elmore for their geological insight and guidance. Thank you to Trey Stearns, Robert Holman, Abdulmohsen Alali, Daniel Costello, Alicia Dye, Amanda and Daniel Trumbo, and Fangyu Li for their technical assistance.

I would also like to acknowledge Schlumberger and Drilling Info for their donation of TechLog, Petrel, and Transform licenses to the University of Oklahoma. The University of Oklahoma's AASPI software was used to generate attributes used in this seismic study.

Lastly, I would like to thank my family for their encouragement throughout the pursuit of my Master's degree.

Table of Contents

List of Figures

Abstract

The Mississippian Limestone of North Oklahoma and Southern Kansas has been one of the more active Midcontinent resource plays of the past decade, with over 4,300 horizontal wells drilled and completed between 2010 and 2015 (IHS). The Mississippian Limestone is a highly heterogeneous reservoir with deposits of not just limestone, but also tripolitic chert, fractured chert, and cherty limestone. The silica rich tripolitic chert found east of the Nemaha Ridge has also been a highly productive drilling target in small portions of the study area. These highly porous tripolitic chert mounds were formed during the early Pennsylvanian uplift with subaerial exposure and diagenetic alteration of the porosity. However, with sporadic vertical production from the more ubiquitous non-porous limestone, it became clear that fracturing is a major driver of production in this reservoir.

Seismic amplitude, attributes, and impedance are often used to map faults, folds, and areas of greater porosity. However, fractures are rarely seen on seismic data. In this thesis I develop a work flow to differentiate more fractured from less fractured areas of the reservoir from 3D surface seismic using five horizontal image logs. I use a sixth image log to validate my prediction.

The strike of fractures in the borehole images confirms the east-west compressional stress regime common to northern Oklahoma. With the uplift, subaerial exposure, and diagenetic alteration of the Mississippian Limestone in early Pennsylvanian time, karsting occurred and is prevalent throughout the area as well, with evidence of karsting interpreted in the borehole image logs.

Of the 18 attributes evaluated, envelope, density, variance, certain dip azimuth angles, frequency, and most negative long wavelength curvature correlated best with fracture intensity measured by the image logs. I used multivariate nonlinear regression statistics to use these attribute volumes to predict fractures throughout the survey. The resulting fracture intensity model shows increased fracturing in areas know to contain tripolitic chert, increased fracturing in areas of faulting, and increased fractures in areas with heavy karsting.

Correlating oil production with the resulting fracture intensity model is more problematic, with inclusion of variable production and engineering parameters necessary to make an accurate prediction.

Chapter 1: Introduction

The Mississippian Limestone has been an exploited reservoir in the mid-continent since 1919 in Osage county (Bosworth, 1920), first producing from the reservoir with vertical wells in structural traps. The increase in horizontal drilling in the early 21st century has revitalized the Mississippian Limestone play in southern Kansas and northern Oklahoma. The Mississippian Limestone is a non-porous heterogeneous cherty limestone that accumulated on a shelf margin. With uplift and subaerial exposure during early Pennsylvanian time, diagenetic altering of the chert left highly porous targets in tripolitic chert mounds found sporadically in the study area. Fracturing can occur not only during subaerial exposure, but also during burial and hydrothermal alteration of the Mississippian Limestone (Young 2010). During diagenetic alteration in this time of uplift, karsting occurred in the study area. Manger (2014) attributes fracturing to diagenesis of chertier lithologies, with many of the fractures associated with shrinkage.

With only a small percentage of the study area covered by tripolitic chert, understanding fracture porosity of the large cherty lime and fractured chert lithologies is essential for infill and further drilling programs. Not only does diagenesis contribute to fracturing of this heterogeneous formation, but tectonic deformation does as well. With east-west compression in the study area, strike slip faults are prevalent along with pop-up structures.

Several recent studies have examined the lithology and fracturing of the Mississippian Limestone. Lindzey (2015) used the same seismic data in Woods County, Oklahoma, as this survey, used well logs and seismic impedance inversion to

generate a 3D geomodel over the study area to map lithology, porosity, and water saturation. Lindzey (2015) found that greater amounts of tripolitic chert and higher porosity were associated with faults seen on the seismic data. She hypothesized that fracturing in the seismically incoherent, faulted areas allowed for fluid flow causing diagenetic alteration. Lindzey (2015) also found that vertical wells in the study area produced from tripolitic chert zones, while horizontal wells were able to also produce from stimulated cherty limestone. Working in Kay County, Oklahoma, Turnini (2015) found that mounds of positive curvature could be used to find tripolitic chert. However, Turnini could not find a direct correlation between tripolitic chert thickness and oil production, indicating other factors play a role in production, such as water production. Further north in Kay County, Oklahoma, Trumbo (2014) was able to predict tripolitic pay to seismic attributes such as impedance inversion. However, older wells did not record water production, handicapping his production calibration. Trumbo (2014) did find a strong visual correlation of production with structural lineaments. He hypothesized that the low oil production from thicker chert adjacent to major faults was due to excessive water production.

There have been several fracture studies east of the Nemaha Ridge in the Mississippian Limestone. Stearns (2015) found that curvature was a good measure of fractures due to structural deformation, but was not able to identify areas of fractures that were generated by a mechanism other than strain. Holman (2014) used multivariate non-linear statistics to predict fractures in the interpreted Mississippian horizon. He was able to successfully correlate complex trace attributes with fracture intensity, but found that fracture intensity correlated opposite of geological reasoning for geometric

attributes such as coherence and curvature. Working in Osage County, White (2013) found that the main driver of predicting fractures was based off lithology, with enhancement from curvature attributes (Figure 1).

This study includes a seismic survey that spans 264 square miles of the expansive midcontinent shelf margin in Woods and Alfalfa counties, Oklahoma, five borehole image logs, well data from 32 vertical and 55 horizontal wells, as well as scaled production data (Figure 2). With the use of well logs and interpreted seismic horizons, seismic attribute volumes are then depth converted using average velocity models. Next, I interpret fractures at the wellbore on five borehole image logs, and upscale them to 110 ft bin size. The seismic attributes extracted along these five boreholes will then be correlated to fractures with the use of multivariate non-linear regression statistics. The combination of correlative attributes will then be used to extrapolate fracture prediction throughout the seismic survey. Finally, the resulting fracture intensity model will be compared with the horizontal Mississippian production. I conclude with analysis of whether fracturing in the Mississippian Limestone is controlled by diagenetic alteration, tectonic deformation, or both and discuss the limitations of correlation with fracturing and production.

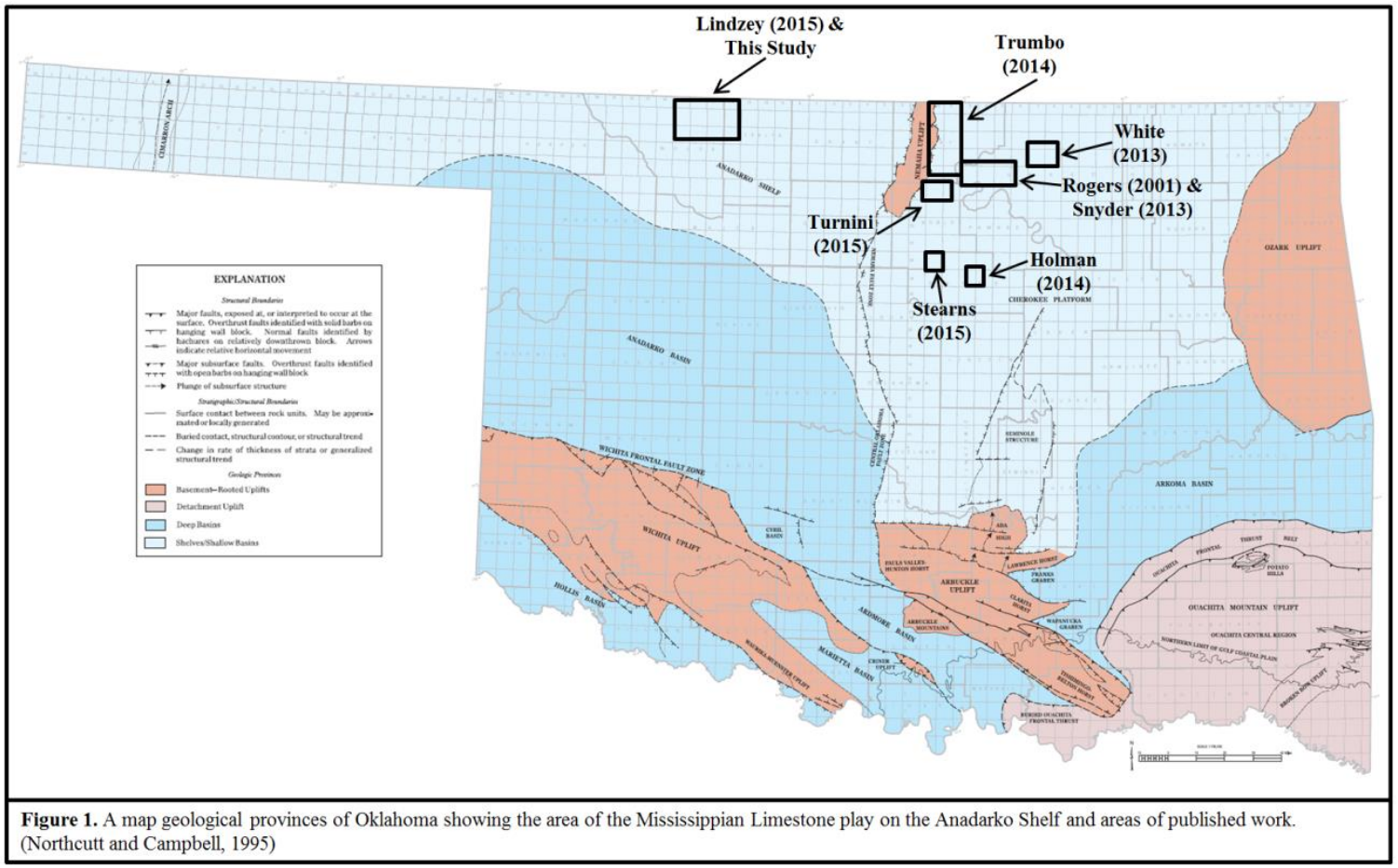

Figure 1. A map geological provinces of Oklahoma showing the area of the Mississippian Limestone play on the Anadarko Shelf and areas of published work. (Northcutt and Campbell, 1995)

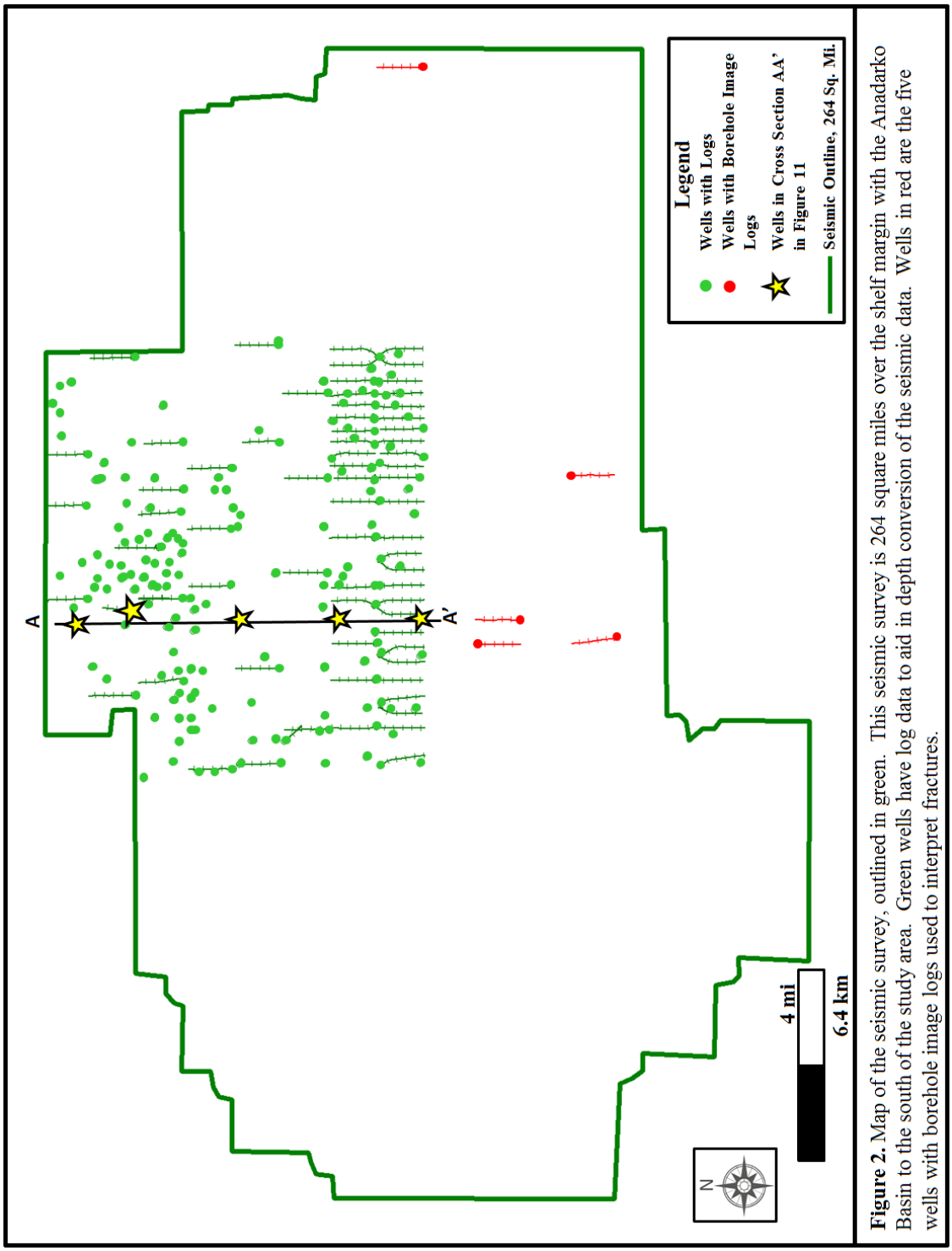

Figure 2. Map of the seismic survey, outlined in green. This seismic survey is 264 square miles over the shelf margin with the Anadarko Basin to the south of the study area. Green wells have log data to aid in depth conversion of the seismic data. Wells in red are the five wells with borehole image logs used to interpret fractures.

Chapter 2: Geologic Background

The Mississippian Limestone, deposited on a continental shelf margin approximately 360 to 320 million years ago (Figure 3), is composed of four main intervals: the Kinderhookian, Osagean, Meramecian, and Chesterian. These intervals contain limestone, some tripolitic chert, cherty limestone, and some shale in the deepest Kinderhookian interval (Watney et al., 2001). Lindzey (2015) created a type log using a cored and logged well in the study area (Figure 4), and found the Chesterian interval to be absent in the study area, subcropping south of the seismic survey.

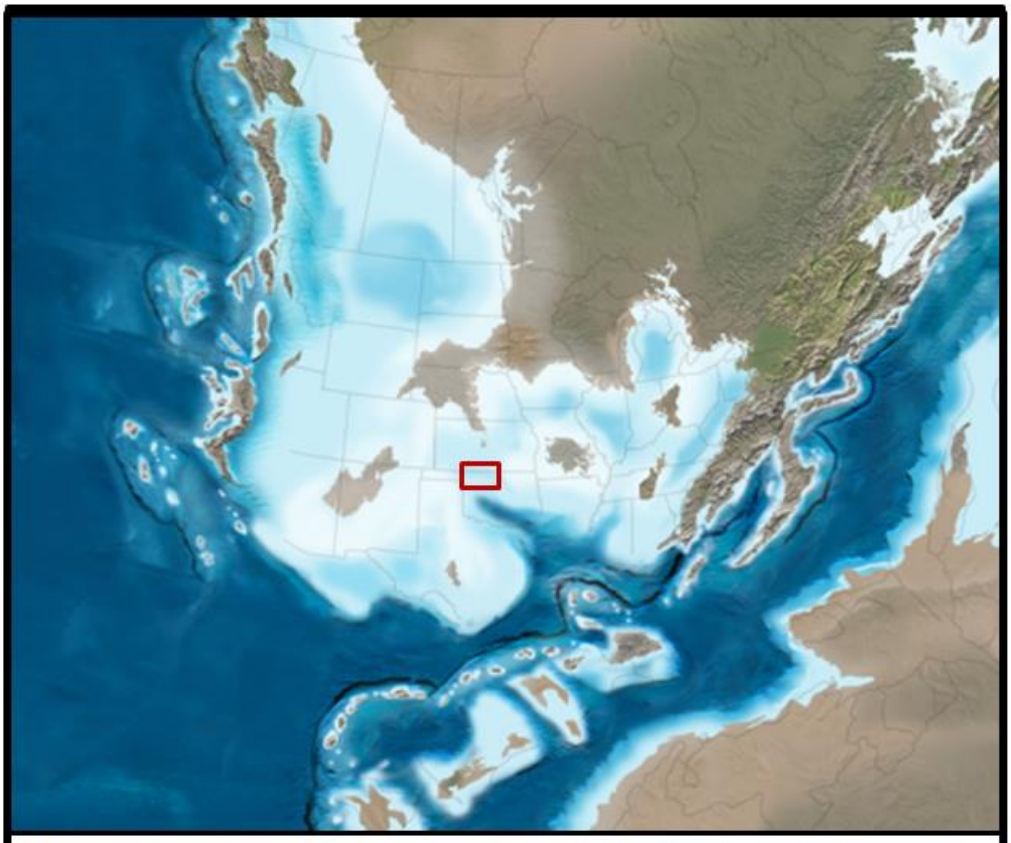

Figure 3. A map of the study area, highlighted in the red box, which lies on the shelf margin of the Anadarko Basin in Mississippian time. Paleogeography map is adopted from Blakey (2014).

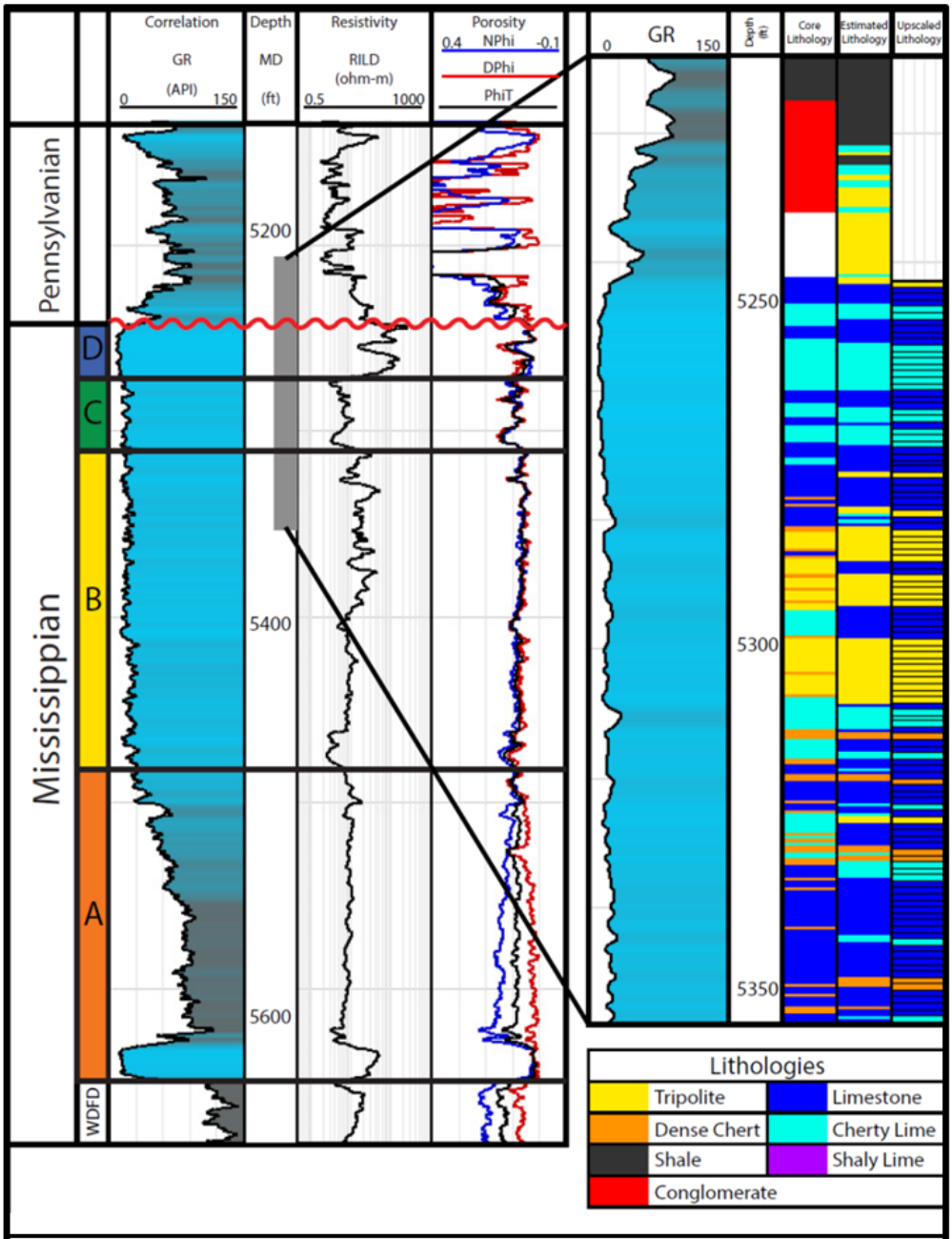

Figure 4. Lindzey (2015) created a type log of the study area using a cored and logged well to illustrated the Mississippian intervals in the study area. The grey bar is the cored interval, with her detailed lithology findings. The Gamma Ray, Deep Resistivity, Neutron Porosity, Density Porosity, and Total Porosity log responses are shown.

During Mississippian time, the present mid-continent was at 20º south latitude and was covered by a well oxygenated, shallow sea. The sea underwent transgressive, regressive cycles, which created a stratal geometry that is interpreted as shallowing upward sequences (Witzke and Bunker, 1996). There are four stacked transgressive-regressive cycles of progradation in the Mississippian section, and these four stacked sequences make up a third-order transgressive-regressive cycle bounded with an unconformity above and below (Manger, 2011). The Mississippian Limestone was located on a shelf margin that sloped into the Anadarko Basin, towards a deep seaway, which had a merging plate boundary (Scotese, 1999). This plate boundary may have released volcanic emissions that provided the source of silica (Watney el al., 2001). The main shelf is a quiet depositional environment, as seen in the Kansas Osagean cherts (Pharham and Northcutt, 1993). Further south in our study area, on the shelf margin, sponge-spicule facies and bioherms were deposited (Thomas, 1982 and Rogers et al., 1995). These spiculitic chert mounds were consolidated, in-situ, internally brecciated sponge and bioherm mats (Rogers et al., 1995). Outside of these sponge-spicule mounds, limestone and cherty limestone were deposited. Chat beds, an informal name for beds of high porosity producing chert, which makes a chattering noise when drilled, were not found further south (Rogers et al., 1995). However, above wave base, some spiculite components were transported due to erosion (Rogers and Longman, 2001). There is cherty limestone in deeper sections of the Mississippian. Chert nodules are seen in limestone, due to silica in the limestone developing in-situ chertification (Pharham and Northcutt, 1993).

With drops in sea level and subaerial exposure, the spiculite mounds were weathered and diagenetically altered (Figure 5). During this time of subaerial exposure, precipitous water led to karsting, including caverns and solution-channel features (Parham and Northcutt, 1993). During the Ouachita collisional, faulting created the Kansas uplift (Figure 6). This extended period of uplift and subaerial exposure created the Mississippian-Pennsylvanian unconformity (Montgomery, et al. 1998). The Pratt anticline (Figure 6), which extends from the Kansas uplift, caused much of the upper portion of the Mississippian chat to be eroded (Watney, et al., 2001).

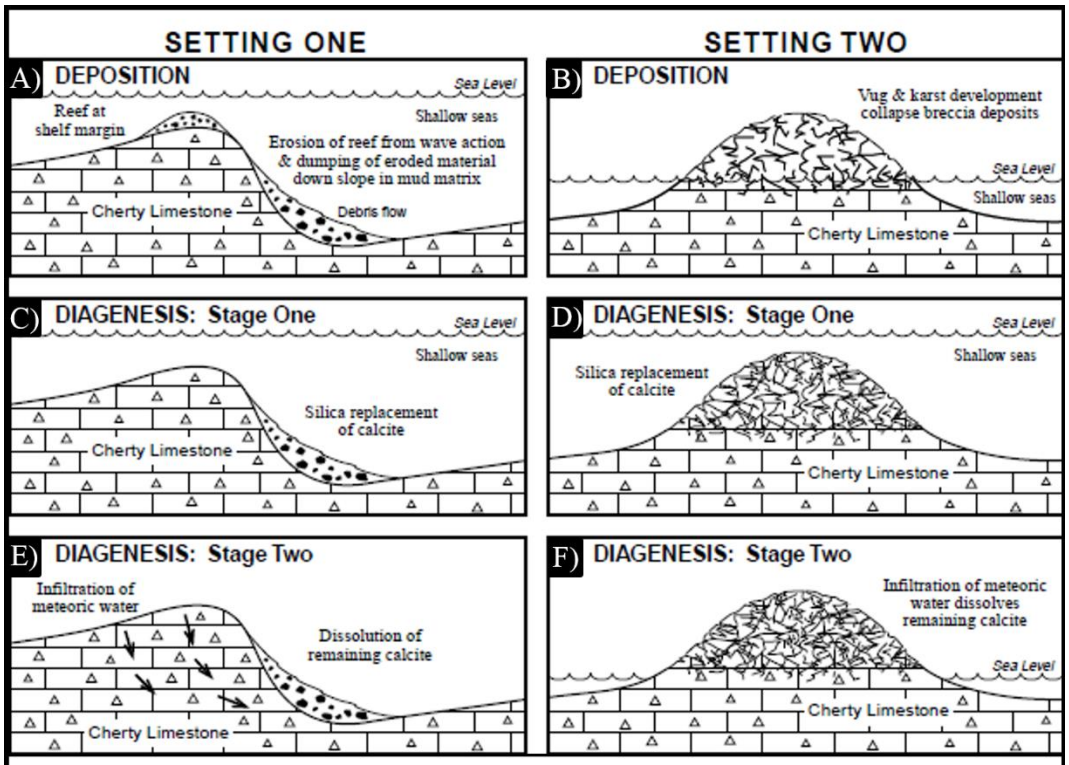

Figure 5. Rogers (2001) illustrates two methods of chert replacement in cherty Limestone. Setting one illustrates transported tripolite down slope and then dissolution of the remaining calcite. Whereas, setting two illustrates in-situ silica replacement with subaerial exposure. Setting two creates vug and karsting features.

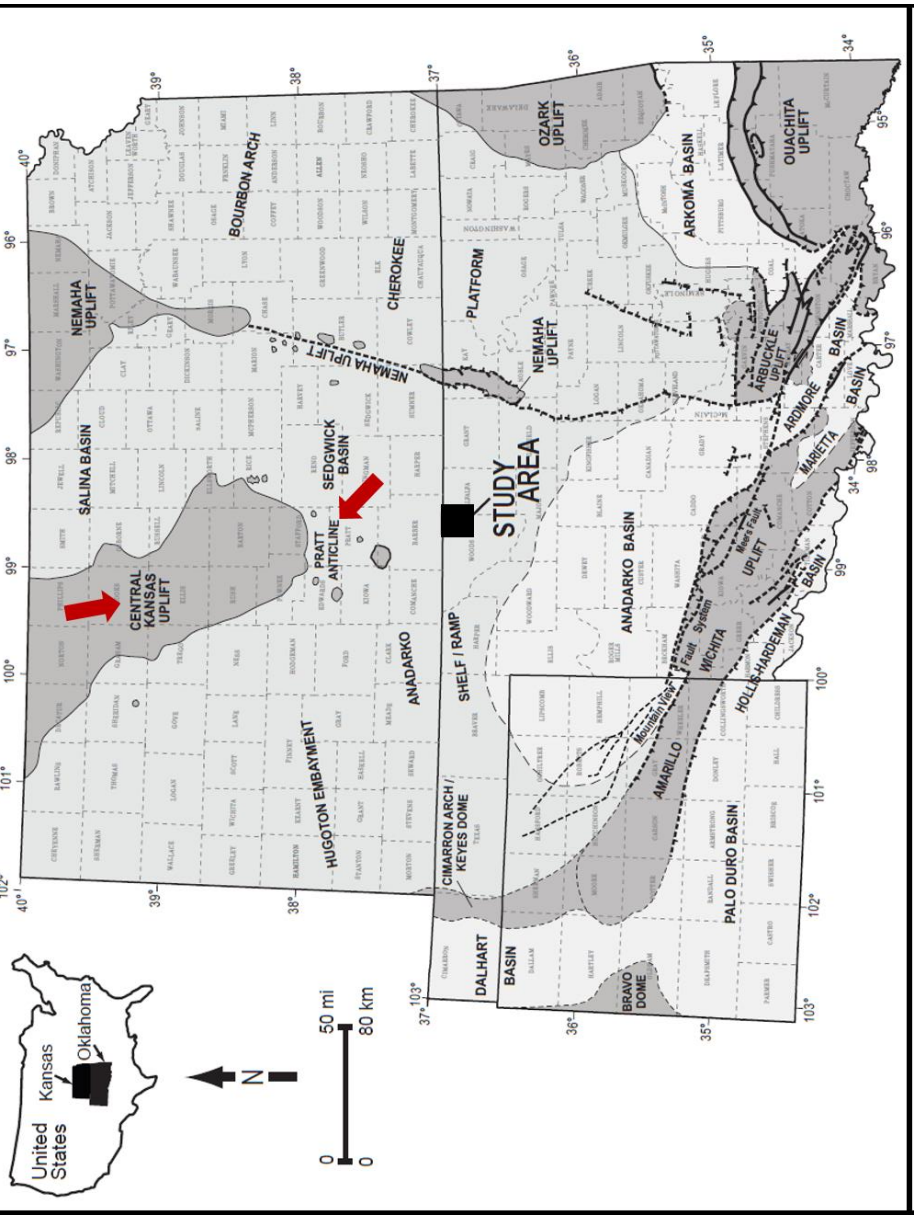

Figure 6. Map of tectonic provinces of Oklahoma and Kansas. The Central Kansas Uplift and the Pratt Anticline are highlighted here, and discussed in the geologic background, page eight. The study area, which lies on the Anadarko shelf margin, is also highlighted in northern Woods and Alfalfa counties. (modified from Lindzey, 2015)

After deposition, the Mississippian went even more diagenesis. Tripolitic chert was the result of dissolution of fossils and volcanic ash (Montgomery et al., 1998). The volcanic ash was silica rich and the dissolved silica precipitated in pore spaces and replaced carbonate fossils on a molecule by molecule basis (Rogers, 2001). This diagenesis occurred just below the sea floor before induration (Manger, 2011). Chert

precipitation, oil migration, and calcite cementation occurred, possibly as a result of hot brine pulsing out of the Anadarko Basin due to structural deformation in the basin (Goldstein and King, 2014). Uplift during early Pennsylvanian time resulted in further subaerial exposure and another occurrence of diagenesis, creating moldic porosity (Montgomery et al., 1998). In some areas there was so much dissolution of carbonate, that vugs formed (Rogers, 2001). Vuggy porosity was seen in areas along the borehole image logs used in this study (Figure 7). Tripolitic chert in the study area resides in these areas that had secondary diagenesis (Montgomery et al., 1998). Hydrocarbon accumulation can occur in this diagenetically altered rock either in structural traps or in stratigraphic traps with the Cherokee Shale overlying the porous diagenetically altered reservoir (Rogers et al., 2001).

Studying outcrops, Mazzullo et al. (2011) found that fracturing in the Mississippian Limestone was dependent on lithology, with fracturing occurring in the more brittle chert and limestone lithologies, and less so in shaley limestone. Fracturing in the Mississippian can be caused by either tectonic deformation or with diagenetic alteration of the rock. Diagenesis of the chert and cherty limestone as described above could contribute to fracture intensity in the chert and cherty limestone lithofacies (Manger 2014). Manger highlights shrinkage fractures from de-watering along the Bella Vista Roadcut in Arkansas (Figure 8), which is a deeper portion of the Mississippian Limestone from the tripolitic chert. In this deeper section of pen contemporaneous chert, the diagenetic sequence begins with opal-A, a siliceous ooze, to opal-CT, a porcelanite, to quartz chert (Manger 2014). Young (2010) found that fracturing in the Mississippian occurred due to diagenesis during subaerial exposure

that occurred during uplift and erosion, burial, and hydrothermal alteration post burial. Trumbo (2014) speculated fracturing in the Mississippian contributes to intermittent production in vertical wells in reservoirs with no matrix porosity. Stearns (2015) found that fractures are correlated to curvature, in brittle rocks, but not in ductile rocks.

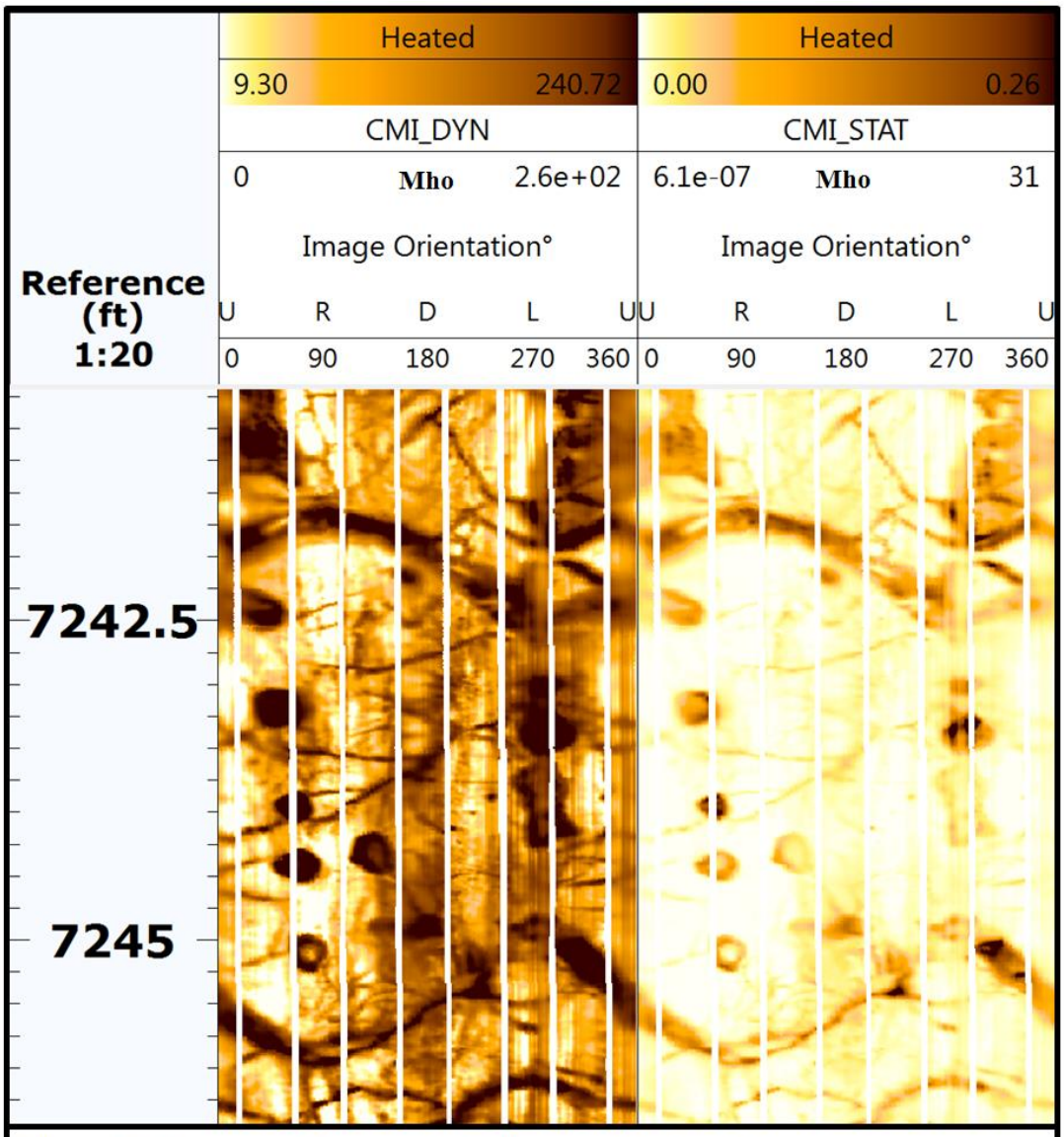

Figure 7. A representative example of diagenetically altered Mississippian Limestone seen in borehole image logs used in this study. This is an example of the vuggy porosity described by Rogers' (2001) setting two, in-situ diagenesis (Figure 5).

Figure 8. An outcrop illustrating diagenetic changes resulting in chert, along with example of shrinkage fractures from de-watering. This is the Lower Boone section of the Mississippian at the Bella Vista Roadcut, Arkansas (Manger, 2014).

Chapter 3: Seismic Interpretation and Depth Conversion

The seismic reflections are measured in two way travel time while the horizontal borehole image logs are measured in depth. In order to correlate the two, I converted the seismic volume to depth, using well log tops, interpreted seismic, horizons, and average velocity models. Such conversion allows the extraction of seismic attributes along a wellbore measured in depth.

Wells with both sonic logs and density logs were used to generate acoustic impedance curves which in turn were used to create a synthetic seismogram to correlate the seismic data with the borehole data. I used the Walden/White method to others since it does not assume the trace at the well is the best correlation to the log; rather it identifies the better trace near the wellbore for correlation. The Walden/White method also does not assume the phase to be constant through all of the frequencies (Walden and White, 1998).

18 wells containing sonic and density logs and were tied to the seismic data (Figure 9).

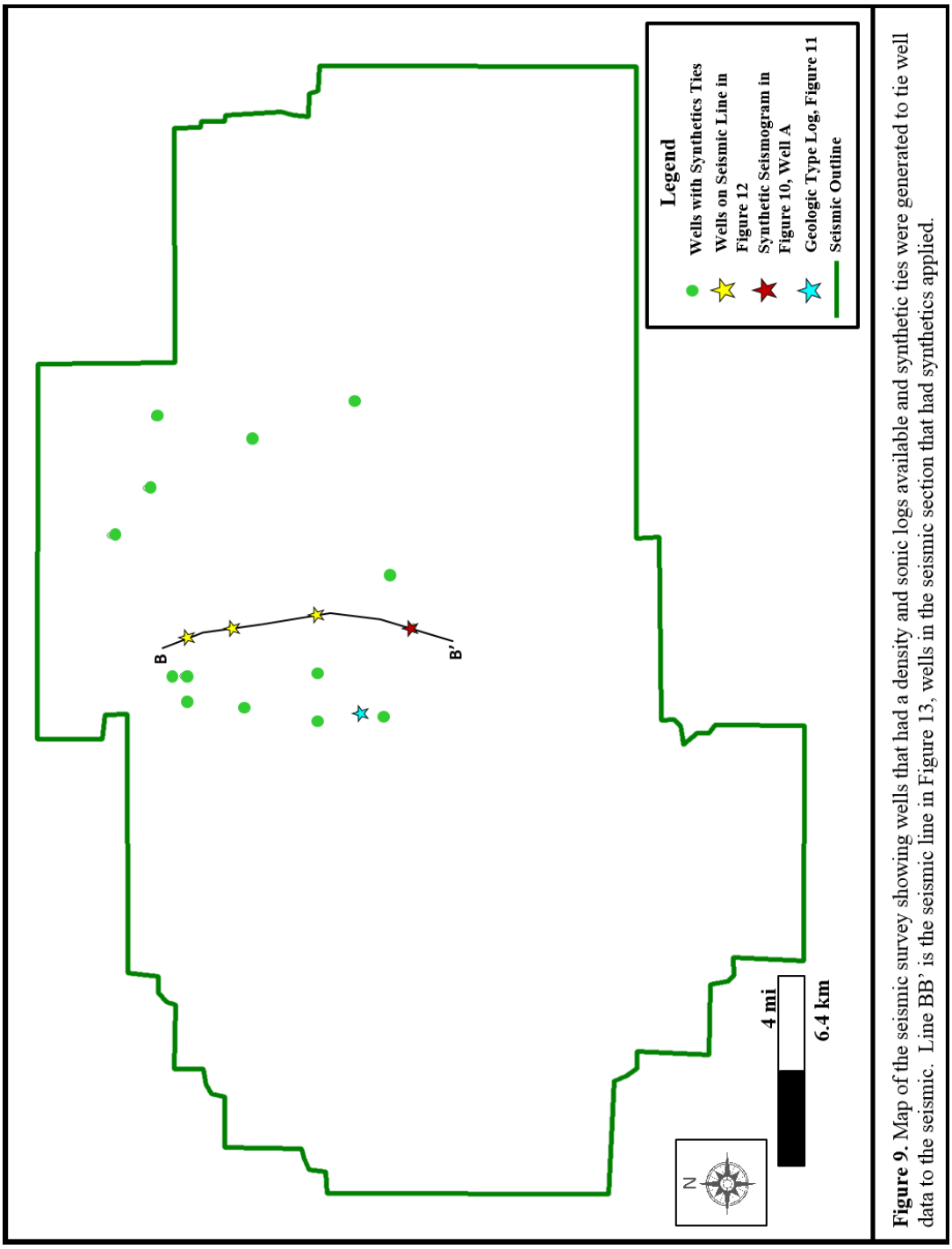

Figure 9. Map of the seismic survey showing wells that had a density and sonic logs available and synthetic ties were generated to tie well data to the seismic. Line BB' is the seismic line in Figure 13, wells in the seismic section that had synthetics applied.

The correlation between the wellbores and the synthetic model were exceptionally good, requiring minimum time shifting, stretching and squeezing of the well logs (Figure 10). The result of the synthetic work was a suite of 18 time to depth curves which allowed correlation of the well top picks to a peak, trough, or zero crossing of the seismic data, used to interpret these surfaces away from the wellbore.

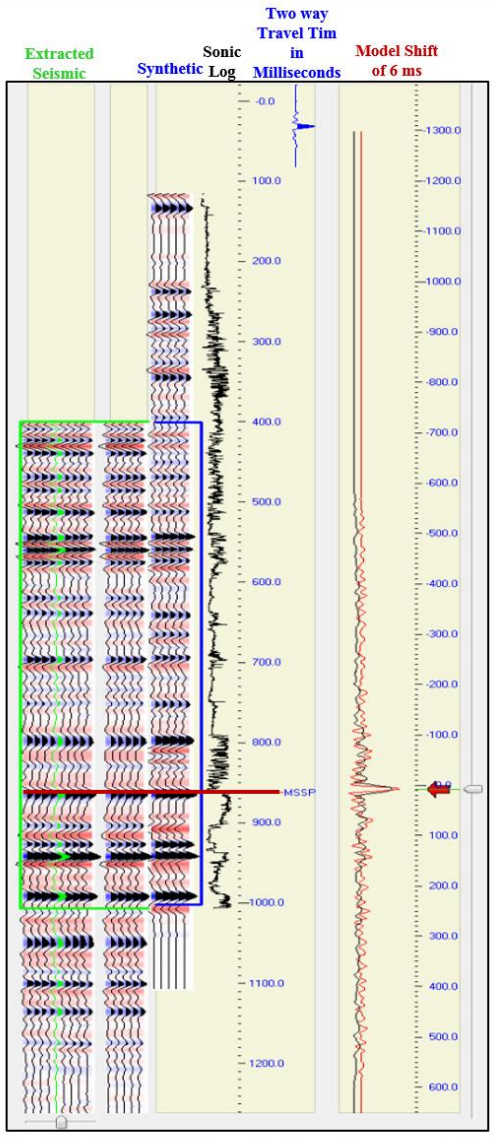

Figure 10. Well tie to seismic for Well A (in Figure 9), shows the extracted seismic, the synthetic seismogram using the Walden/White method, the sonic log, and the slight shift of the model by 6 milliseconds. The top of the Mississippian Limestone is indicated by the red line and this well to seismic tie has a correlation coefficient of 0.8078.

For an accurate depth conversion of the entire Mississippian Limestone formation, both a shallower and deeper formation tops needed to be interpreted as well. I used the top of the shallower Lansing Limestone formation, and the top of the deeper Woodford Shale formation, the latter which forms the base of the Mississippian Limestone. The Lansing Limestone is overlain with shale and lies above the Kansas City Limestone. I defined the top of the Lansing Limestone formation as an interface of the shale and limestone, where the gamma ray had high values before it transitioned to the lower values of the carbonates. Log responses to the formations interpreted are illustrated on Figure 11, with a type geologic section, created from the well highlighted on Figure 9. The Mississippian Limestone also is overlain by shale, the Cherokee Shale's such that the Mississippian formation top was interpreted at the point where the gamma ray went from high values in the shale to lower values in the carbonate. The Woodford Shale lies just below the Mississippian Limestone and its formation top was interpreted just below low gamma ray values of the Mississippian Limestone and on top of the high gamma ray values of the Woodford shale, accompanied by a slight lowering of the density log values in the Woodford Shale. The vertical section shown in Figure 12 shows how the Mississippian Limestone becomes thicker to the south.

These three formation tops were interpreted on the seismic volume, with the shallower and deeper formations interpreted more accurately depth convert the Mississippian. The Lansing Limestone, overlain by a thick bed of slower shale results in a high amplitude peak throughout the seismic. The Mississippian Limestone, overlain by the Cherokee Shale, results in a peak as well. Lastly, the interface between

the Mississippian Limestone and the slower Woodford shale below, results in a high amplitude trough throughout the seismic data volume (Figure 13).

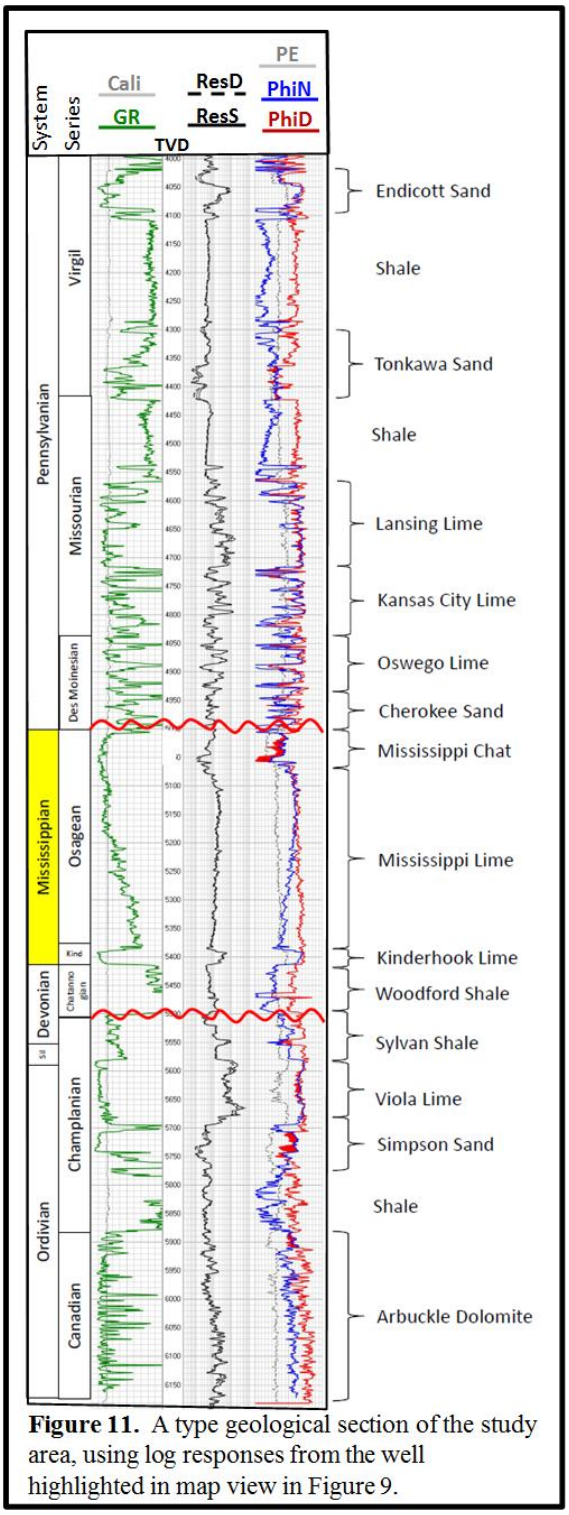

Figure 11. A type geological section of the study area, using log responses from the well highlighted in map view in Figure 9.

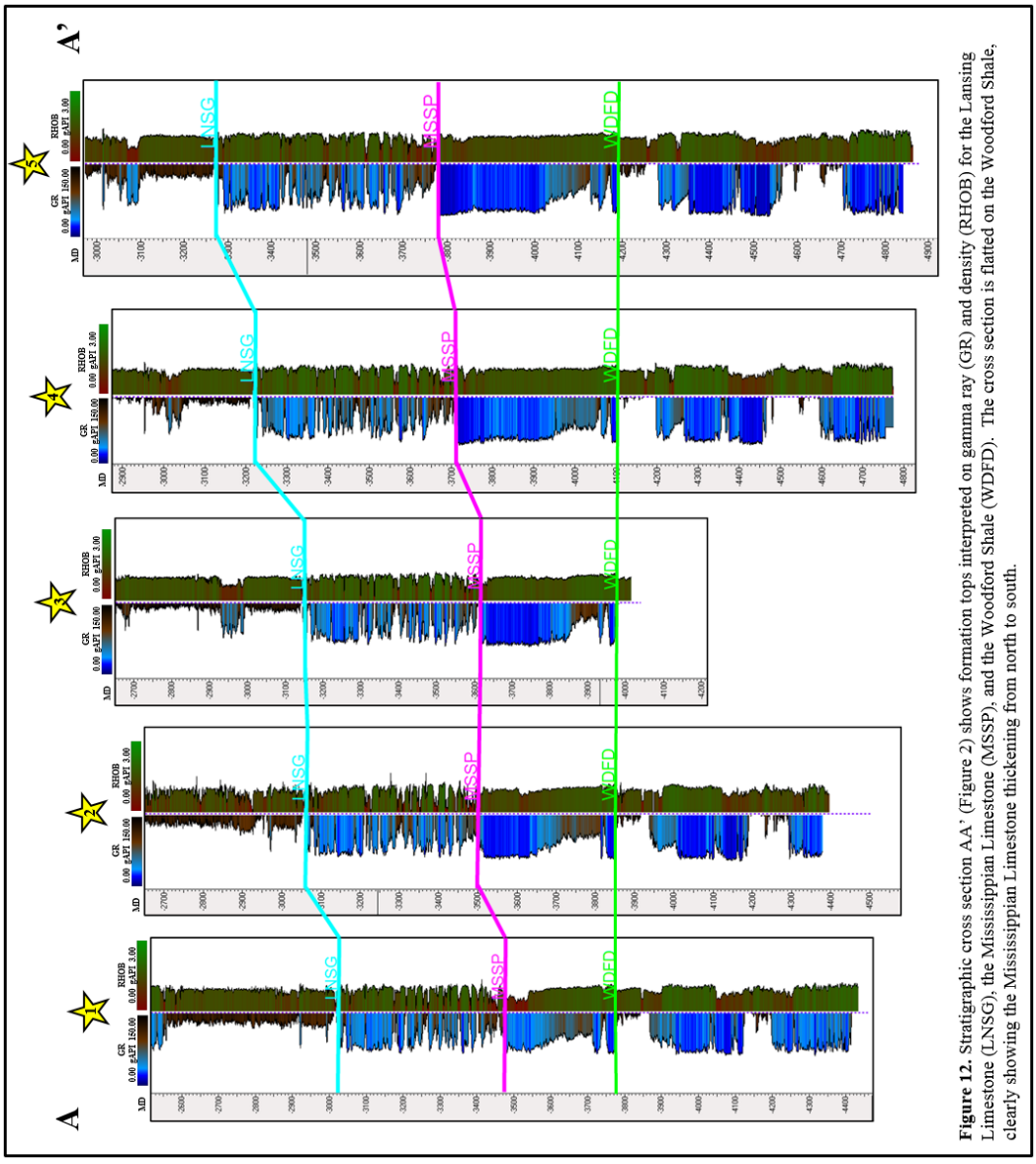

Figure 12. Stratigraphic cross section AA' (Figure 2) shows formation tops interpreted on gamma ray (GR) and density (RHOB) for the Lansing Limestone (LNSG), the Mississippian Limestone (MSSP), and the Woodford Shale (WDFD). The cross section is flatted on the Woodford Shale, clearly showing the Mississippian Limestone thickening from north to south.

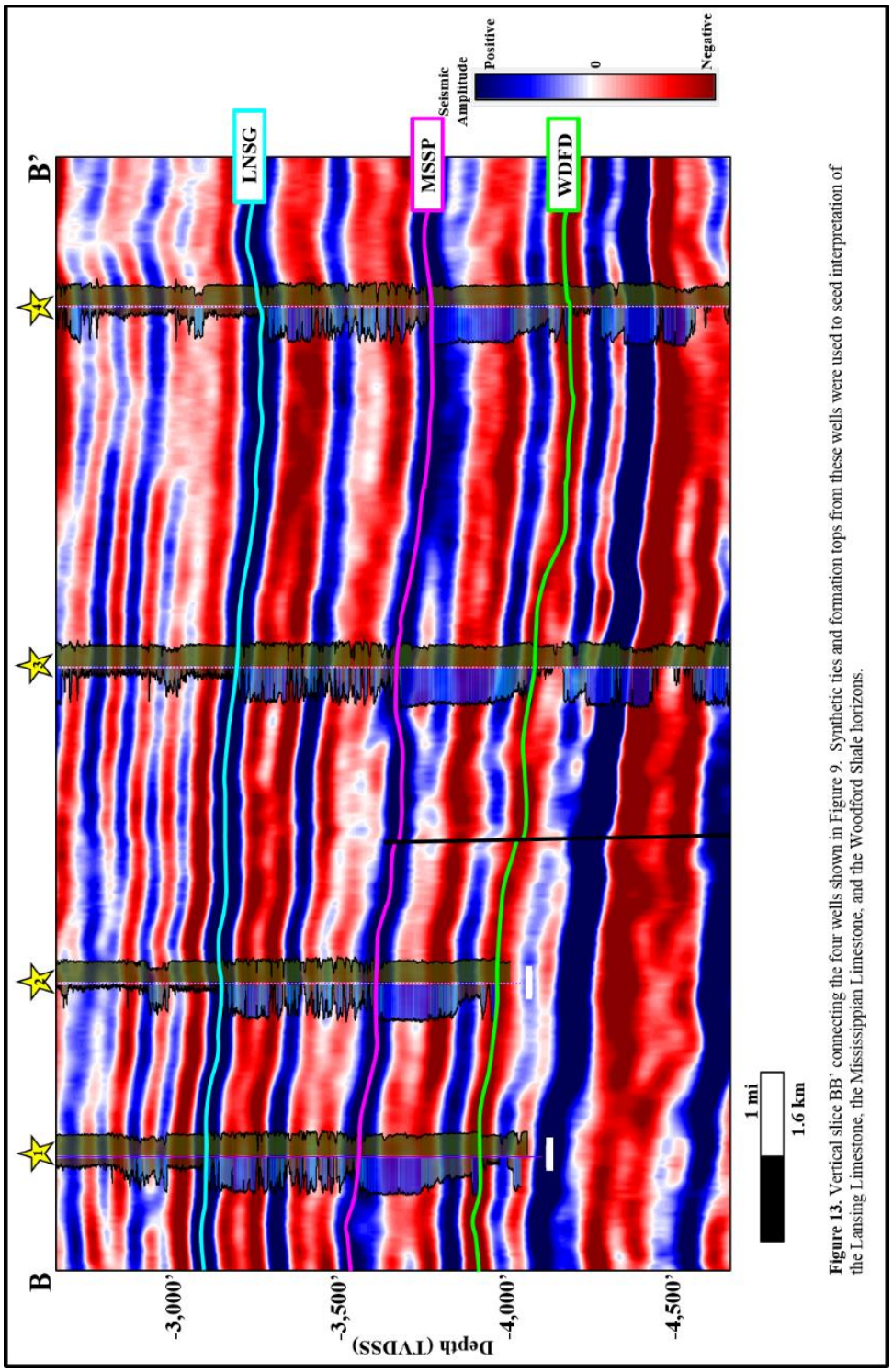

Figure 13. Vertical slice BB' connecting the four wells shown in Figure 9. Synthetic ties and formation tops from these wells were used to seed interpretation of the Lansing Limestone, the Mississippian Limestone, and the Woodford Shale horizons.

With formation tops interpreted in depth and seismic horizons interpreted in time, an average velocity model was generated for the surface to the top of the Lansing Limestone, from the Lansing Limestone to the top of the Mississippian, and from the top of the Mississippian Limestone to the top of the Woodford Shale (Appendix A1). Due to their greater depth and age, each interval has a faster average velocity than the one above. Using these average velocity models, I converted the seismic from time to depth, as well as the three interpreted surfaces.

The Lansing Limestone is shallower in the northern portions of the seismic survey and deeper in the south, ranging from 2,900 ft subsea to 3,700 ft subsea (Appendix A2). The top of the Mississippian Limestone also increases in depth (Figure 14) and thickness to the south (Appendix A3). One of the major structural features of the Mississippian Limestone in this seismic survey is a major left lateral strike slip fault FF' (Figure 15) that runs from the northeast corner of the survey all the way to the southwest corner with upthrow to the northwest and down throw to the south east. A reverse fault RR' extends from the north central extents of the survey and runs north-south, extending south of the first strike slip fault described. A strike-slip fault GG' is seen in southeastern portion of the survey. Finally, a pop-up feature, originates in the basement, lies in the center of the survey (Figure 16). The initial faulting in the survey is late Mississippian in age with reactivation of faults post Mississippian; offsets of the large northeast-southwest fault can reach up to 100 ft.

Examining the major faults throughout the survey from the deeper structure map of the Woodford Shale up through the Mississippian Limestone and the Lansing Limestone, the structural features of the faults and the pop up feature have less offset as

you make your way up shallower through the section. The Woodford Shale (Appendix A4) has dramatic faulting, and plunges down to 4,900’ subsea in the southern extents of the seismic survey.

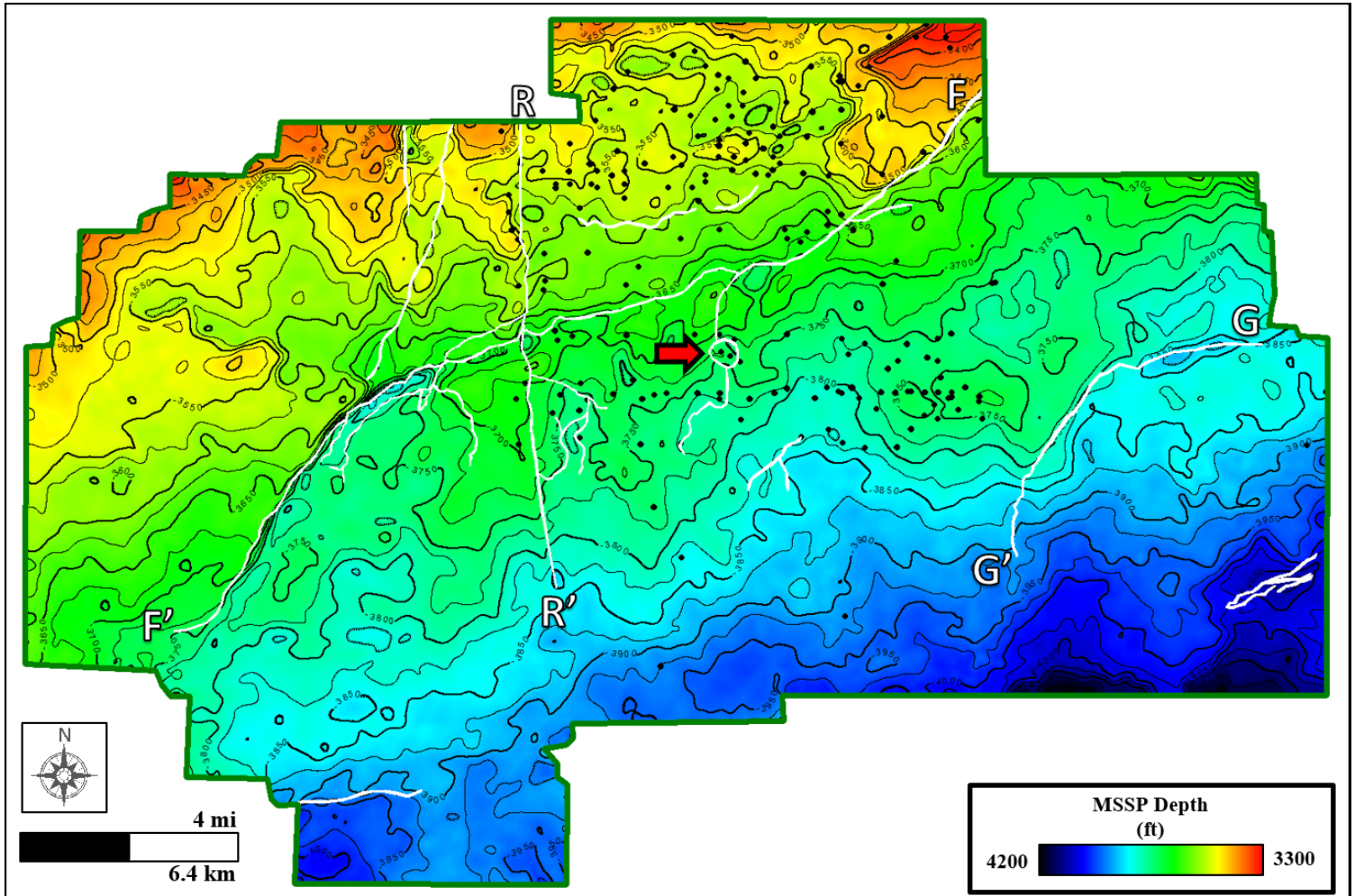

Figure 14. Depth converted structure map of the top of the Mississippian Limestone, picked on seismic amplitude and then depth converted with formation top picks and an average velocity model, with 50 ft contour intervals. The structure map shows the Mississippian Limestone deepens to the south and is cut by three main faults. A pop up structure in the center of the survey is highlighted with a red arrow.

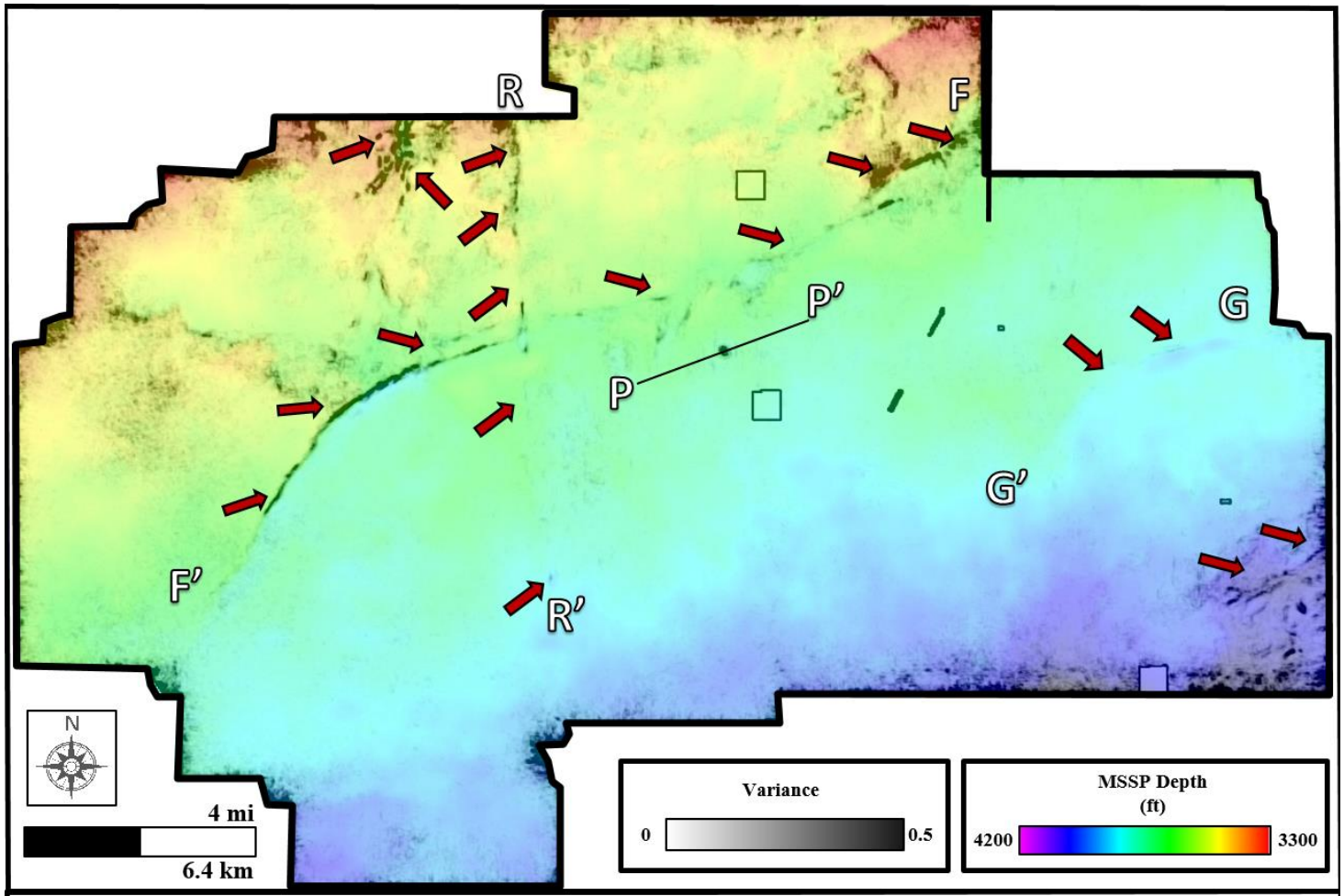

Figure 15. Depth converted structure map of the top of the Mississippian Limestone, co-rendered with variance extracted along the top of the Mississippian Limestone. Variance, a similar algorithm to coherence, compares the waveforms of neighboring traces in the seismic amplitude and highlights major structural features of the seismic survey, including faults and pop-up features. The pop-up feature can be seen in the vertical seismic section PP' in Figure 16.

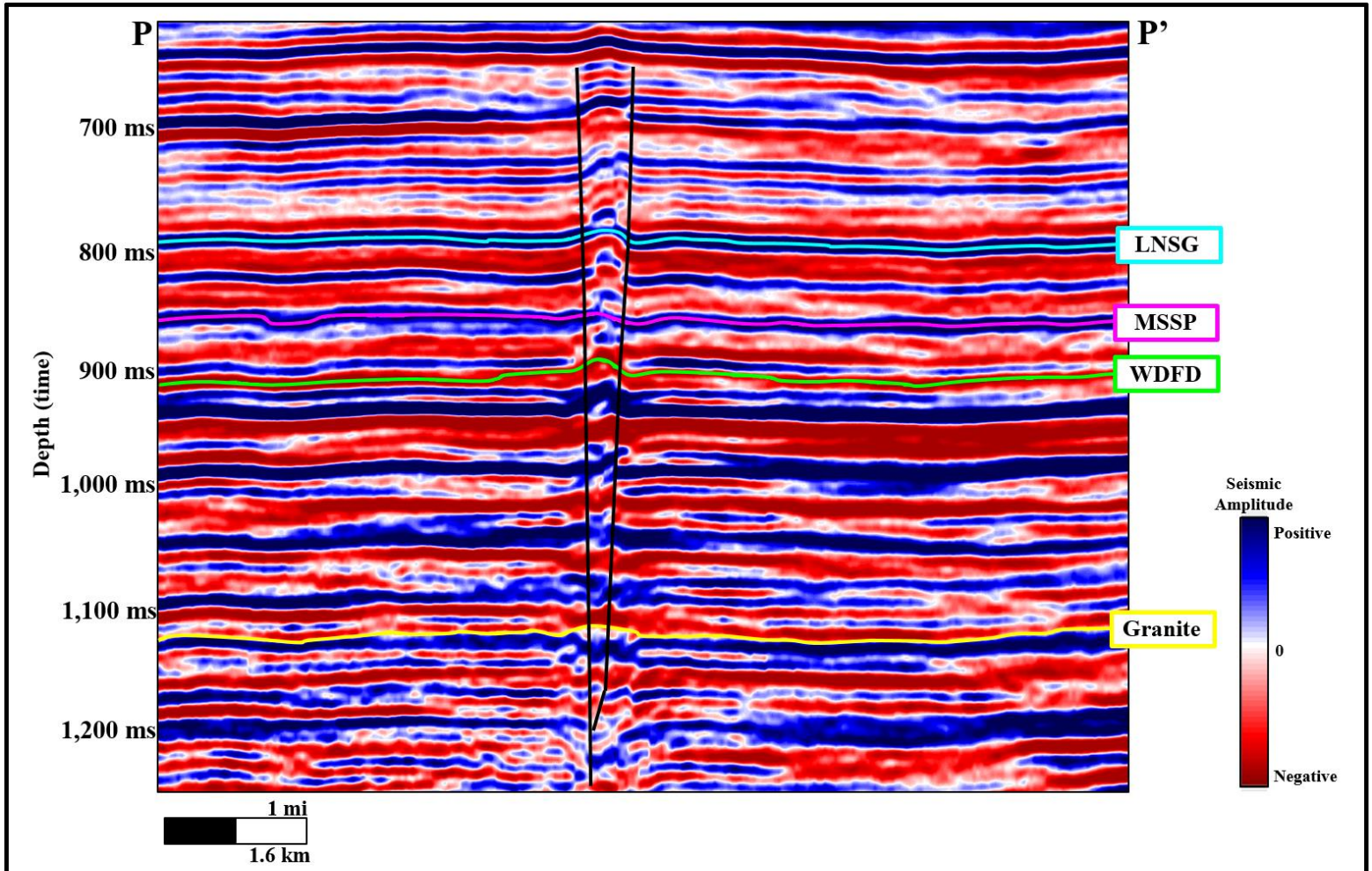

Figure 16. PP' shows the pop-up structure which lies in the center of the survey. The granite is interpreted based off a well in the survey that contains a sonic and density log that penetrates into the granite of the geologic basement. The pop-up feature can be seen in the seismic vertical section from below the geological basement, up through formations shallower than the Lansing Limestone.

Chapter 4: Borehole Image Interpretation

FRACTURES

Electrical borehole images from electrical borehole imaging tools are in effect superior dip meters. Imaging tools have a complex array of electrodes on 8 pads, in this study, that press against the borehole wall. Electrical current is released into the borehole wall and the electrodes measure the current after it has examined the rock. As a result, you get an electrical picture of rocks and fluids confronted by a wellbore (Hurley, 2004). Five borehole images were interpreted for open, conductive fractures. During borehole image interpretation both open, conductive fractures and mineralized, non-conductive fractures were observed. In order to model open, conductive fractures; the output from the borehole image interpretation was open, conductive fractures only.

The open, conductive fractures were interpreted as fractures that had a higher measured resistivity up against the lower resistivity measured from the surrounding chert or limestone. This appears as a darker colored plane against its lighter surrounding matrix. This higher resistivity reading was from the drilling mud that was able to penetrate into the fracture plane. Much of the borehole image logs were highly fractured with open, conductive fractures. Interpretation of conductive fractures was done with a full sinusoid for fractures that cut through the entire borehole and partial fractures were also used to interpret fractures that only cut through a portion of the borehole (Figure 17 and Figure 18). Stereonets were generated for fractures that penetrated the entire borehole. The strikes of these fractures were east northeast – west southwest. Some of the fractures were partially conductive and partially mineralized. This was seen with a halo effect surrounding the fracture and a higher resistivity

through the center of the fracture. In this case, a partial fracture was interpreted only through the conductive portion of the fracture.

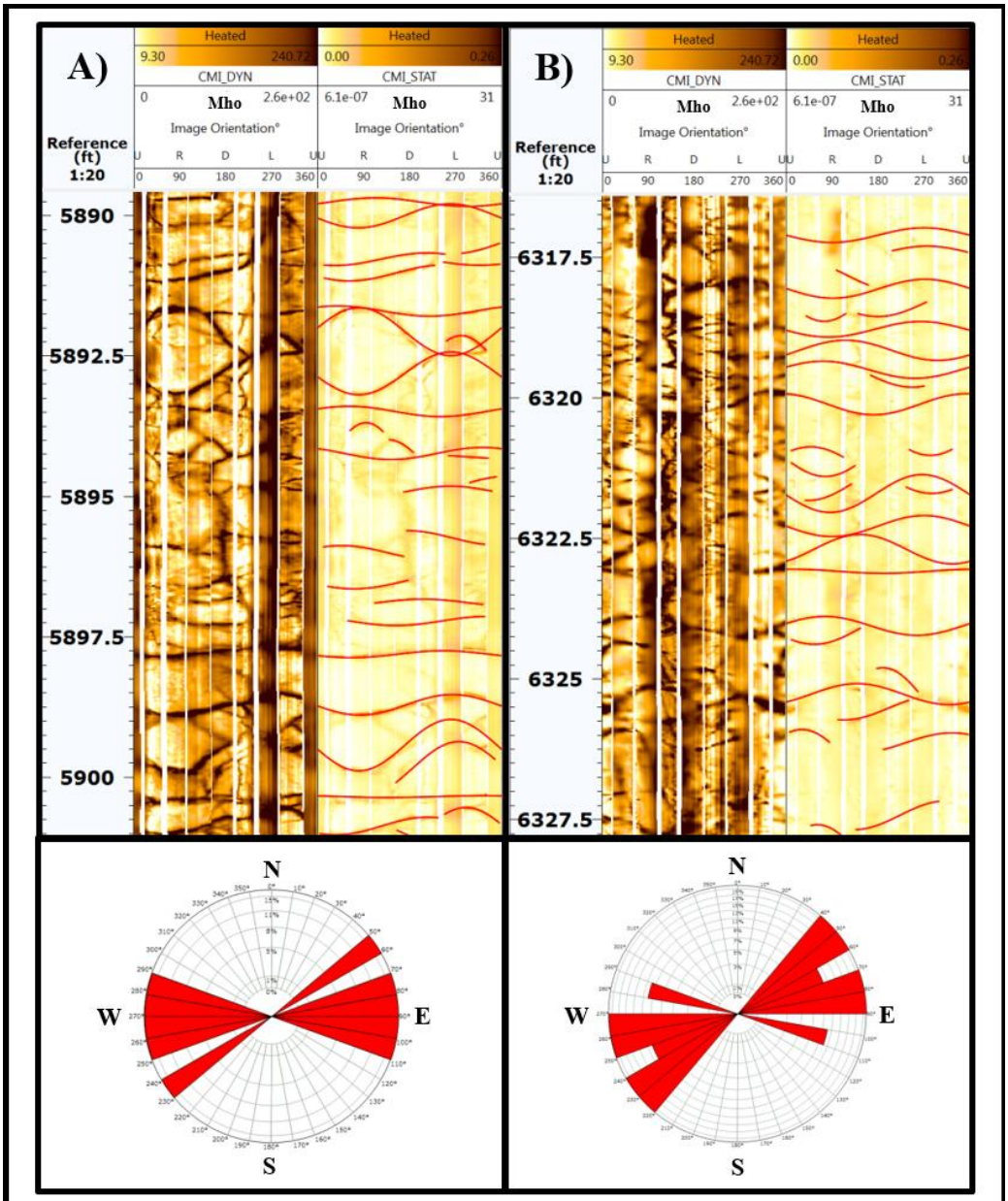

Figure 17. Examples of conductive fractures seen in a horizontal well where drilling mud filling the fracture planes is seen as a dark brown (high conductivity) against the lighter colors (lower conductivity) of the limestone. Orientation of the image is indicated by up (U), right (R), down (D), and left (L) of the well circumference. The stereonets below the track show the strike of the fractures that cut through the entire borehole.

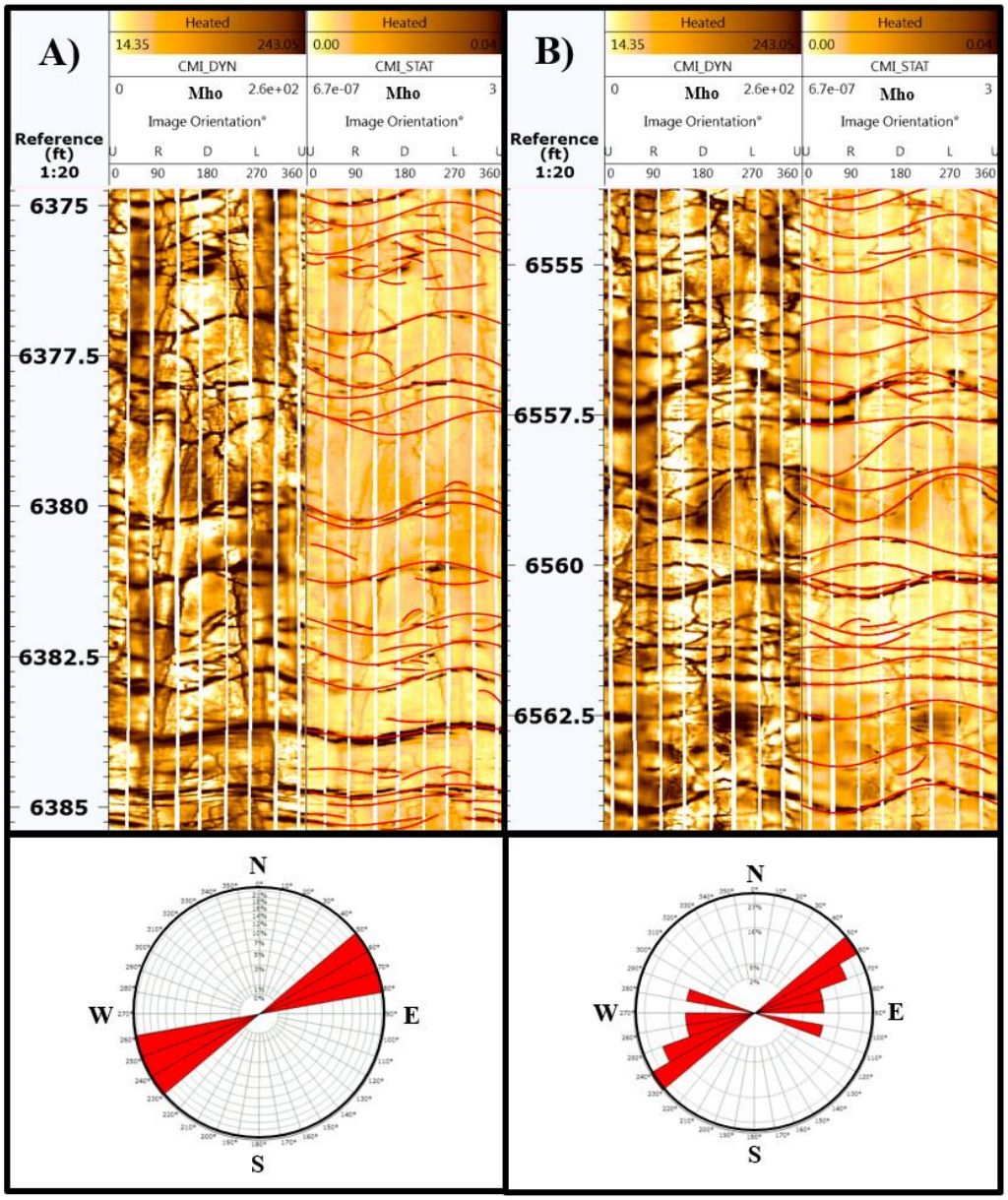

Figure 18. Examples of conductive fractures where drilling mud filling the fracture plane appears as darker brown colors against a lower, lighter color, limestone. The stereonets below the track show the strike of the fractures that cut through the entire borehole.

A non-conductive, mineralized fracture is nevertheless less non-conductive than the surrounding chert and limestone and appears lighter (Figure 19 and Figure 20). There were far fewer non-conductive fractures seen in the five borehole images. Stereonets were generated for non-conductive fractures, which exhibited similar east northeast to west southwest strike directions as the conductive fractures. Examples of both conductive and non-conductive fractures are shown in Figures 17 through 20. However, only the conductive fracture interpretations were used as an input to the fracture model.

Drilling induced fractures were also present in much of the borehole images. These fractures ran perpendicular to the natural fractures in the horizontal wellbore (Figure 21) and are often described to look like "railroad tracks". Drilling induced fractures often provide an estimate of the maximum principle horizontal stress direction; west – east in the study area. In areas of strike slip faulting, faults trend ±30° from maximum horizontal stress (Figure 22, Zoback, 2016). Most of the faulting in the study area runs -30° from the west – east maximum horizontal stress seen in induced fracturing. It would be expected for natural fractures to strike in a similar orientation to the faulting, considering with the compressional horizontal stress, the rock fails at that orientation, parallel to faulting. Both natural fracturing and faulting strike -30° from the west – east maximum horizontal stress.

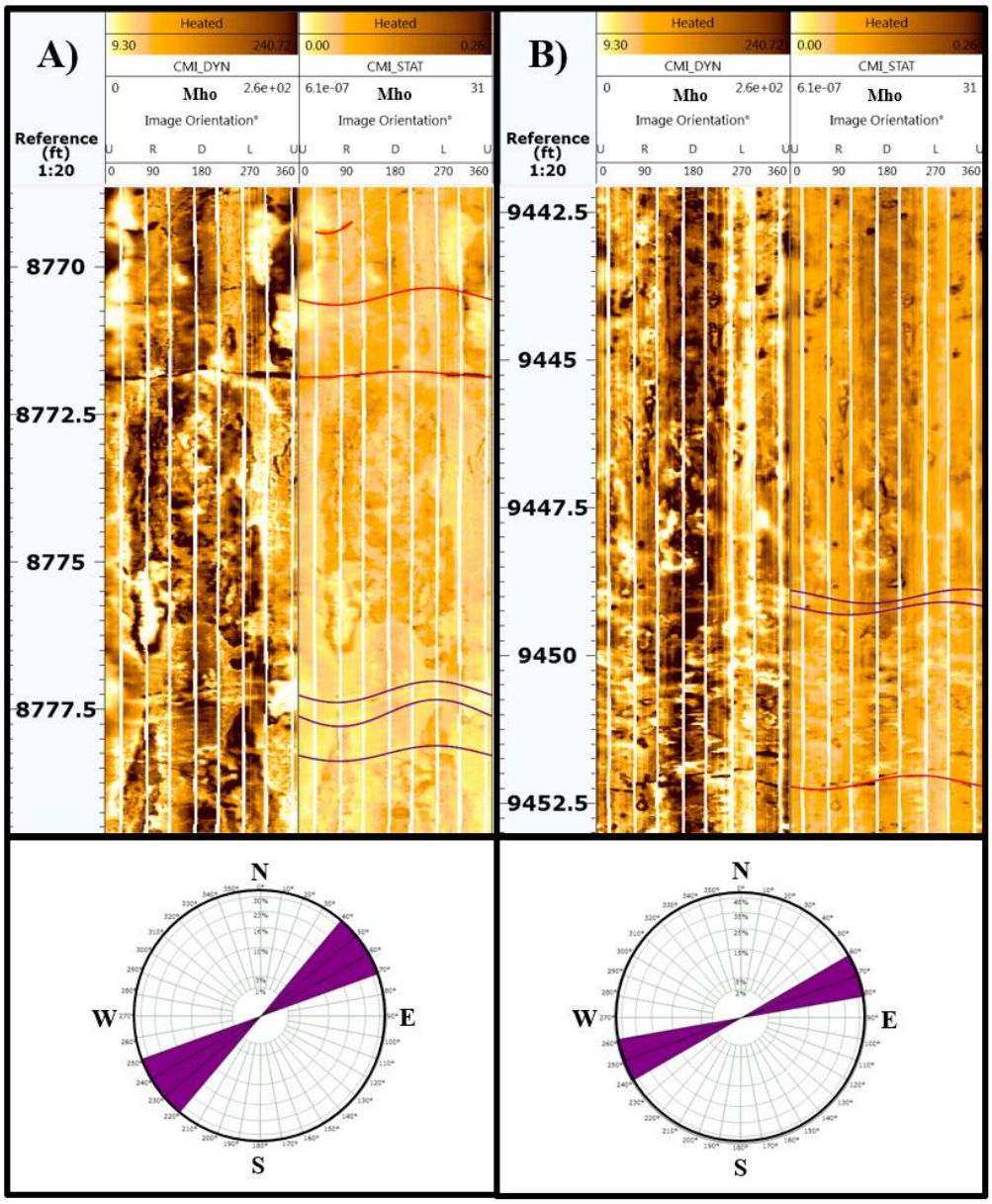

Figure 19. Examples of non-conductive, mineralized fractures in purple where the fracture plane appears as a lighter, white color (lower conductivity) against the darker orange colors of the limestone (higher conductivity). The stereonets below the track show the strike of the non-conductive fractures.

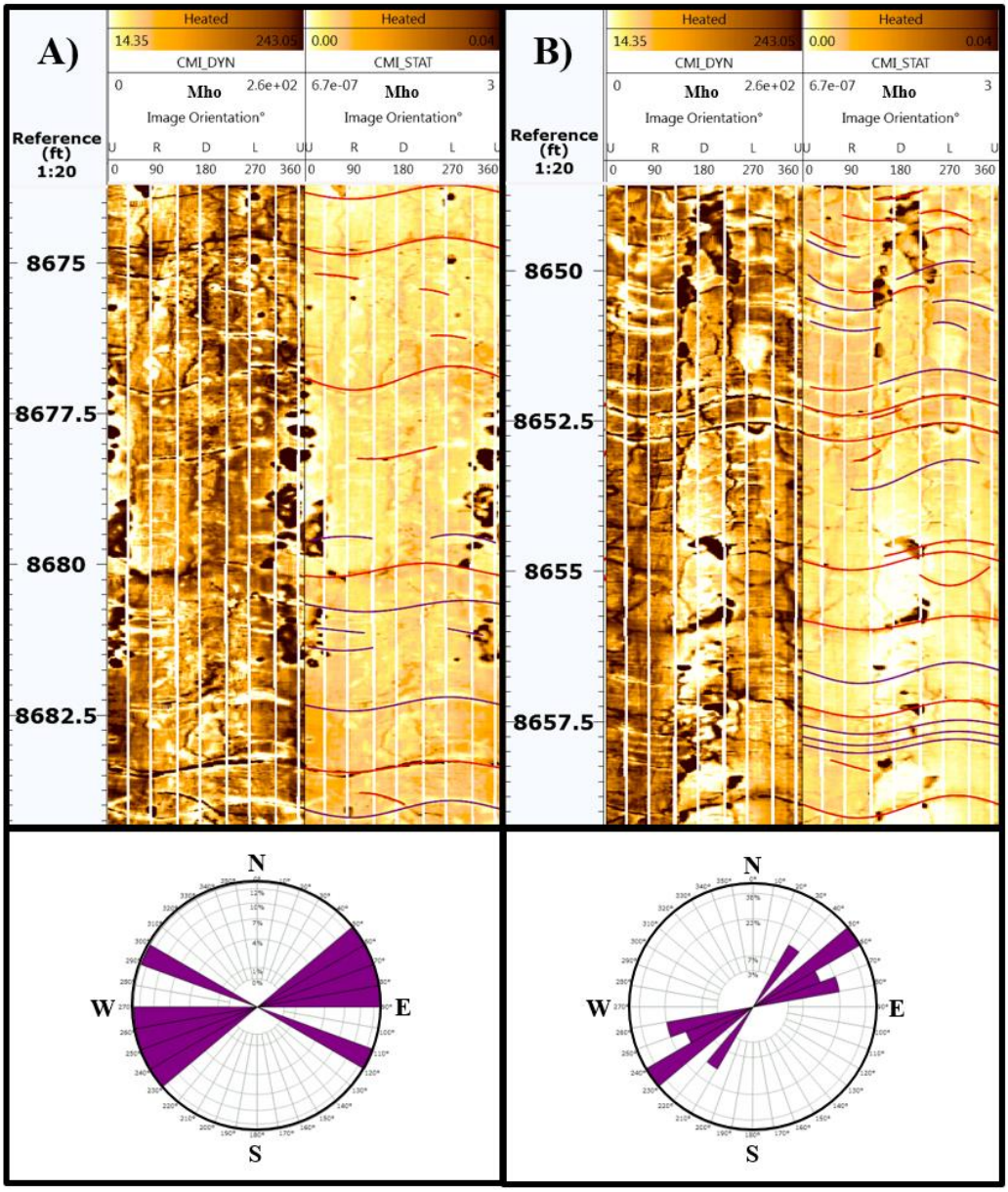

Figure 20. Examples of non-conductive, mineralized fractures in purple where the fracture plane appears as lighter, white colors (lower conductivity) against the darker orange and brown colors (higher conductivity) of the limestone. The stereonets below the track show the strike of the non-conductive fractures.

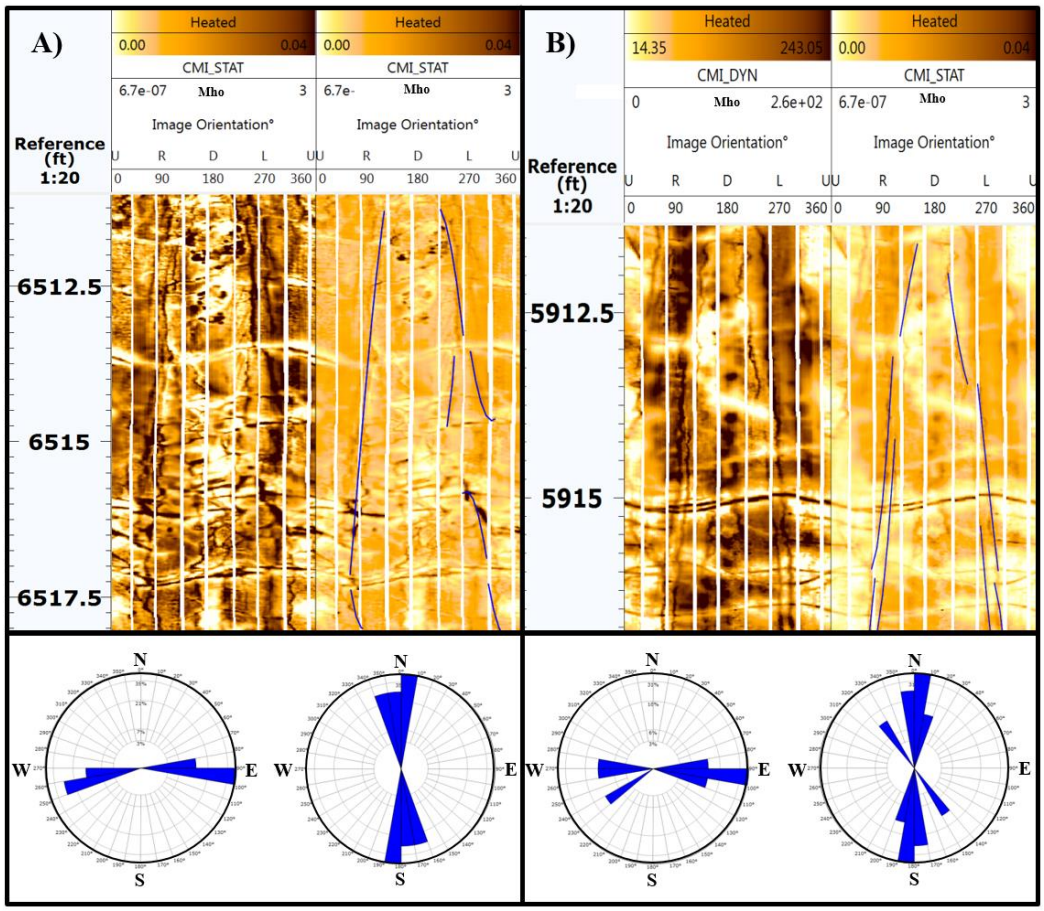

Figure 21. Examples of drilling induced fractures in blue. The stereonets below the track show the azimuth of the induced fractures on the left and the strike of the induced fractures on the right.

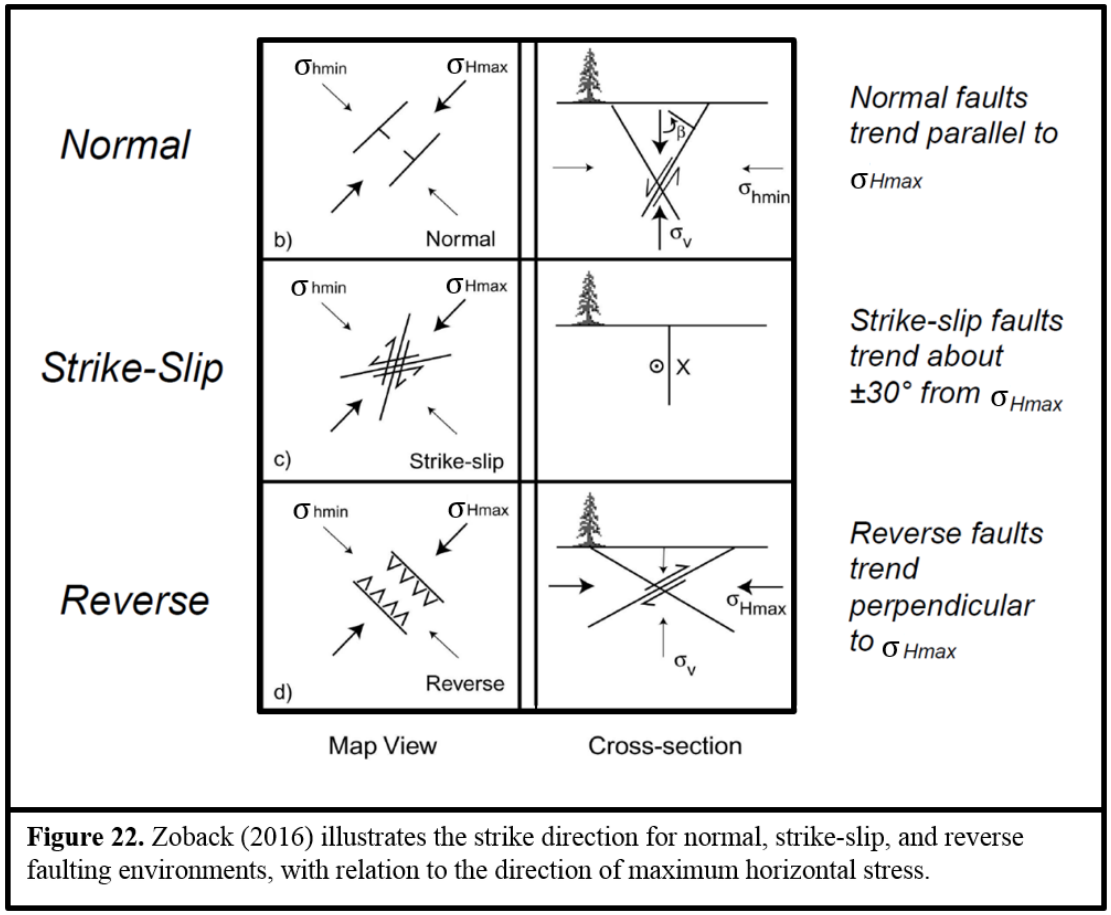

Figure 22. Zoback (2016) illustrates the strike direction for normal, strike-slip, and reverse faulting environments, with relation to the direction of maximum horizontal stress.

ROCK TYPE

The Mississippian Limestone is a very heterogeneous formation and multiple lithologies were present in the borehole image logs. Confirming rock texture seen on image logs with photoelectric index logs, resulted in five rock types. The first rock type was chert, which had photoelectric index readings less than 3.0. Only a small percentage of the wellbores with the borehole image logs contained pure chert. The areas that contained chert were only moderately fractured (Figure 23), with the exception of karsted chert areas. The second rock type was cherty limestone with

photoelectric readings of 3.0 to 4.0. Most areas of the cherty limestone exhibited no fractures, although some limestone was fractured (Figure 24). The third and fourth rock types were limestone and highly fractured limestone. With photoelectric index readings had readings of higher than 4.0. In the borehole image logs, limestone was the most abundant lithology present. There were some stretches of limestone that had little to no fracturing (Figure 25), while other stretches of limestone on the borehole image logs were heavily fractured (Figure 26), suggesting factors other than lithology play a role in fracture genesis. The fifth and last rock type was areas of karsting (Figure 27). Four of the five borehole images had sections of karsting. Karsting occurred in al l three interpreted lithologies: chert, cherty limestone, and limestone. Karsting signature was one of rock rubble within a dark matrix. I initially hypothesized the dark matrix to be either shale from the overlying Cherokee Shale formation, or drilling mud invading void space between the limestone cobbles, potentially being areas of high permeability. The gamma ray logs showed an increase in gamma ray with every karst collapse feature on the borehole image (Figure 28). With the gamma ray response, I interpret the high resistivity matrix as Cherokee Shale.

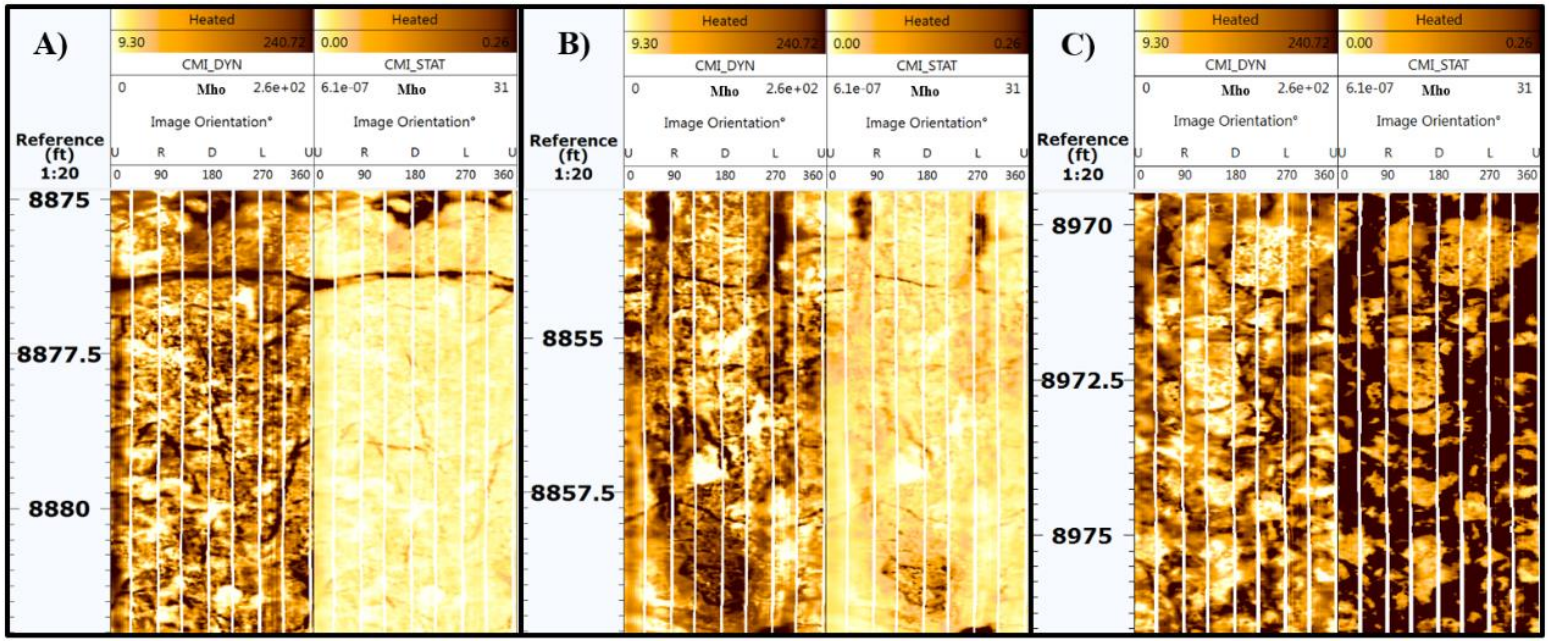

Figure 23. Representative images of fractured chert facies interpreted with assistance from photoelectric index (Pe) logs. Length of each image above is 7.5 ft. Fractured chert represented 4% of the five borehole image logs.

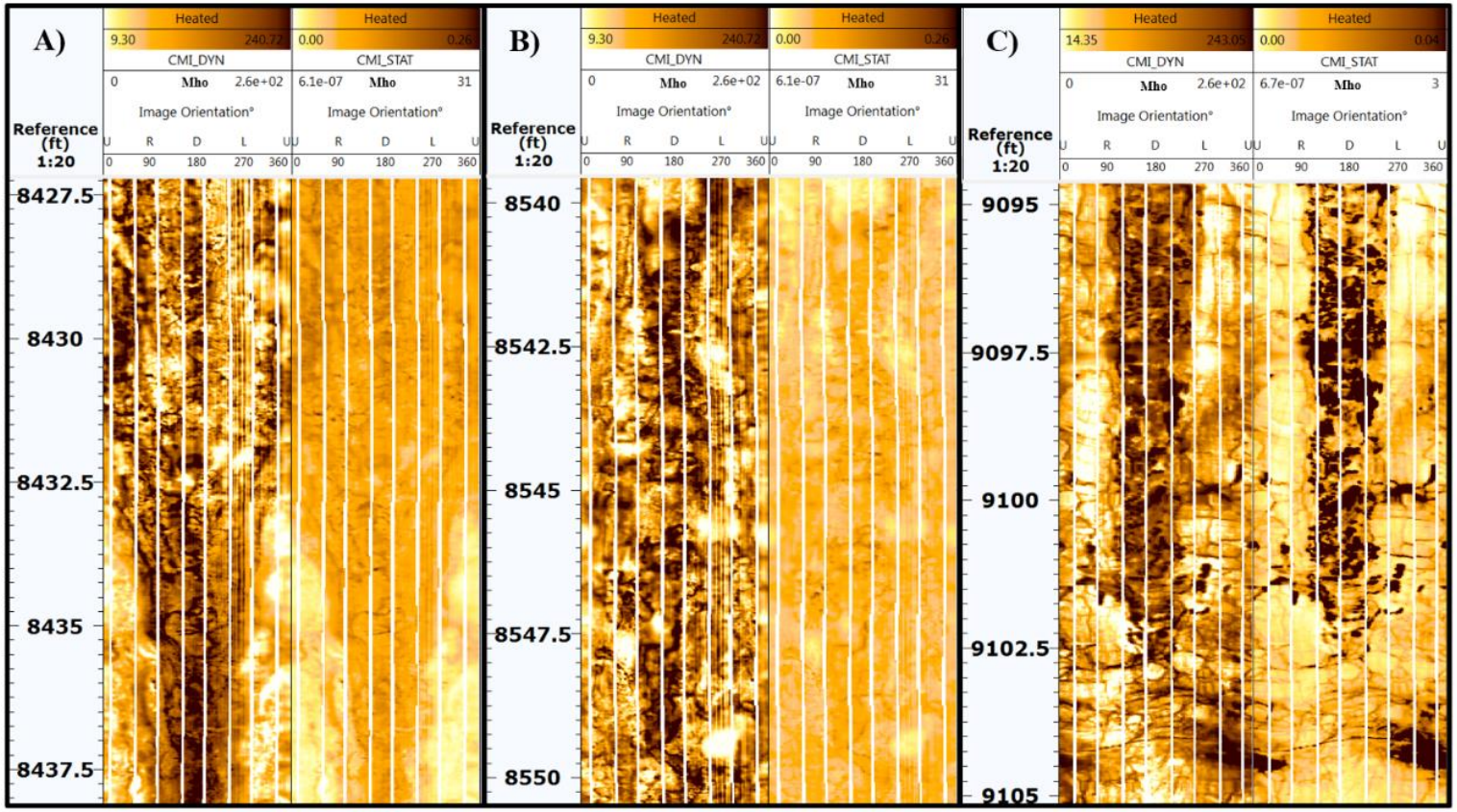

Figure 24. Representative images of cherty limestone interpreted with assistance from photoelectric index (Pe) logs. The cherty limestone is not as intensely fractured as the fractured chert facies. Length of images is 10 ft. Cherty limestone represents 18% of the five borehole image logs.

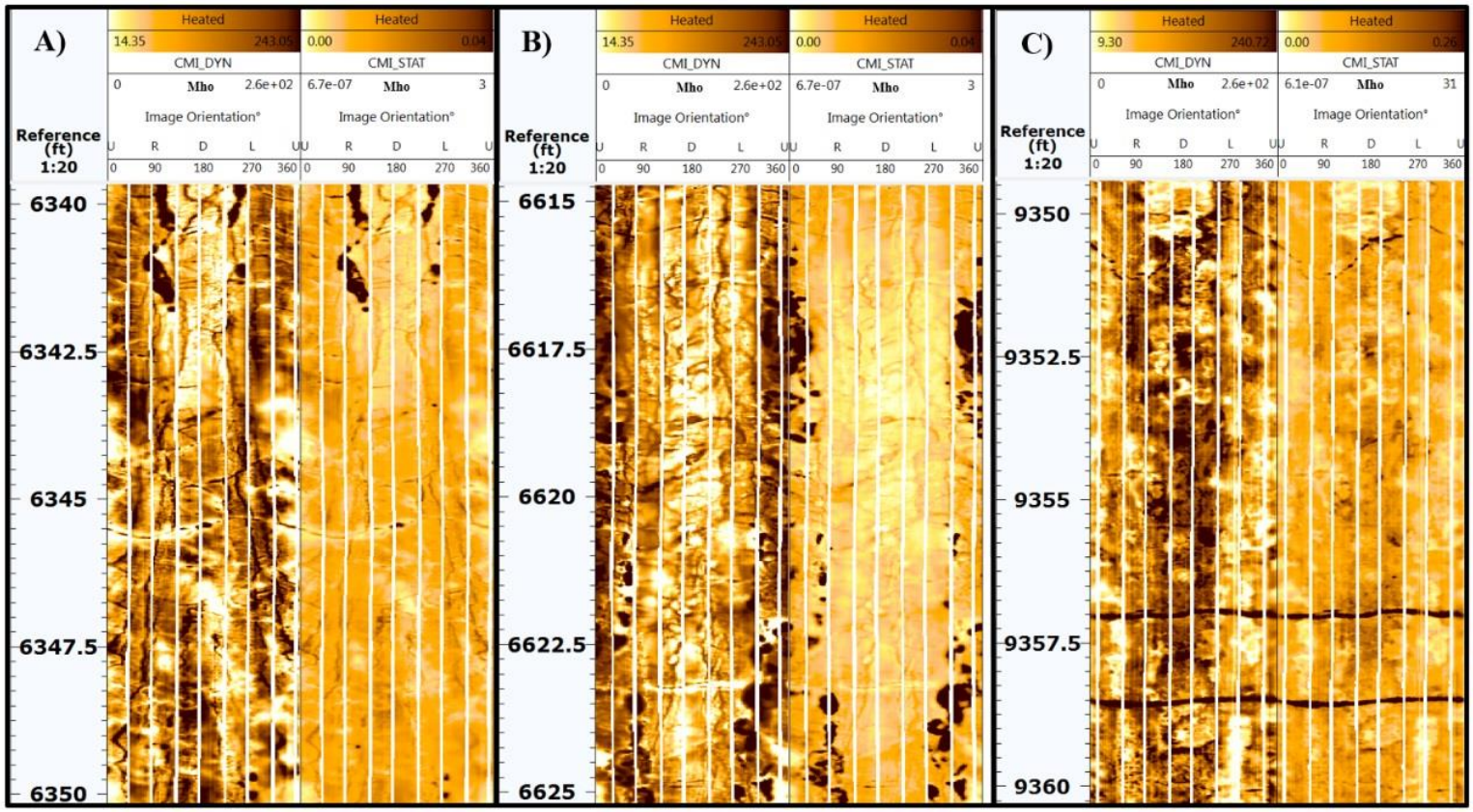

Figure 25. Representative images of limestone, interpreted with assistance from photoelectric index (Pe) logs. Limestone represented 78% of the five borehole image logs. The limestone ranged from areas with minimal fractures, to highly fractured limestone. Highly fractured limestone is highlighted in Figure 22.

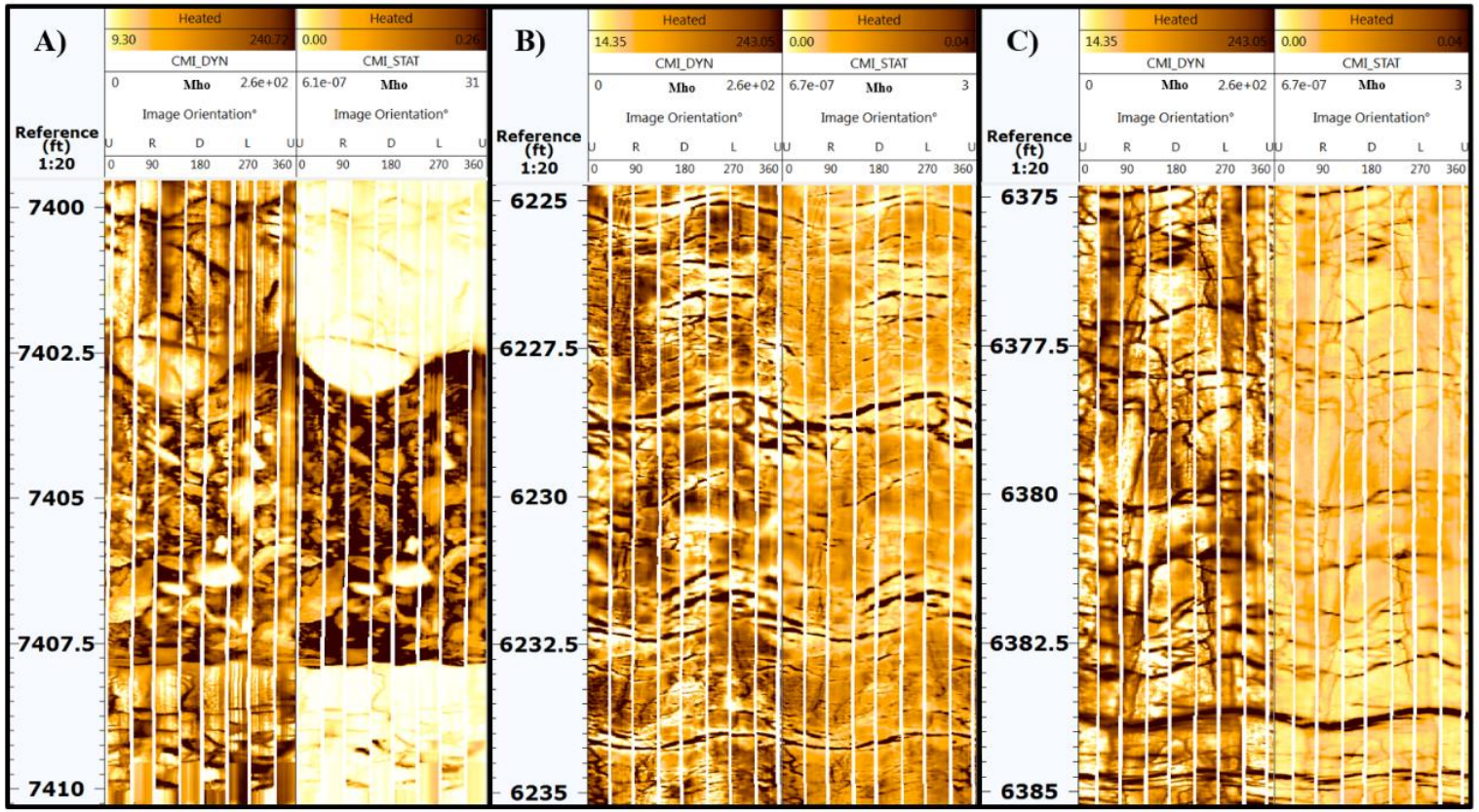

Figure 26. Representative images of limestone, interpreted with assistance from photoelectric index (Pe) logs. Limestone represented 78% of the five borehole image logs. The limestone ranged from areas with minimal fractures, to highly fractured limestone. Minimally fractured limestone is highlighted in Figure 21 and highly fractured limestone is highlighted above.

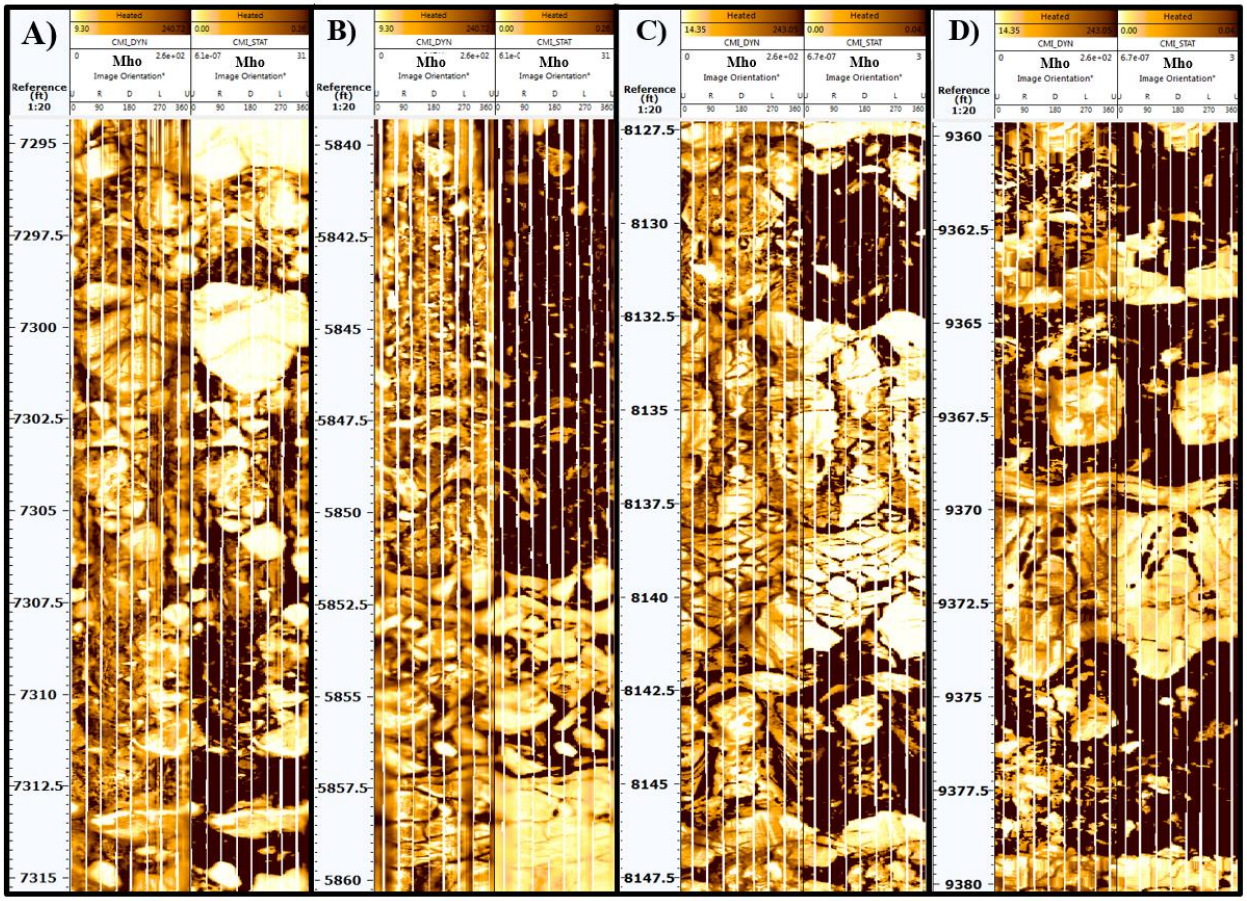

Figure 27. These are 20 foot sections of borehole image logs interpreted as karsted sections of the boreholes. Four of the five boreholes had karsting and karsting occurred throughout all three of the lithologies: chert, cherty limestone, and limestone. The dark resistivity reading in these borehole image logs are interpreted as either shale from the overlying Cherokee shale or drilling mud in-between some of the limestone cobbles, potentially being areas of high permeability.

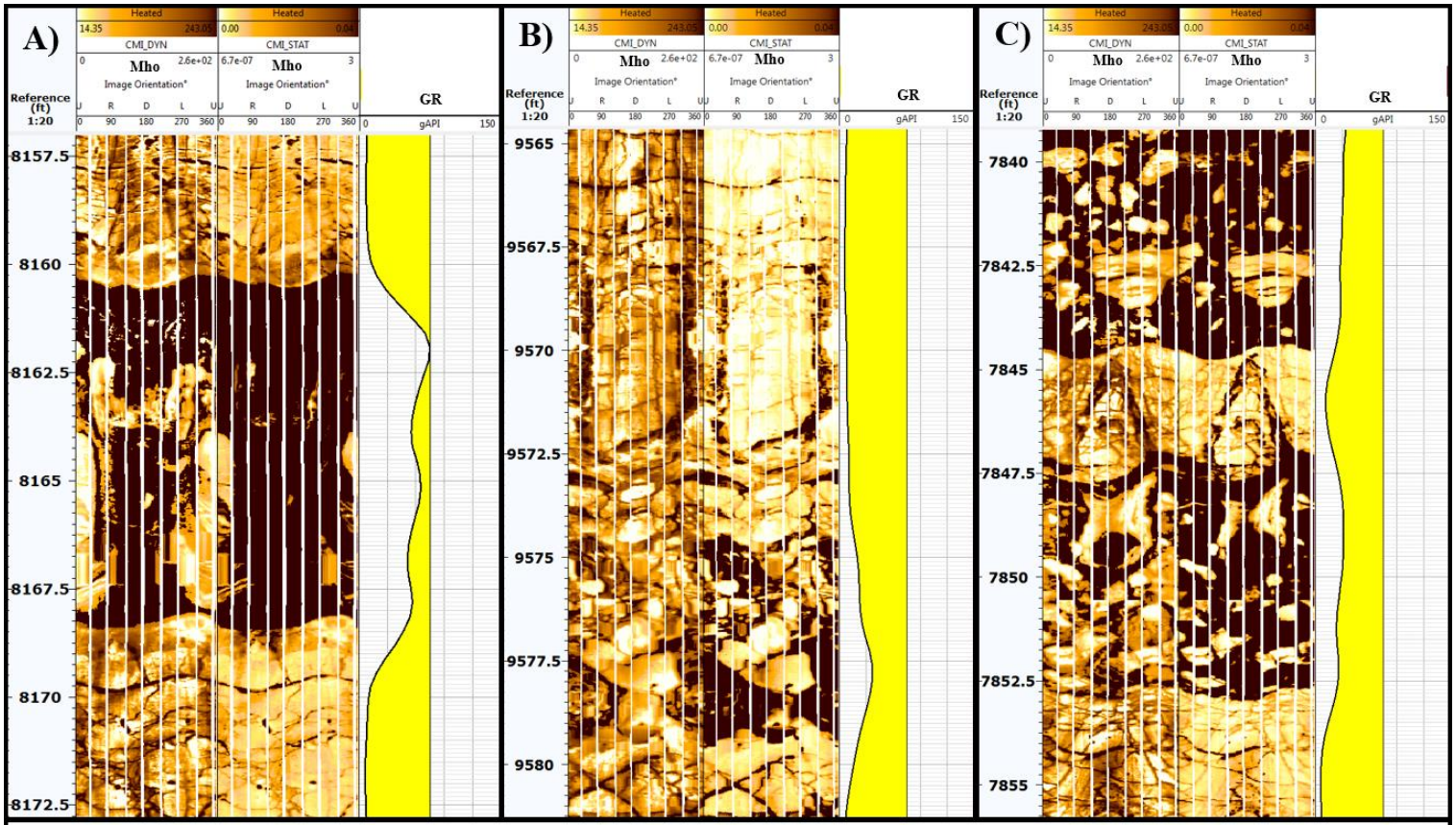

Figure 28. These are 15 foot sections of borehole image logs interpreted as karsted sections of the boreholes. The darker matrix surrounding the limestone cobbles was initially hypothesized as either Cherokee Shale from the overlying formation, or as drilling mud in-between limestone cobbles, potentially being areas of high permeability. Every area of karsting seen on the borehole image was accompanied by an increase in the gamma ray log. With the gamma ray response, the high resistivity readings are interpreted as Cherokee Shale.

IMAGE QUALITY

Borehole image log data quality can suffer in areas, causing limitations on the fracture interpretation. Some of the image logs exhibited streaky and blotchy whitening of the image (Appendix B1), making it difficult to map fractures, and identify rock type from the texture. An interpreter in this case has to look closely for slight resistivity contrasts to pick fractures.

On each of the borehole images interpreted, eight tracks were present. However, many of the images had missing tracks that appeared blank. There were also many areas where the tracks showed little resistivity contrast between the fracture and the matrix (Appendix B2). To address these limitations, one uses the dynamic rather than static image. However, there were a couple of borehole images where resistivity contrast was better viewed on the static image, as opposed to the dynamic image.

Often, there are five to ten ft stretches of "smeared" borehole images, when the electrode pads are moved too quickly along the borehole wall, making fractures difficult to interpret (Appendix B3). Typically at the top or bottom of these "smears" the pads are also misaligned and the interpreter has to select whether to interpret the fracture along the shallower or deeper pads (Appendix B4).

Despite limitations with fracture interpretation on borehole image logs, conductive fractures were interpreted on all five wells with borehole image logs. Once all of the conductive fractures were interpreted, a fracture area log was constructed, in order to model conductive fractures. This fracture area log calculates the area of the fracture surface, divided by the volume of the borehole, along one foot increments (Appendix B5). The fracture area log was used as opposed to a fracture count log, in

order to more accurately account for the appropriate area measurement of full fractures and partial fractures, rather than counting each fracture as “one”.

Chapter 5: Correlating 3D Seismic Data to Borehole Fractures

A number of seismic attributes were computed in order to correlate surface seismic measurements to the fracture intensity and rock type. Geometric attributes such as curvature were computed for both long and short wavelengths, to see if they would correlate to fracture intensity with the hypothesis that short wavelength would better correlate with small scale fracture features. Curvature is the second derivative of the surface, with k_1 highlighting anticlinal features and k_2 highlighting synclinal features (Figure C1). Curvedness, which is the root mean square of most positive and the most-negative curvature, was also computed to see if it would contribute in a non-linear regression correlation to fracture density. Energy ratio similarity is a seismic coherence algorithm computed along reflector dip to compare the waveform but not the amplitude of neighboring traces. In contrast, amplitude curvature compares lateral changes in amplitude for that part of the data having the same waveform. Petrel's Ant Tracking, was used in conjunction with two passes of structure oriented filtering to further sharpen fault images. Shape components of a bowl, valley, saddle, ridge, or dome were also computed to determine if there was a correlation of fractures and rock type to folding and karst collapse.

Envelope and instantaneous frequency were examined for correlation with fracture intensity.

Output volumes from prestack impedance inversions, done by Abdulmohsen Alali, were also examined for correlation to fracture intensity, include P-impedance, S-impedance, Vp/Vs ratio, and density.

I upscaled the one foot resolution interpreted fracture area logs, in order to correlate them to the 110 ft by 110 ft resolution seismic measurements. Specifically, I used a 220 foot sliding window of Backus averaging on the fracture area logs (Figure C2). This Backus averaging creates a fracture intensity log that is on the same resolution as the seismic attributes that are being investigated to calibrate the seismic to fracture intensity. Backus averaging preserves gradational interfaces and achieves rock property curves at seismic scale without creating artificial blocks into the geology.

Having upscaled the well measurements, I used multivariate non-linear regression statistics to calculate which of the attributes could be used to create a fracture intensity volume that would best model the interpreted fracture area logs throughout the seismic volume. Non-linear regression fits the seismic attributes to the fracture intensity to minimize the sum of the squares of the distances of the data points to the curve (Motulsky and Fansnas, 1987). Explicitly, the fracture intensity, $\mathbf{Y_i}$, is related to a vector of predictor variables, or seismic attributes, $\mathbf{x_i}$. This non-linear model has the form:

$$\mathbf{Y_i} = f(\mathbf{x_i}, \boldsymbol{\theta}) + \varepsilon_{i,\ i=1,\ldots n} \quad (1)$$

Where $\mathbf{Y_i}$ are resonses, f is the known function of the covariate vector of predictor variables, $\mathbf{x_i} = (x_{i1}, \ldots, x_{ik})^T$ and the parameter vector $\boldsymbol{\theta} = (\theta_1, \ldots, \theta_p)^T$, and ε_i are random errors (Smyth, 2002).

With multivariate non-linear regression, more than one step is taken to come to the best solution, where the best fit to the data requiring a reiterative process. First, one computes an initial estimate of the correlation for each attribute. Then, in the nonlinear regression process, different attributes are combined to improve the fit of the curve to

the data. These iterations continue until the process converges. The resulting attribute correlations must also be examined to be geologically sound. For example, higher fracture intensity may be expected to be seen with larger values of curvature; as seen in fracture and curvature studies that found higher fracture intensity on the hinge zone of a fold (Yenugu and Marfurt, 2011; White, 2013). If a candidate attribute shows a correlation counter to findings in previous studies and geologic knowledge, then that attribute should be taken out of the multivariate nonlinear regression and replaced with another attribute that illustrates an acceptable correlation. When doing the multivariate non-linear regression statistics, it is also beneficial to not over train the model by incorporating too many seismic attributes. Of the 20 seismic attributes examined, only six were retained in the final model.

The resulting fracture model had a correlation coefficient of 0.744 and an R-Squared value of 0.553 (Figure 29). The blind well with interpreted fractures, which was not implemented in the computing of the model, was predicted with similar fracture intensity trends (Figure 30). Figure 30 shows the increase of fracture intensity predicted along the lateral well, in particular the area of high fracture intensity at a measured depth of 7,700 ft. There is an area of discrepancy, where the bracketed section shows some increases in fracture intensity with the model, which was not seen on the borehole image log. Figure 31 shows the four other fracture area logs that were implemented in the generation of the fracture model compared to the resulting modeled fractured intensity above them. The model was able to predict much of the same fracture intensity trends along these laterals, as seen with the arrows. However, there are some

areas along these laterals that also have some discrepancies from the original interpretation of fracture area along these boreholes, highlighted with brackets.

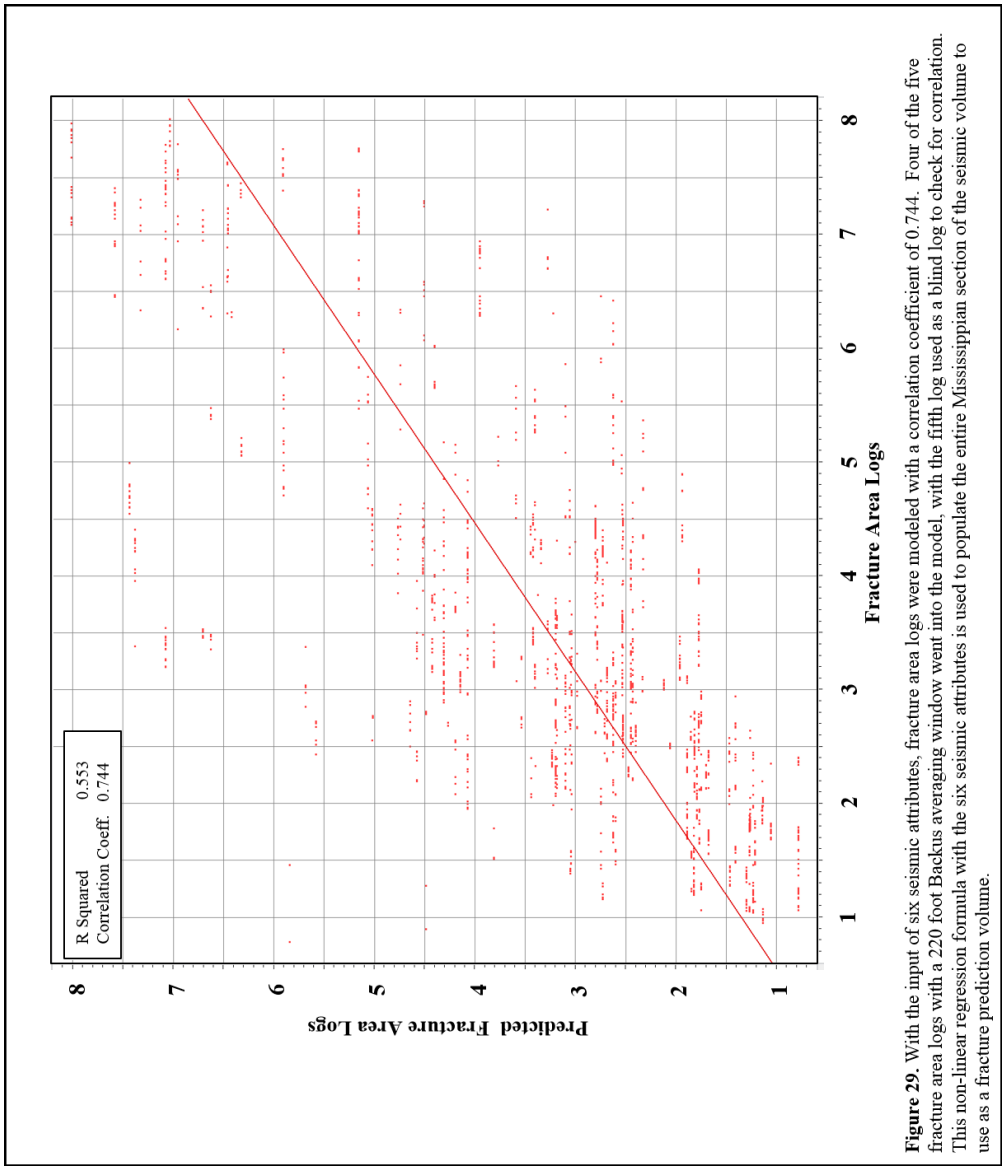

Figure 29. With the input of six seismic attributes, fracture area logs were modeled with a correlation coefficient of 0.744. Four of the five fracture area logs with a 220 foot Backus averaging window went into the model, with the fifth log used as a blind log to check for correlation. This non-linear regression formula with the six seismic attributes is used to populate the entire Mississippian section of the seismic volume to use as a fracture prediction volume.

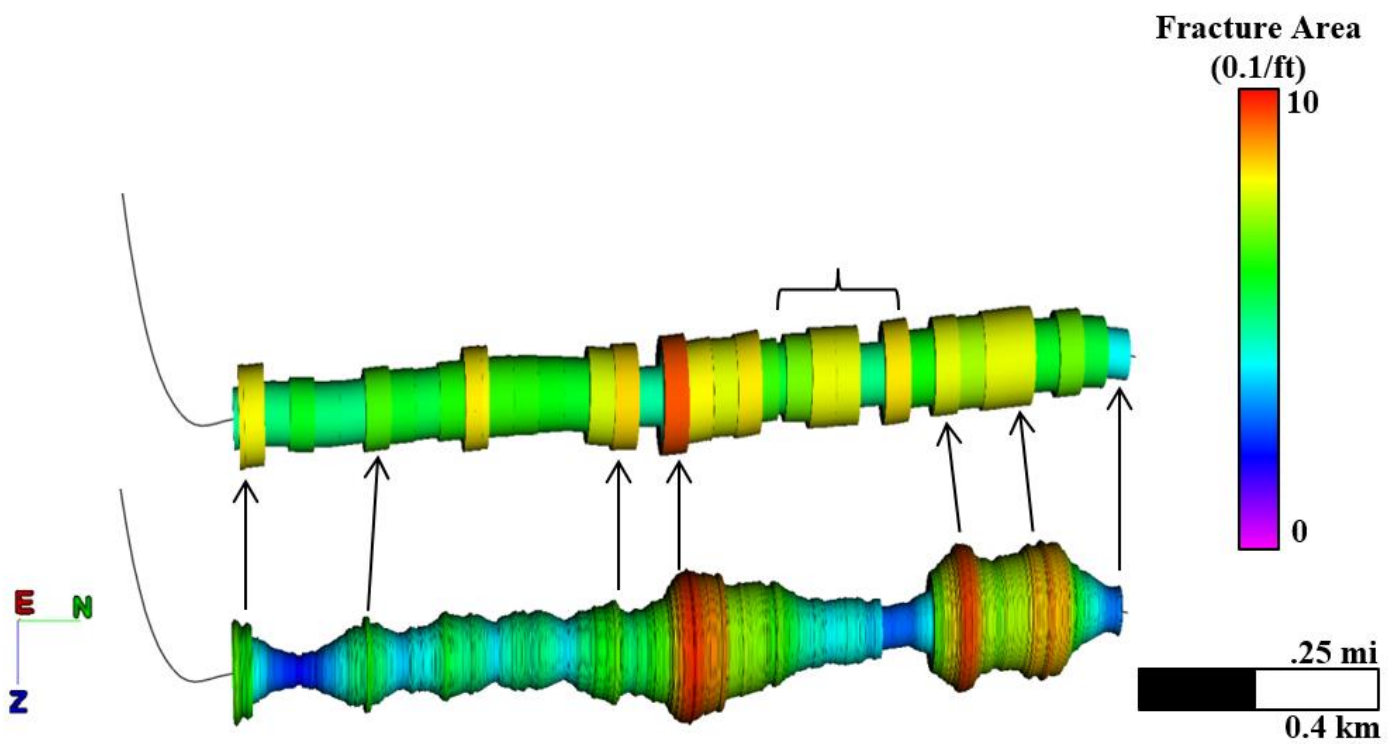

Figure 30. This is the blind well that did not go into the generation of the fracture intensity model. Many of the increases and decreases in fracture intensity line up between the model, above, and the fracture area log, below. Arrows show features that align and the bracketed area shows an area where the model increases fracture intensity, when in fact fractures decrease in intensity.

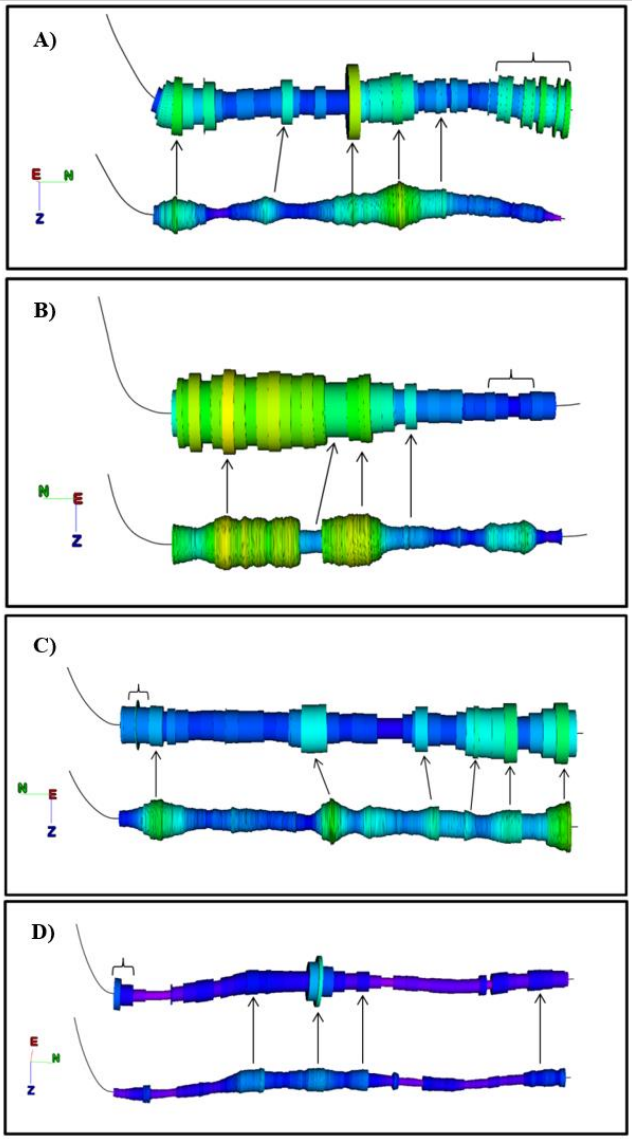

Figure 31. Above are the four wells that went into the fracture intensity model. The bottom logs are the interpreted Fracture Area logs with a 220 foot Backus average and the top logs show what was modeled using the six seismic attributes. Arrows indicate fracture intensity increases and decreases where the model and original logs align and brackets show features that were modeled, but were not in the original logs.

The six seismic attributes implemented in the fracture intensity model, and their correlation, can be seen in Figure 32. These attributes are displayed in order of their significance to the model. Two of the attributes used in the model were complex trace attributes, instantaneous frequency and amplitude.

Envelope is defined by the equation:

$$A(t) = [f^2(t) + f^{*2}(t)]^{\frac{1}{2}}, \quad (2)$$

where $f(t)$ is the real seismic trace and $f^*(t)$ is the quadrature, or conjugate trace (Taner et al, 1979). High reflection strength can be an indicator of drastic changes of lithology, such as the drastic change across the Mississippian Limestone unconformity, from the overlying Cherokee Shale to the abrupt change to the limestone. Envelope represents the acoustic impedance contrast. With increased fracturing, density and p-impedance decrease. P-impedance was also examined and a decrease in p-impedance correlated with an increase in fractures. However, envelope had a larger contribution to predicting fractures due to the fact that envelope is a representation of p-impedance and density. Also, the wells examined lie close to the unconformity, where highly fractured collapse features contain Cherokee Shale and the envelope between the overlying Cherokee Shale and the Mississippian Limestone is diminished in the areas of shale and limestone rubble.

Instantaneous frequency is defined by the equation:

$$\frac{d\theta(t)}{dt} = \omega(t), \tag{3}$$

which is the rate of change of the time-dependent instantaneous phase, gives the time-dependent frequency. The change of instantaneous frequency typically changes gradually with thinning beds or a gradual change in the lithology. A drastic change in the instantaneous frequency can be an indicator of a more drastic change in lithology, or an oil water contact (Taner et al, 1979).

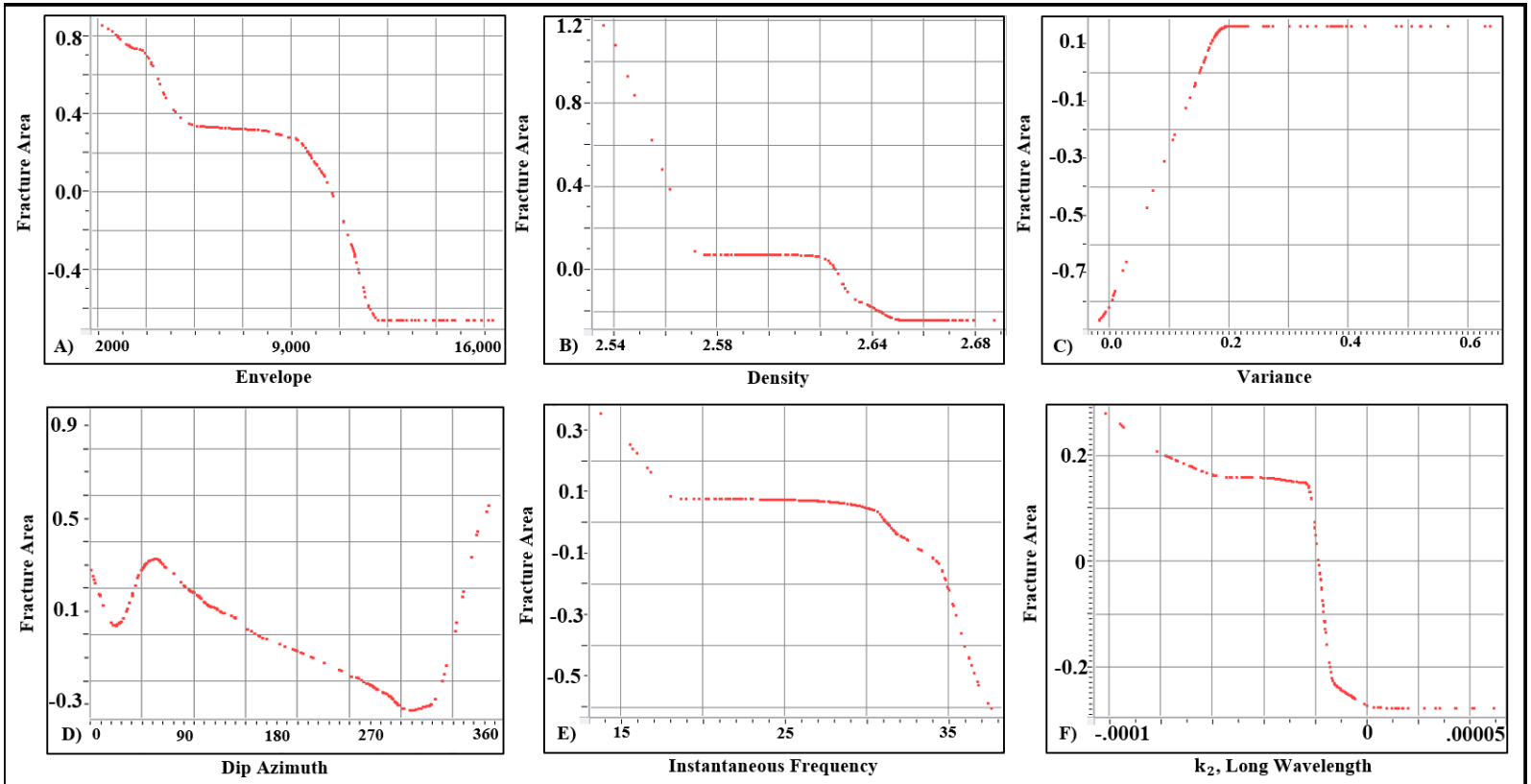

Figure 32. Seismic attribute inputs into the non-linear regression model predicting fractures. The attributes are in order of their significance to the model. These seismic attributes include physical, geometric, and acoustic impedance output attributes. The x-axis in the correlation plots show input values for each attribute, and the y-axis illustrates normalized values.

The model shows a correlation of an increase in fractures with a decrease in frequency. This correlation is likely a result of higher frequencies being scattered due to attenuation in fractured areas (Taner, 2001). (Figure C3) The average attenuation of the first 50 ft of the Mississippian Limestone illustrates a correlation of areas with high attenuation and areas of tectonic deformation and tripolitic chert. (Figure C4) Frequency of the survey illustrates lower frequencies in areas of higher dip magnitude. Similarly, increased fracture intensity correlates with lower reflectivity strength. Areas with increased fracturing were seen in areas of small collapse features. With less contrast between the top of the Mississippian and the overlying Cherokee Shale, the acoustic impedance contrast will weaken in these rubble areas. (Figure 33) Envelope illustrates areas along the five interpreted borehole images where a decrease in reflection strength correlates to an increase in fracture intensity. Envelope represents the acoustic impedance contrast; density and Zp decrease with an increase in fracturing.

The prestack inversion volume which best correlated with fracture intensity was the density volume. Fracture intensity was much higher with a decrease in density. In fact, when looking at the correlation of all of the inversion volumes, all of the outputs had a correlation of higher fracture intensity with lower impedance values. The lower impedance and lower density correlation could highlight some highly fractured, less dense, tripolitic chert in other portions of the seismic survey. Fracture intensity is plotted against density in the vertical section (Figure 34). A look at the wells with higher fracture intensity can be seen up against the dark blues, or higher density. However, Well E and the second half of the lateral of Well B have a low amount of fractures, and are seen to be drilling through rock of higher density.

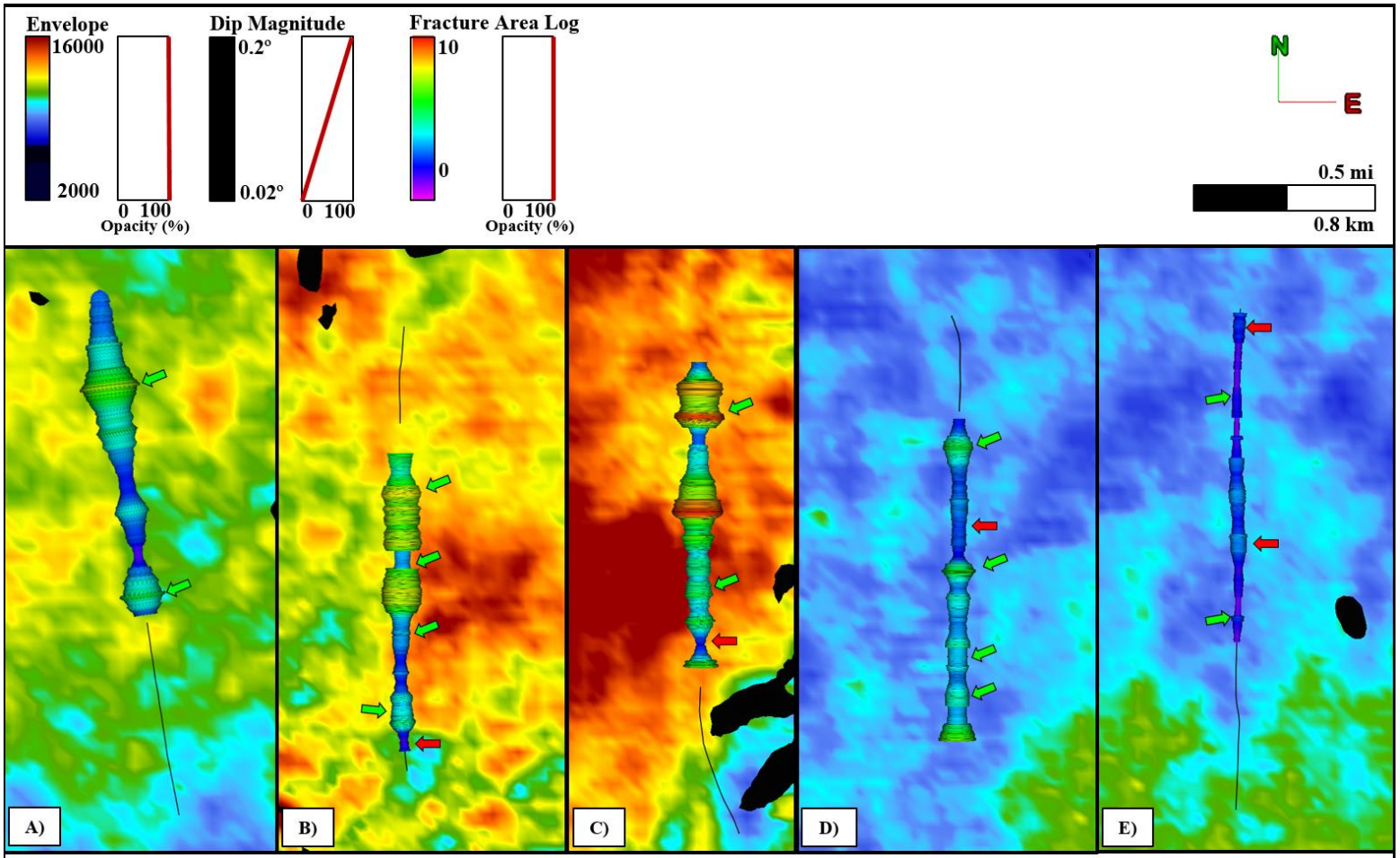

Figure 33. Envelope had the largest correlation to fracture intensity. Interpreted fracture area logs have been plotted on envelope, co-rendered with dip magnitude. Not every decrease in envelope coincides with an increase in fractures. Green arrows indicate trends where a decrease in envelope aligns with an increase in fractures, or when a decrease in fractures aligns with an increase of envelope. Red arrows indicate areas that go against the correlation of decreasing envelope with an increase in fracture intensity.

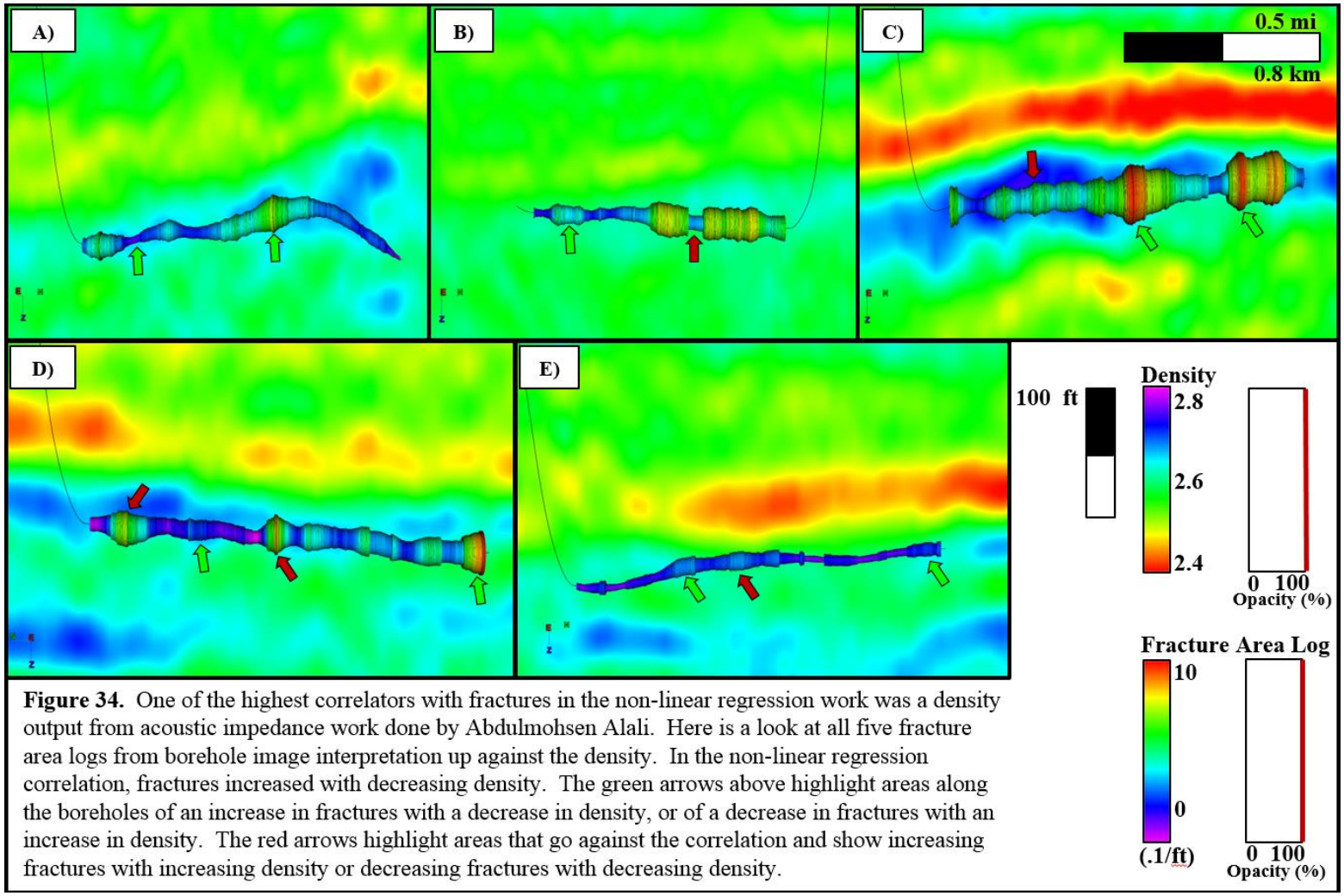

Figure 34. One of the highest correlators with fractures in the non-linear regression work was a density output from acoustic impedance work done by Abdulmohsen Alali. Here is a look at all five fracture area logs from borehole image interpretation up against the density. In the non-linear regression correlation, fractures increased with decreasing density. The green arrows above highlight areas along the boreholes of an increase in fractures with a decrease in density, or of a decrease in fractures with an increase in density. The red arrows highlight areas that go against the correlation and show increasing fractures with increasing density or decreasing fractures with decreasing density.

Three geometric attributes were also used in modeling fracture intensity. The most significant geometric attribute in modeling fracture interpretation was variance, which is a coherence algorithm. Coherence compares the waveforms of neighboring traces, and is computed along reflector dip. Variance is commonly used as an edge detector attribute. Variance is co-rendered in Figure 10 along with the depth structure of the top of the Mississippian Limestone. It is shown that variance aids in highlighting faults throughout the survey.

The next geometric attribute which contributed to fracture prediction was dip azimuth. Dip azimuth is measured in the direction of maximum downward dip, and is measured perpendicular to the geologic strike (Marfurt, 2007). In Figure cross plots of all the correlative attributes (Figure 32), it is evident that fracture intensity increases the most when dip azimuth is 360º, or due north. The dip of the Mississippian Limestone is to the south; therefore dip to the north indicates areas of deformation, resulting in increased fracturing. There is a secondary increase in fracture intensity when the dip azimuth is 60º, or northeast, which is the same direction as faulting and fracturing in the study area. Dip azimuth in the Mississippian (Figure 35) highlights this correlation with yellow arrows illustrating an increase in fracture intensity along dip azimuth of 360º. Red arrows highlight an increase in fracture intensity along a dip azimuth of 60º. A majority of increase with fracture intensity aligns with dip in these two directions, but the pick arrows highlight areas of fracture increases along other dip directions.

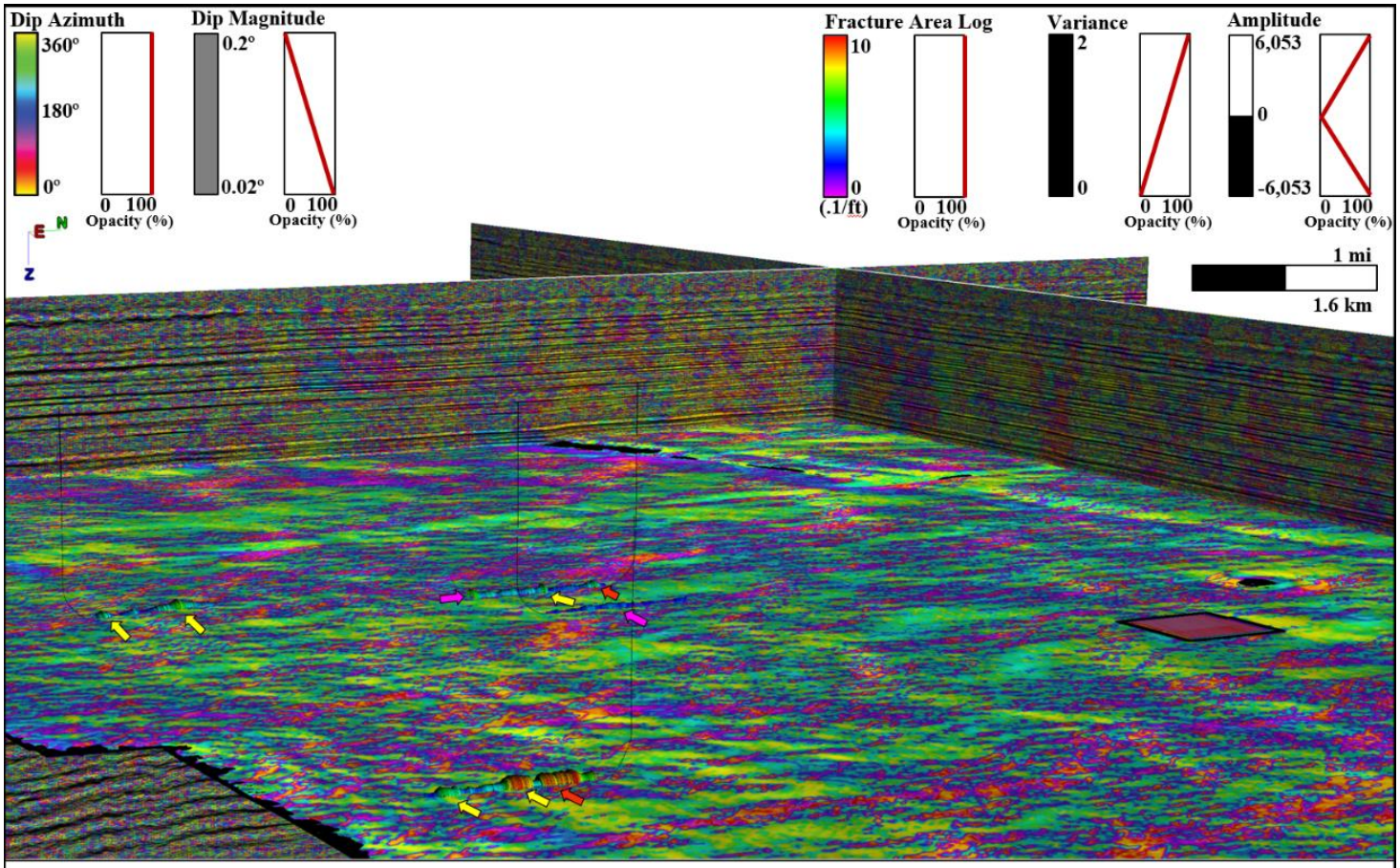

Figure 35. One of the inputs into the fracture intensity model was dip azimuth. Here dip azimuth, dip magnitude and variance have been extracted onto the Mississippian Limestone and the fracture intensity logs have been plotted along four of the five laterals that had fracture interpretation. The non-linear regression showed fractures intensify at a dip azimuth of 360° and 60°. 360° is represented in yellow and 60° is represented in a dark orange color. Yellow and dark orange arrows point out areas of high fracture intensity along the laterals that match up with these two dip azimuth directions. Pink arrows on the map point out areas that don't align with the statistics. Well E has a large swath of it's lateral in a dip azimuth of 360°, but had less fractures than all the other wells. There is also a pink arrow at the end of well D where an area of high fracture intensity does not align with a dip azimuth of 360° or 60°

The last geometric attribute which contributed to fracture intensity was k_2, long wavelength most negative curvature. This aligns with the highly fractured collapse features seen in the borehole image logs. Most negative curvature highlights synclinal features, which would be present in karst collapse features. Most negative curvature (Figure 36) shows how faults are highlighted with most positive and most negative curvature. However, much of the increases in fracture intensity along interpreted borehole images are in areas of k_2, with the exception of one area of increased fracture intensity in Well A, which has a drastic increase of fractures in an area of k_1.

Azimuthal intensity was computed from k_2 most negative curvature and from k_2 strike from azimuths -90º, -60º, -30º, 0º, 30º, and 60º. Azimuthal intensity was extracted onto a surface 35 feet into the Mississippian Limestone (Figure 37). Azimuthal intensity at -60º correlated best with interpreted fractures with a correlation coefficient of 0.450. Azimuthal intensity at -60º had a 0.150 correlation coefficient with water production and a 0.09 correlation coefficient with oil production.

The shape index seismic attribute did not contribute to an increase in fracture intensity overall in the multivariate nonlinear regression modeling. However, shape index did an excellent job at highlighting the collapse features seen in the borehole images with a visual correlation (Figure 38). There were eleven collapse features interpreted in the five borehole image logs. Of those, nine of them are highlighted with the bowl value found in the shape index attribute.

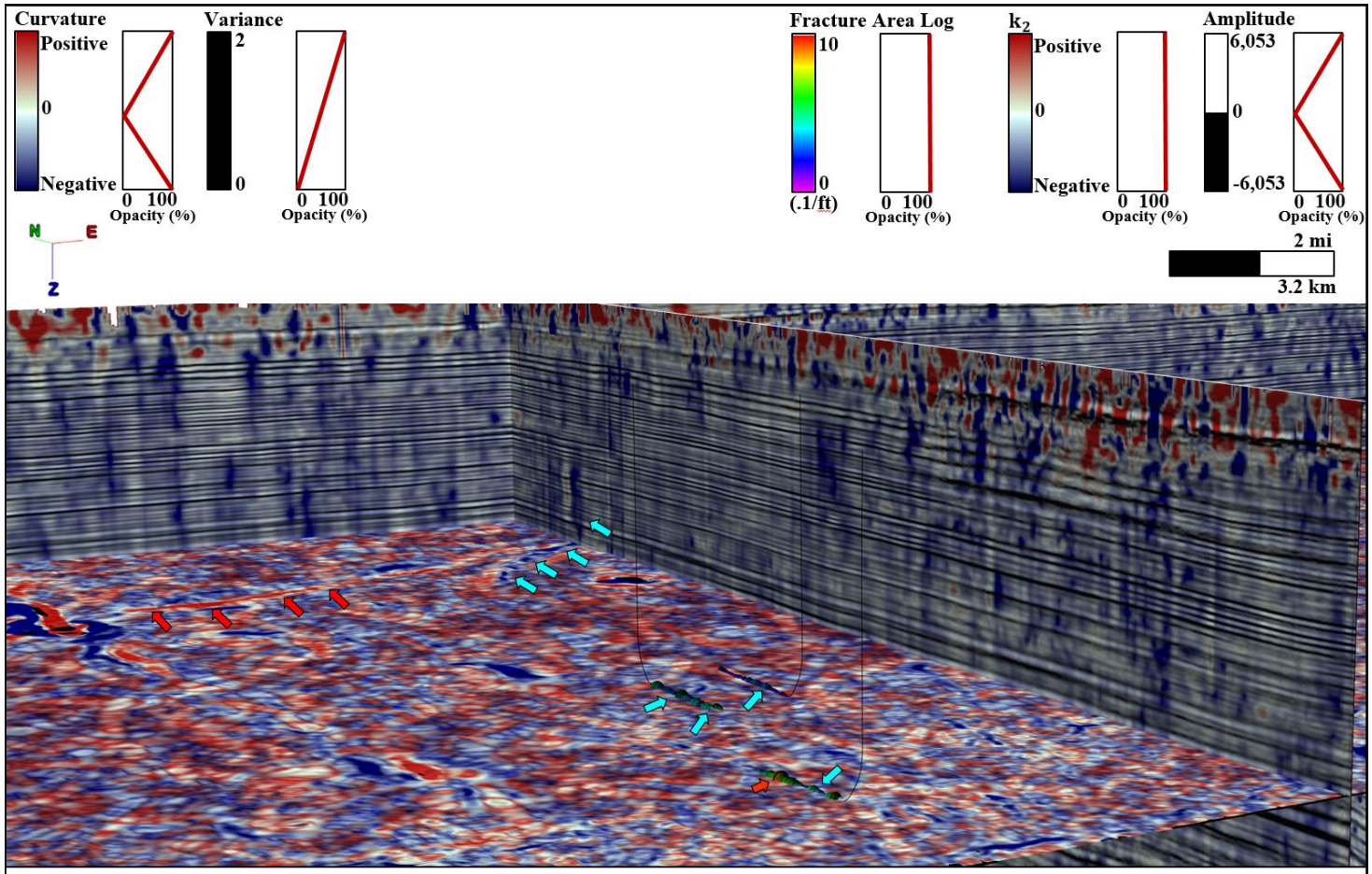

Figure 36. One of the inputs into the fracture intensity model k_2, longwave most negative curvature. Here most positive and most negative curvature are co-rendered along the Mississippian Limestone. Amplitude and k_2, most negative curvature, are co-rendered along the vertical seismic displays. The fracture intensity along the wellbore has areas of negative curvature that align with high fracture intensity, noted in cyan arrows. There are also areas of high fracture intensity that align with most positive curvature as well, noted with a red arrow. Most positive and most negative curvature really highlight large scale faults in the study area.

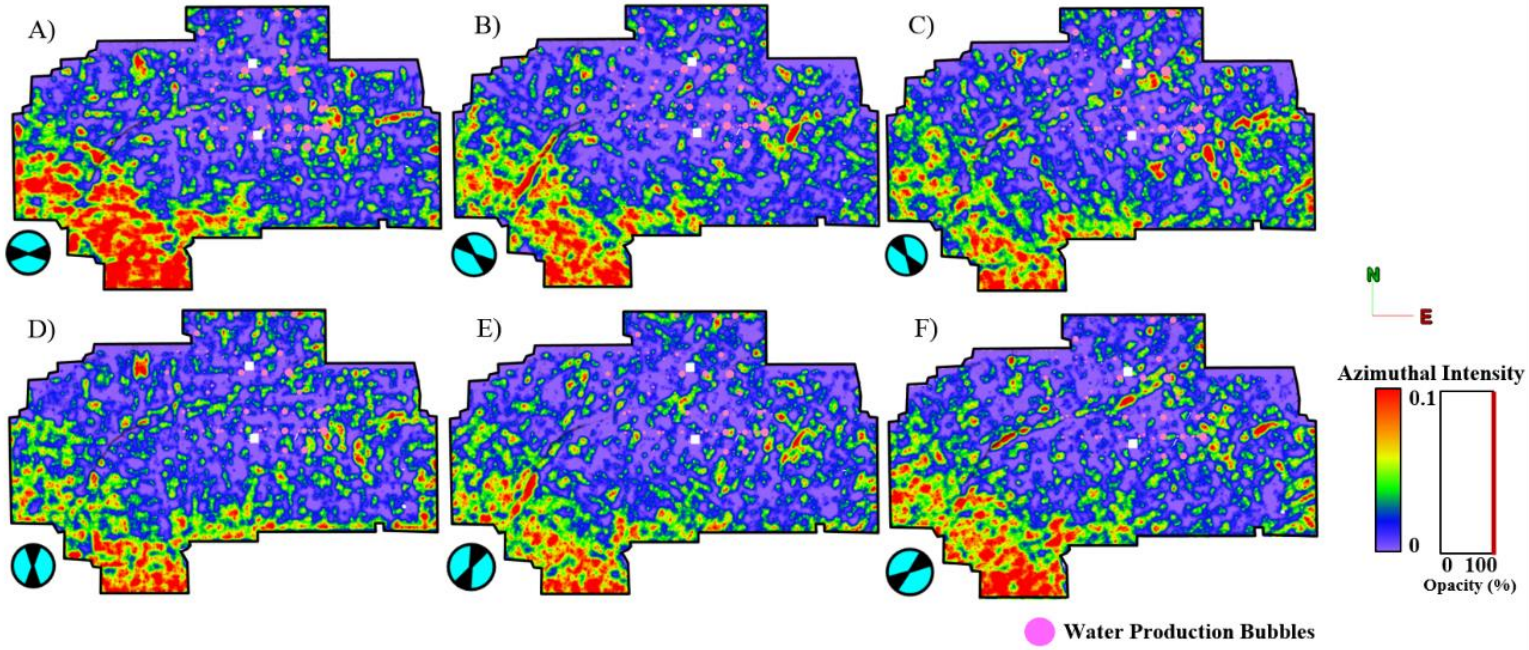

Figure 37. Azimuthal intensity was computed from k_2 most negative curvature and from k_2 strike from azimuths (A) -90°, (B) -60°, (C) -30°, (D) 0°, (E) 30°, and (F) 60°. Azimuthal intensity was extracted onto a surface 35 feet into the Mississippian Limestone. (B) -60° correlated best with interpreted fractures with a correlation coefficient of 0.450. (B) -60° had a 0.150 correlation coefficient with water production and a 0.09 correlation coefficient with oil production.

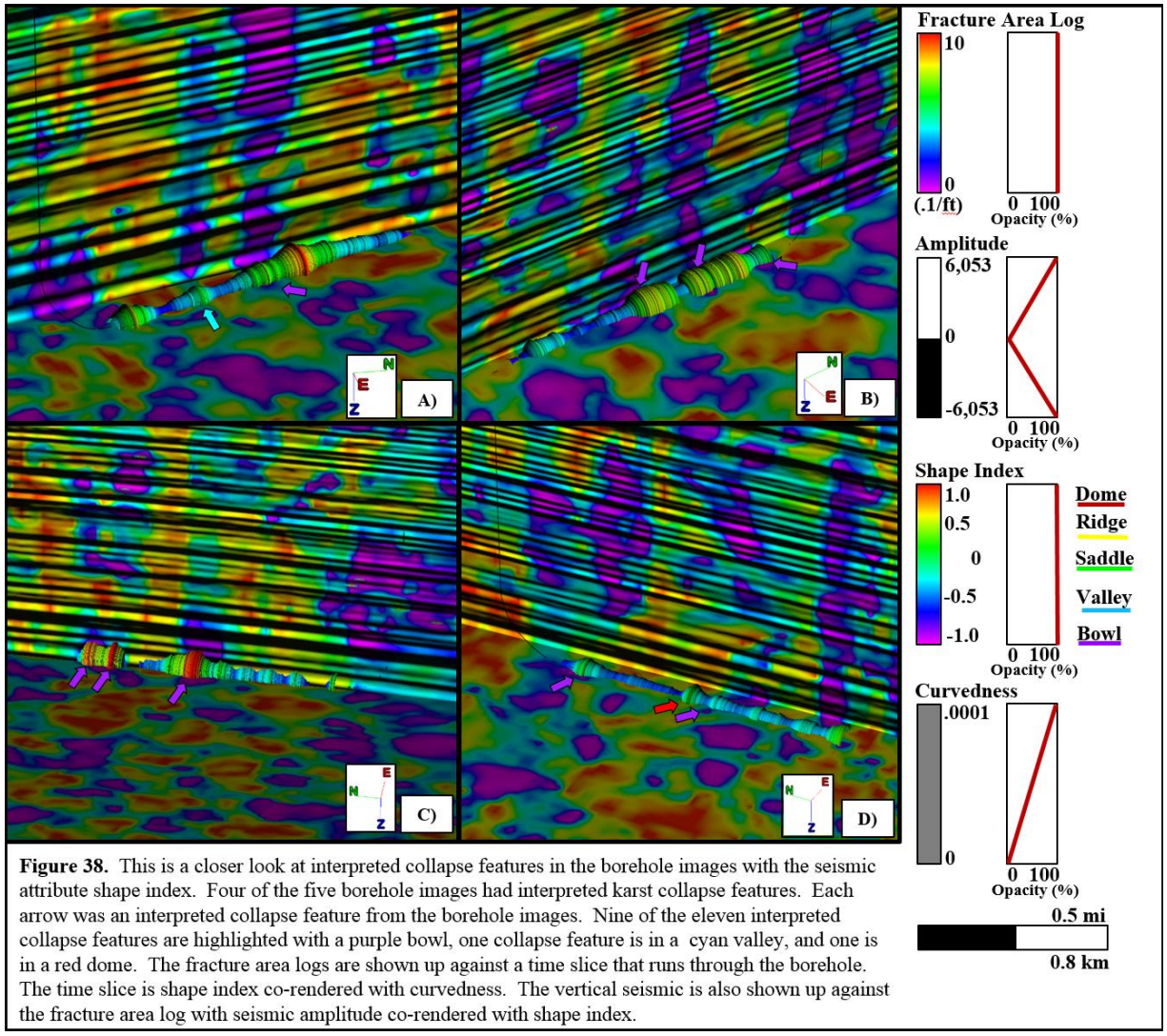

Figure 38. This is a closer look at interpreted collapse features in the borehole images with the seismic attribute shape index. Four of the five borehole images had interpreted karst collapse features. Each arrow was an interpreted collapse feature from the borehole images. Nine of the eleven interpreted collapse features are highlighted with a purple bowl, one collapse feature is in a cyan valley, and one is in a red dome. The fracture area logs are shown up against a time slice that runs through the borehole. The time slice is shape index co-rendered with curvedness. The vertical seismic is also shown up against the fracture area log with seismic amplitude co-rendered with shape index.

These six attributes were used to generate a fracture intensity model throughout the entire seismic volume. Observing the fracture intensity model (Figure 39), there is an increase in fracture intensity along known mapped faults in the survey, which are mapped on Figure A3. There is also an area of increased fracturing in areas that contain a higher probability of tripolitic chert (Lindzey, 2015). There are areas of anomalous high fracture intensity along the perimeter of the seismic survey, which is assumed to be edge effect. Lastly, there is a strong correlation of modeled fractures in the model with a known area of heavy karsting in the southeastern part of the survey.

When looking at the vertical slices through the fracture intensity model (Figure 40), red arrows highlight mapped faults. There is high fracture intensity along many of these know faults. However, the bands of high fracture intensity swaths run more laterally than vertically through the section, which is expected considering amplitude and density were the most significant seismic attributes contributing to fracturing. This could be a result of fracturing being controlled by lithology changes throughout this heterogeneous formation and enhanced with structural deformation highlighted by coherence and curvature.

The resulting fracture model was then utilized, along with two prestack impedance attributes, Lambda Rho and Mu Rho, to highlight the relationship between shear and compressional strength with fracture intensity. Lambda Rho and Mu Rho were extracted from a surface 35 feet into the Mississippian Limestone, cross plotted against each other, and colored by fracture intensity (Figure 41). Fracture intensity is high with low shear strength and high compressional strength (Alzate, 2012). The highly fracture areas can take more strain without further breaking.

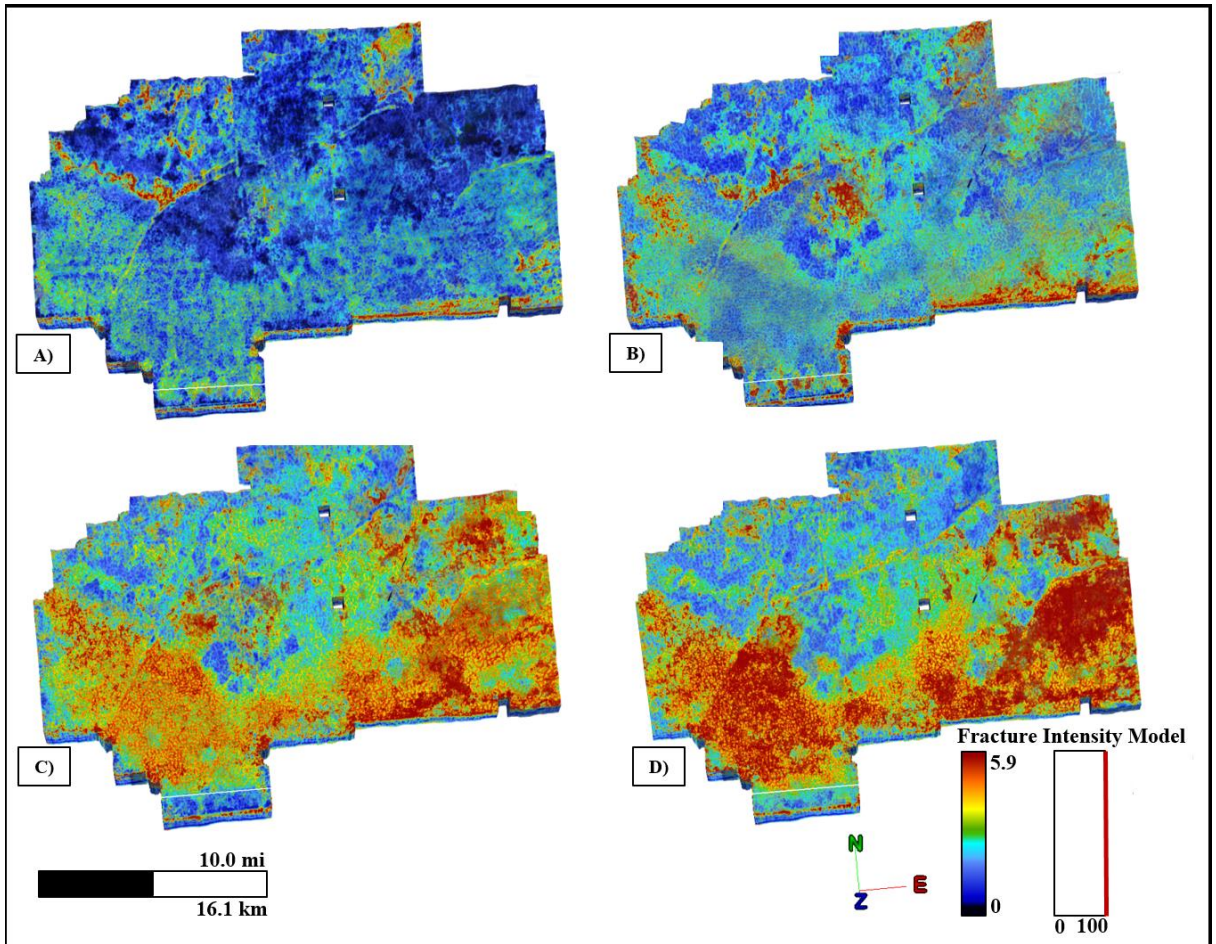

Figure 39. This is the fracture intensity model for the Mississippian Limestone generated from the six seismic attributes at (A) the top of the Mississippian Limestone, (B) 50 ft into the Mississippian Limestone, (C) 100 ft into the Mississippian Limestone and, (D) 150 ft into the Mississippian Limestone. Fractures are apparent in the model along interpreted faults seen in figure A3. Within the first 150 ft of the Mississippian Limestone, fracture intensity increases with depth in southern extents of the survey while decreasing in northern extents of the survey.

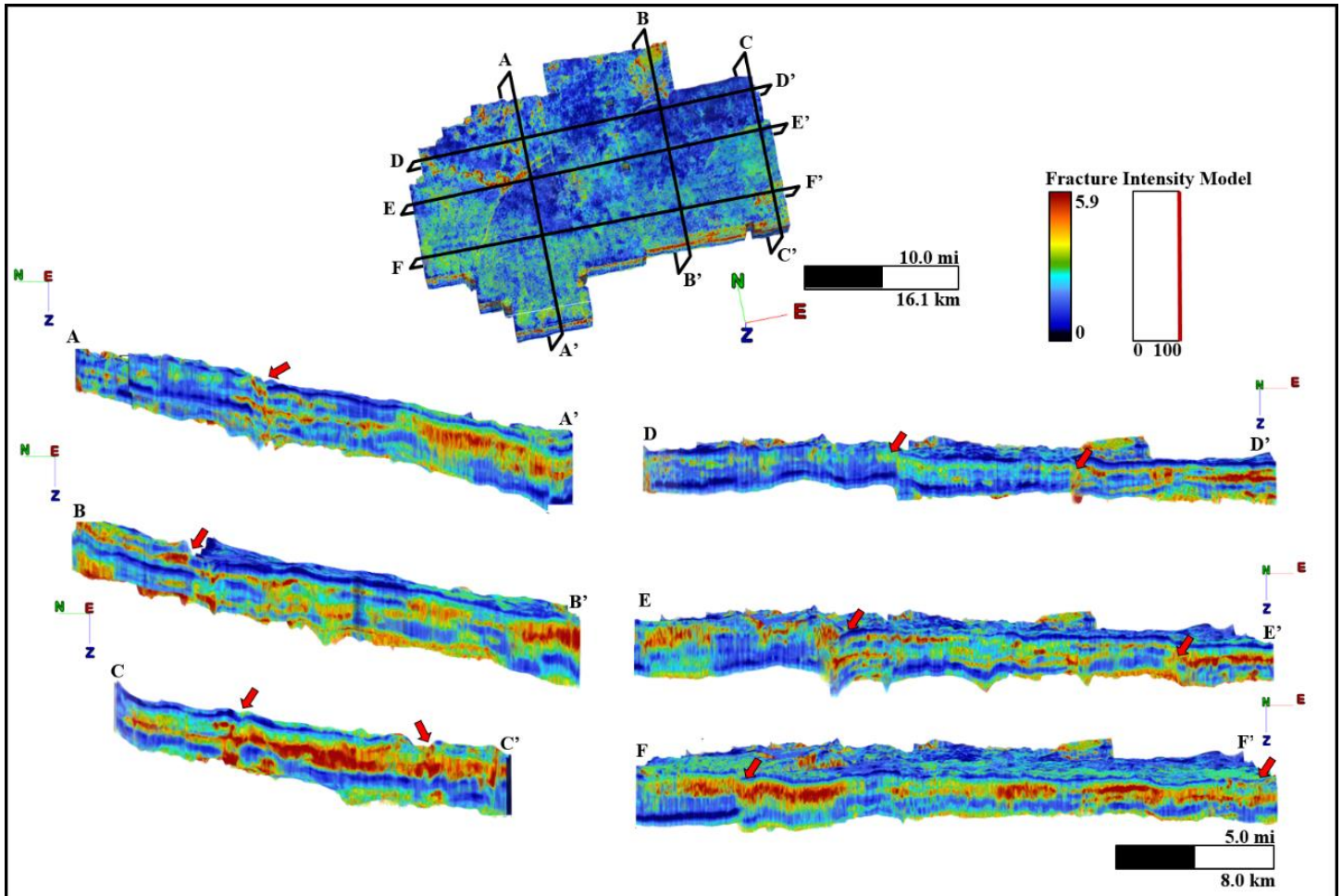

Figure 40. This is the fracture intensity model with cross sections north to south and east to west through the study zone. Red arrows indicate interpreted faults where there is a presence of higher fracture intensity. The high fracture intensity swaths run laterally instead of vertically through the section, which is expected considering amplitude and density were the most significant seismic attributes contributing to fracturing. This could be a result of fracturing being controlled by lithology changes throughout this heterogeneous formation.

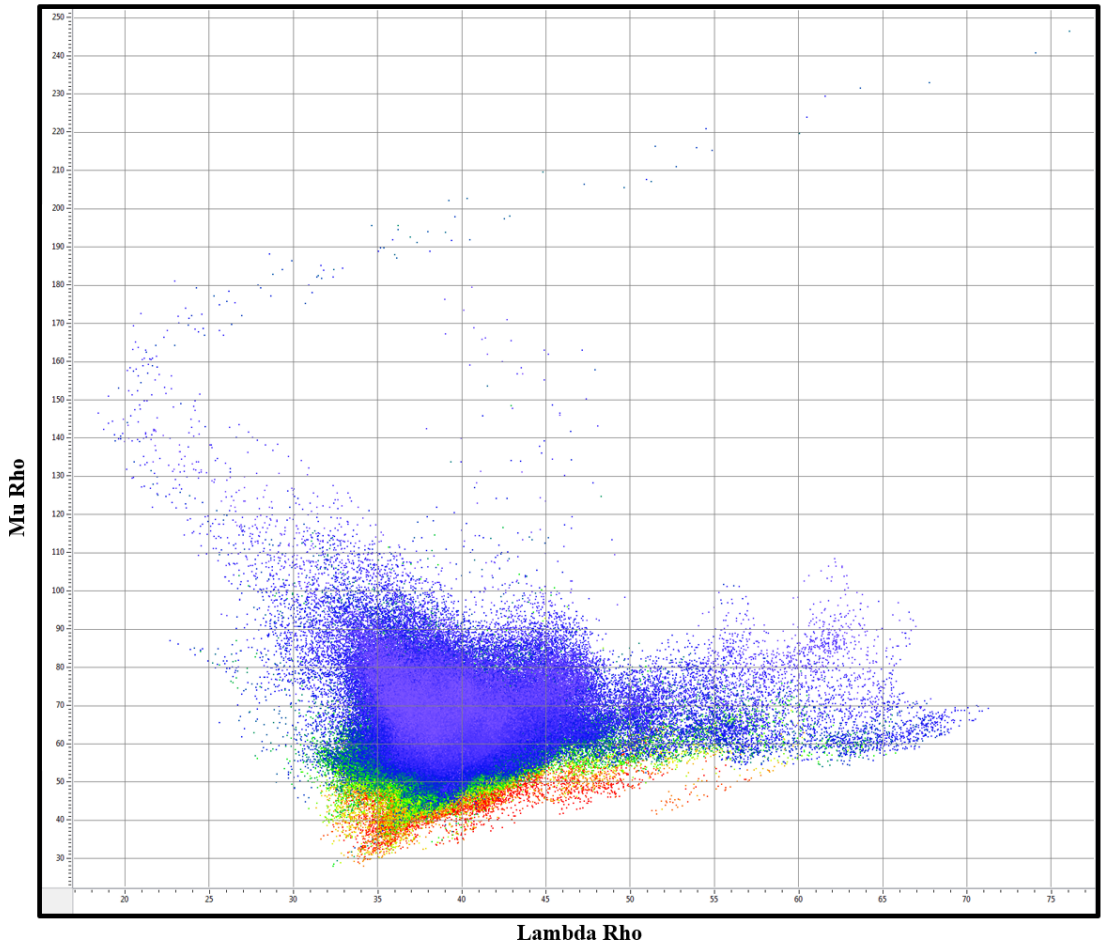

Figure 41. Lambda Rho and Mu Rho extracted from a surface 35 feet into the Mississippian Limestone were cross plotted and colored by fracture intensity. Fracture intensity is high with low shear strength and high compressional strength. The highly fractured areas can take more strain without further breaking.

Chapter 6: Fracture Model and Production Analysis

Now that the fracture model is generated throughout the entire seismic survey, the question of whether fracture intensity is related to production can be answered. First, the five wells with borehole image interpretation were examined for a correlation before fracture intensity and production. The average fracture area log that was interpreted was cross plotted against cumulative oil, cumulative gas, and cumulative water production. Only four of the five wells had water production, which was a fair positive correlation of 0.562 with an R-Squared value of 0.315. The fracture area logs for the five wells, cross correlated with oil production gave a negative correlation with a correlation coefficient of -0.638 and an R-Squared value of 0.407. Gas production essentially had no correlation with fractures with a correlation coefficient of 0.121 and an R-Squared value of 0.0145 (Figure 42). Analysis of a stimulate reservoir was then done, assuming a radius of 250 ft and a half height of 50 ft for the five wells with interpreted borehole images. The outcome for a stimulated reservoir remained similar. Water production and fractures had a positive correlation with a correlation coefficient of 0.403 and a R-Squared value of 0.162. Oil continued to have a negative correlation with fractures, at -0.598 and an R-Squared value of 0.358. Lastly, gas continued to have essentially no correlation with fractures with a -0.111 correlation coefficient and an R-Squared value at 0.0122 (Figure 43).

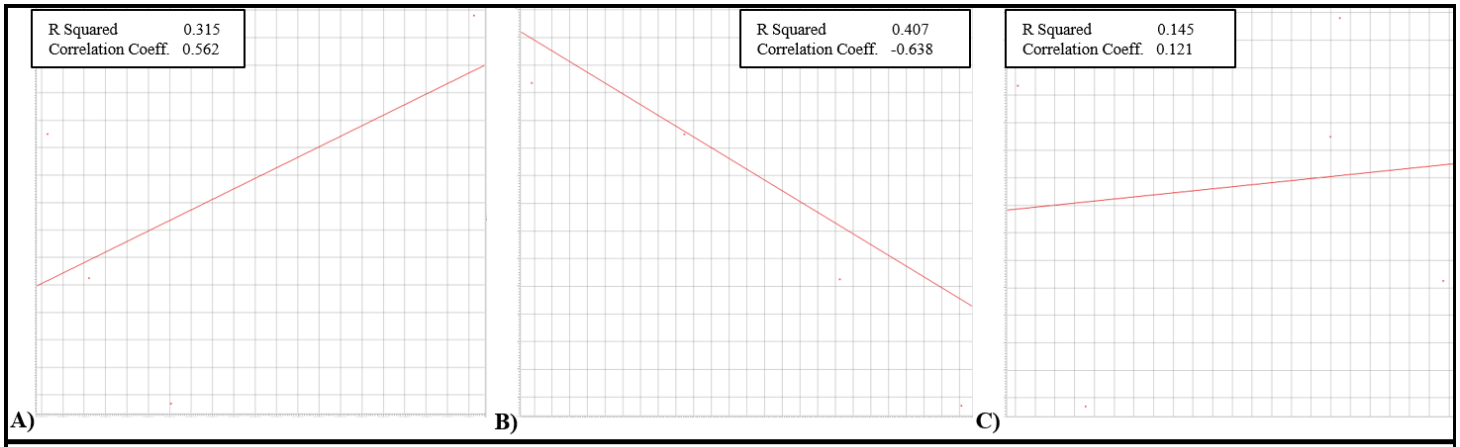

Figure 42. Cross plots of fractures interpreted on borehole image logs, correlated with scaled water, oil and gas production. A positive correlation is made for (A)water and (B) oil production, with a negative correlation to C) gas production. With fractures only extracted at the well, it would be beneficial to cross plot with fractures modeled around the borehole, to get an idea of correlation with stimulated reservoir.

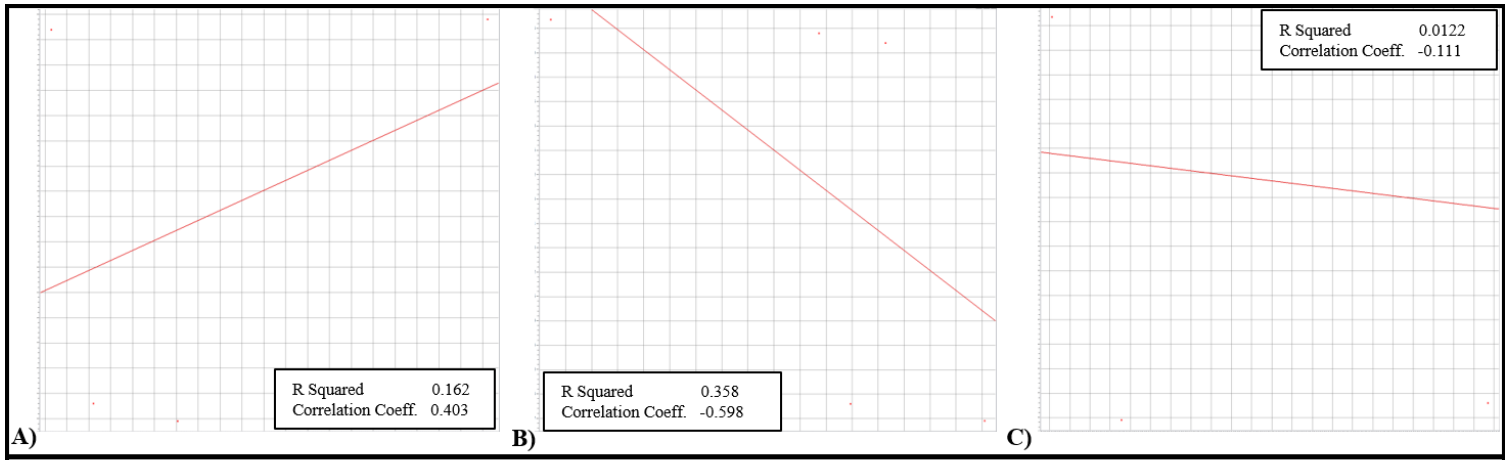

Figure 43. Cross plots of modeled fractures of the five interpreted borehole image wells, correlated with scaled water, oil and gas production, with a stimulated reservoir taken into account. A positive correlation is made for (A) water, with a negative correlation to (B) oil production (C) gas. With fractures only extracted for the five originally interpreted wells, it is beneficial to cross plot with a larger sample of wells in the survey next.

With the first to analyses of fractures with production, only five wells were being analyzed. To increase confidence in correlations, 77 wells with production values were analyzed. The first two analyses were done with actual interpretation against production. The following correlations were done on modeled fractures, based off of the multi-variate nonlinear regression model. Modeled values were extracted along the Mississippian section of boreholes and averaged. Those average values were then cross correlated with oil, gas, and water scaled production values provided. With the 77 wells, horizontal wells, water essentially had no correlation with fractures with a correlation coefficient of -0.175 and an R-Squared value of 0.0307. Oil had even less of a correlation with fractures with a correlation coefficient of -0.0213 and an R-Squared value of 0.000452. Lastly, gas had a slightly negative correlation of -0.182 and an R-Squared value of 0.0331 (Figure 44). Other mathematical methods were used for generating a fracture scalar for each well, including maximum value, mode, and median. No matter which mathematical method was used to get a fracture intensity scalar to correlate with production, the outcome was extremely similar. Essentially no correlations were found for water, oil, or gas to fractures.

New analyses were done on the 77 wells, taking stimulation of the reservoir into account. First, values were extracted not just along the wellbores, but also took into account a stimulation of 250 foot radius and a 50 foot half height. There was not much of a change in correlation, even with a stimulated reservoir taken into account. Cumulative water production cross plotted with modeled fractures received a poor correlation of only -0.182 with a R-Squared value of 0.0331. Oil production cross correlated with modeled fractures also had essentially no correlation when including

stimulated reservoir. The correlation coefficient for oil production again modeled fractures was -0.0139 and an R-Squared value of 0.000192. Lastly, cumulative gas production had just a slight negative correlation with a correlation coefficient of -0.218 and a R-Squared value of 0.0473 (Figure 45).

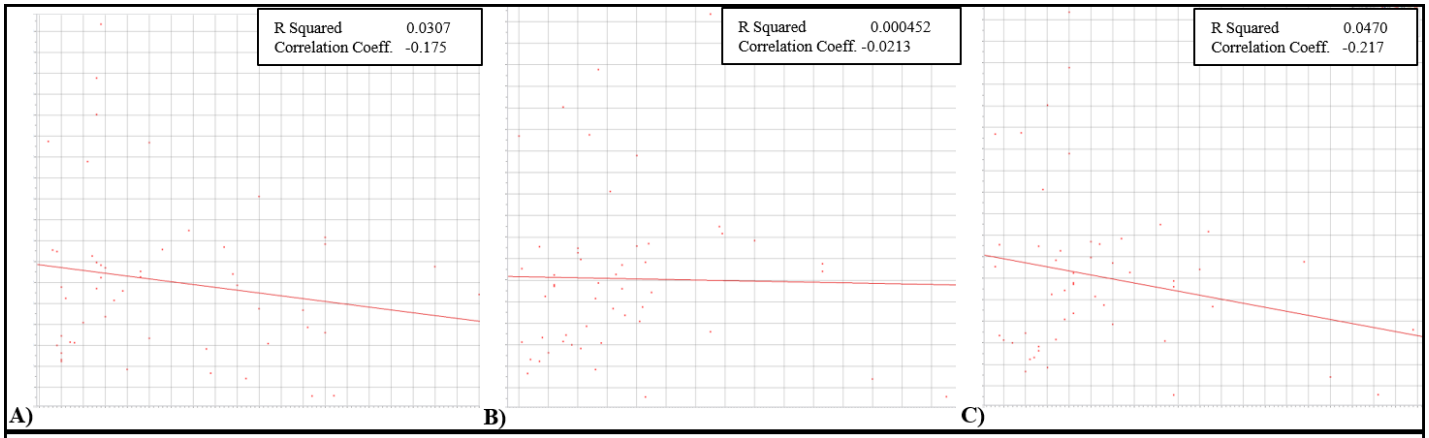

Figure 44. Cross plots of modeled fractures for 50 horizontal wellbores in the seismic survey, correlated with scaled water, oil and gas production. Essentially no correlation is made for (A) water production, (B) oil production or (C) gas. With fractures only extracted at the wellbores, it would be optimal to extract modeled fractures for the higher well count, while also taking a stimulated reservoir into account.

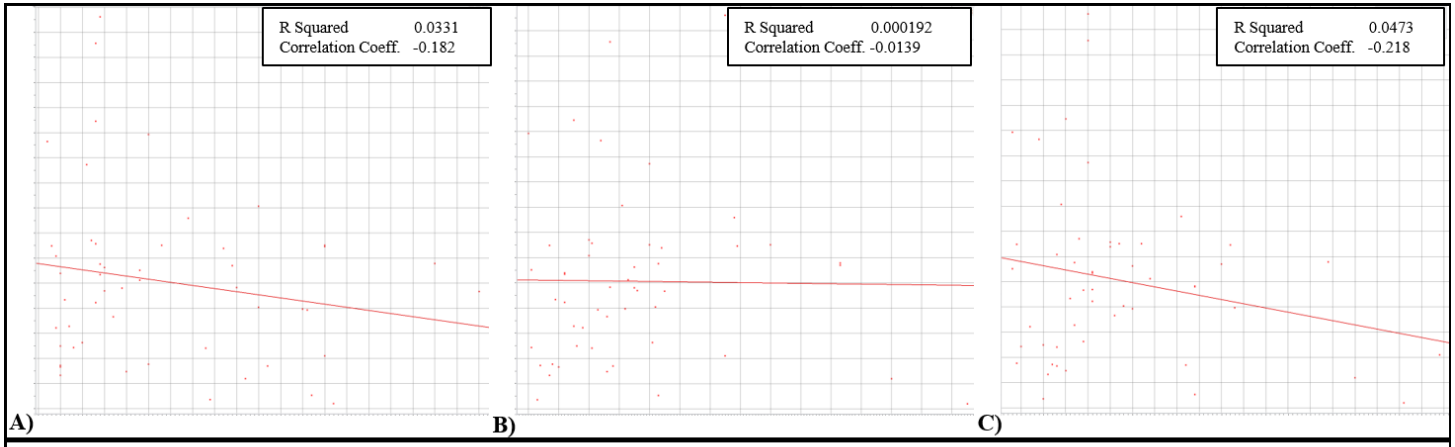

Figure 45. Cross plots of modeled fractures for 50 horizontal wellbores in the seismic survey, correlated with scaled water, oil and gas production, with a stimulated reservoir taken into account. Essentially no correlation is made for (A) water production, (B) oil production or (C) gas. With varying engineering and production variables unknown, it difficult to correlate fractures with production. If wells with similar production and completion methods were compared for the first well drilled in a section, an accurate correlation could be made.

When plotting cumulative water production against the fracture intensity model (Figure 46), a general trend is not apparent. Further inspection was done on two wells right next to each other, one with a large amount of water production and the other with very little water production. The well with a large amount of water production has very little, and even less fracture intensity that the well just east of it, which has much less water production.

Cumulative oil production was plotted on modeled fracture intensity (Figure 47). Once again, no visual correlation can be seen between fractures and cumulative oil production. With closer inspection of two wells on the west side of the north-south normal fault, the well to the north has more cumulative oil production than the well south of it. Inspection of the well with higher oil production in the fracture intensity model shows higher fracture intensity at the top of the Mississippian Limestone and at the end of its lateral. The fracture model of the well with less oil production does in fact have less fracture intensity, when comparing just these two wells.

Cumulative gas production was plotted on modeled fracture intensity (Figure 48). Once again, no production trend is apparent. There are two horizontal wells that lie just south of the northeast-southwest normal fault, one with more gas production than the other. The well to the northeast with larger gas production may have slightly more fracture intensity throughout the lateral. The well with the lower gas production has higher fracture intensity just in one swath towards the end of the lateral, but minimal fractures along the rest of the lateral.

There are several limitations when attempting to correlate production in the Mississippian Limestone. Many of the wells in this play are choked back by engineers,

have different tubing sizes, or curtail production due to pipeline over flooding. With these varying engineering elements, an accurate production correlation is difficult. It would be ideal to find wells that had similar completion and production methods, and were the first well drilled in their section. This would give a much more accurate idea of how fracturing correlates with production.

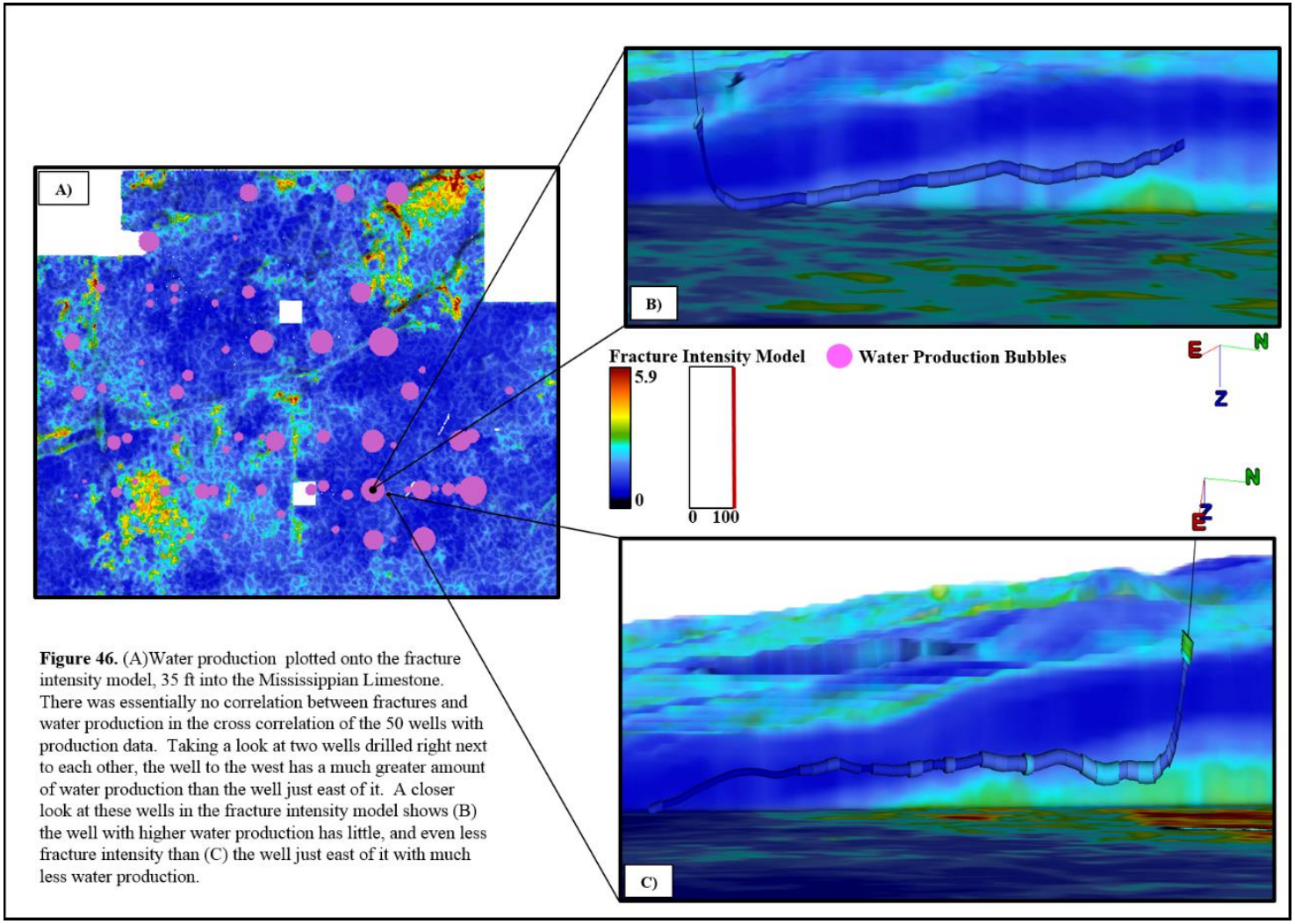

Figure 46. (A)Water production plotted onto the fracture intensity model, 35 ft into the Mississippian Limestone. There was essentially no correlation between fractures and water production in the cross correlation of the 50 wells with production data. Taking a look at two wells drilled right next to each other, the well to the west has a much greater amount of water production than the well just east of it. A closer look at these wells in the fracture intensity model shows (B) the well with higher water production has little, and even less fracture intensity than (C) the well just east of it with much less water production.

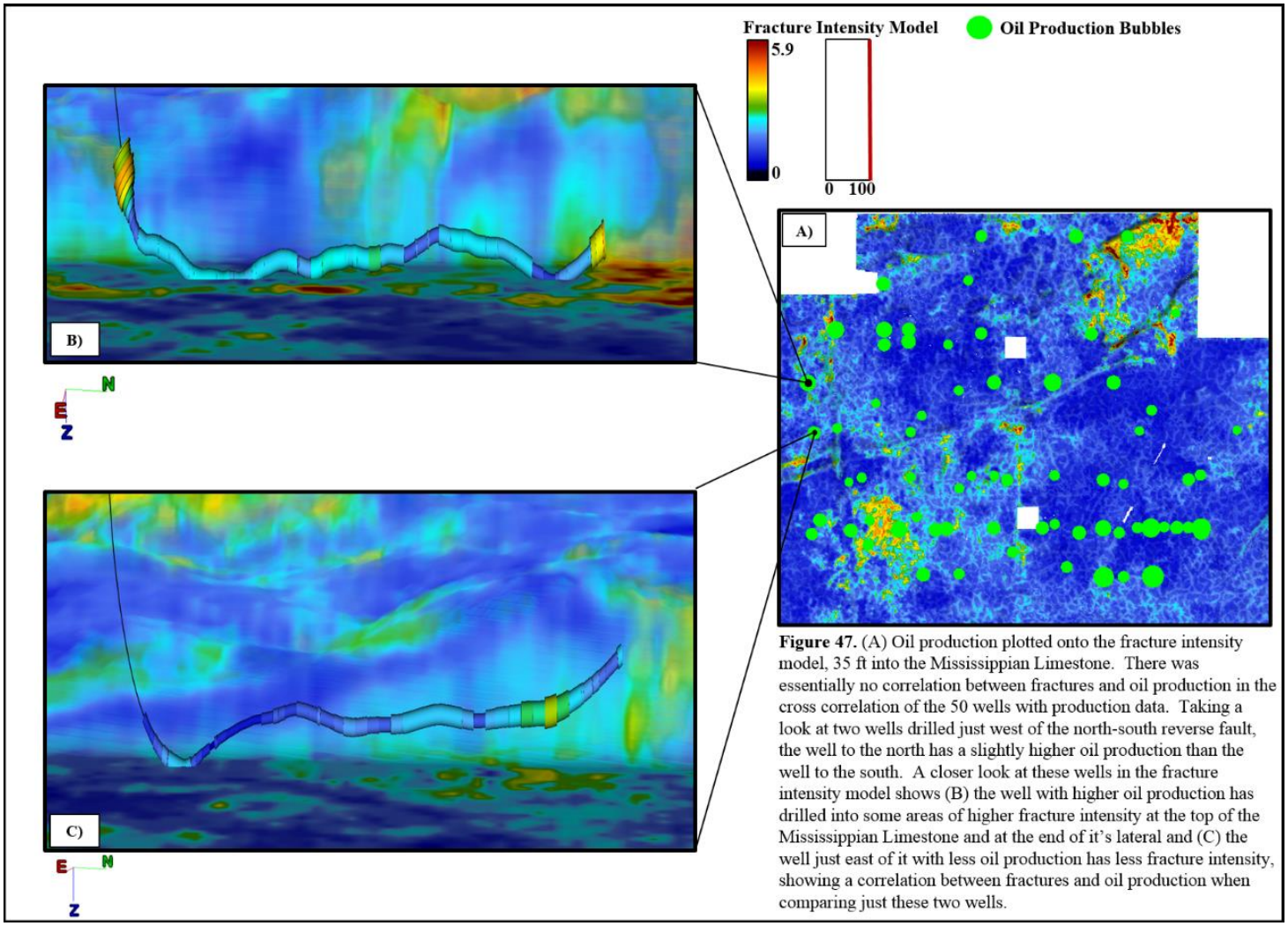

Figure 47. (A) Oil production plotted onto the fracture intensity model, 35 ft into the Mississippian Limestone. There was essentially no correlation between fractures and oil production in the cross correlation of the 50 wells with production data. Taking a look at two wells drilled just west of the north-south reverse fault, the well to the north has a slightly higher oil production than the well to the south. A closer look at these wells in the fracture intensity model shows (B) the well with higher oil production has drilled into some areas of higher fracture intensity at the top of the Mississippian Limestone and at the end of it's lateral and (C) the well just east of it with less oil production has less fracture intensity, showing a correlation between fractures and oil production when comparing just these two wells.

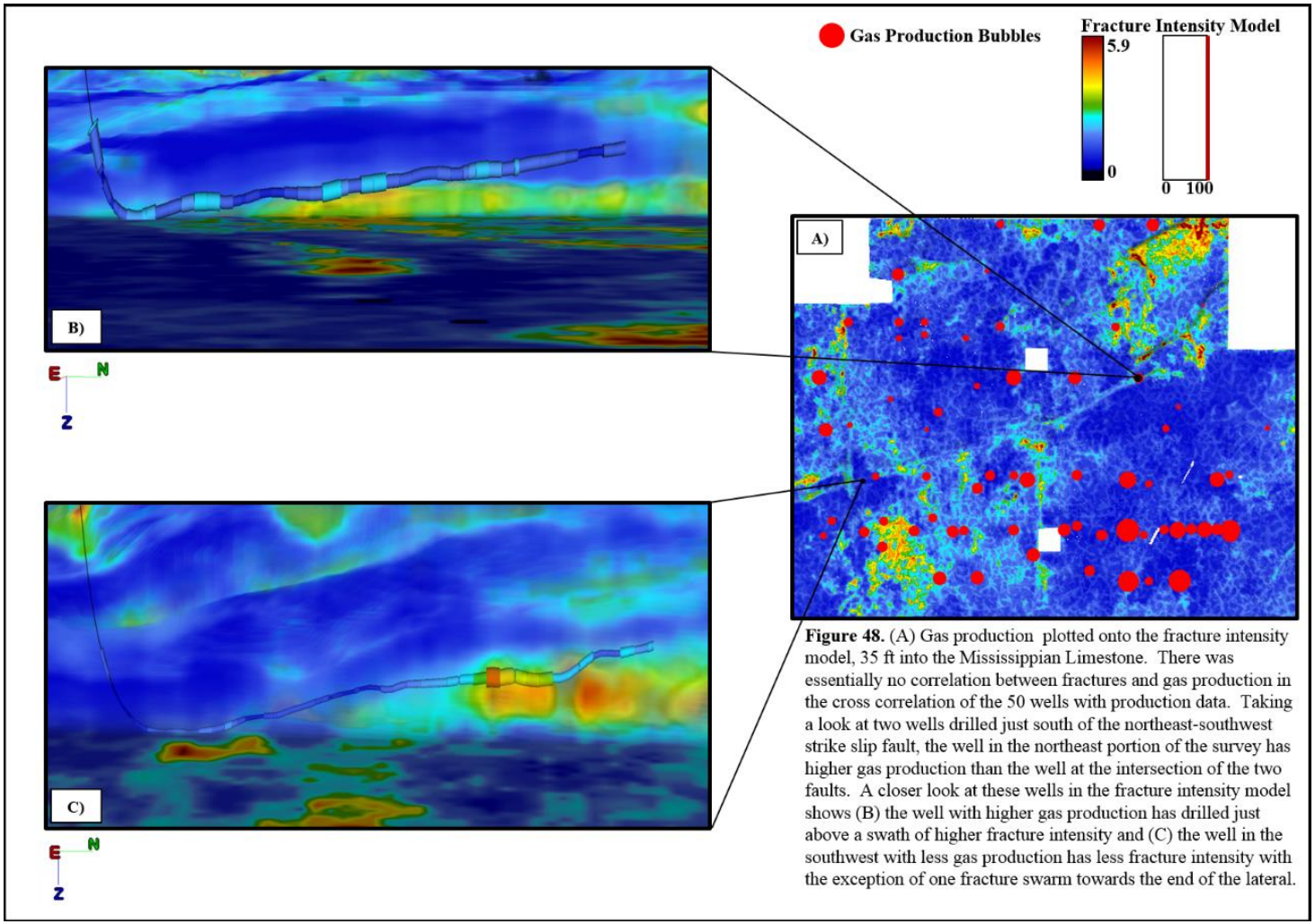

Figure 48. (A) Gas production plotted onto the fracture intensity model, 35 ft into the Mississippian Limestone. There was essentially no correlation between fractures and gas production in the cross correlation of the 50 wells with production data. Taking a look at two wells drilled just south of the northeast-southwest strike slip fault, the well in the northeast portion of the survey has higher gas production than the well at the intersection of the two faults. A closer look at these wells in the fracture intensity model shows (B) the well with higher gas production has drilled just above a swath of higher fracture intensity and (C) the well in the southwest with less gas production has less fracture intensity with the exception of one fracture swarm towards the end of the lateral.

Chapter 7: Conclusions

The Mississippian Limestone reservoir along the Anadarko shelf is an extremely fractured and heterogeneous reservoir, with lithologies changing quickly and multiple times observed in five borehole images. Within the borehole images, three lithologies and five rock types were identified: chert, cherty limestone, limestone, highly fractured limestone, and collapse features. The majority of the fractures seen in borehole images were conductive fractures with a strike of northeast-southwest. Karst collapse features were also seen in eleven areas along the borehole images, with some large scale collapse features, and many smaller collapse features.

A suite of complex trace, geometric, and impedance attributes were generated throughout a seismic volume containing the interpreted borehole image logs. With the use of multivariate non-linear regression statistics, six seismic attributes out of the original twenty were used to model fractures seen on the image logs throughout the seismic survey. Of these attributes, the complex trace attributes showed that fracture intensity increased with decreasing instantaneous frequency and envelope, likely due to increased attenuation and scattered seismic energy in highly fractured areas. An important attribute in modeling fractures was a density volume generated from prestack inversion. The geometric attributes that aided in fracture modeling were variance, dip azimuth, and long wavelength most negative curvature. Variance highlighted an increase in fractures in faulted regions. Dip azimuth illustrated that fracture intensity increased when reflectors dipped to the north and northeast. Lastly, long wave length most negative curvature had a strong correlation with fractures, consistent with highly fractured rock in collapse features.

With the generated fracture intensity model, higher fracture intensity was observed along previously mapped faults. Higher fractures were also observed in areas where there are known deposits of tripolitic chert. There is also an increase in fractures along a large swath across southern portions of the survey that have low instantaneous frequency.

Attempts to correlate oil, water, and gas production with fracture intensity proved to have little to no correlation. In such a heterogeneous and complicated reservoir, other geological and engineering factors must be considered and a more expansive statistical study incorporating seismic, geologic, and engineering variables appears necessary to better predict production.

References

Alzate, J.H., R. Perez, D. Devegowda, K.J. Marfurt, 2012, The value of production logging combined with 3D surface seismic in unconventional plays characterization: 82nd Annual Meeting, SEG, Expanded Abstracts, 1-5.

Blakey, R., 2016, Paleogeography: http://jan.ucc.nau.edu/~rcb7/index.html, (accessed February 27, 2016).

Bosworth, T.O., 1920, Geology of the Mid Continent Oilfields, Kansas, Oklahoma and North Texas, p. 19-20.

Chopra, S., and K.J. Marfurt, 2007, Seismic Attributes for Prospect Identification and Reservoir Characterization, p. 27-43.

Downton, J., B. Roure, and L. Hunt, 2011, Azimuthal Fourier Coefficients: CSEG Recorder, 36, no. 10, 22-36.

Elrafie, E.A., S.D. Russell, G. Vassilellis, R.S. McCarty, J.W. Austin, and F. Medellin, 2015, Natural fracture detection characterization and modeling in a tight oil carbonate resource enables through multi-disciplinary integration, targeted development and enhanced overall resource performance: Presented at Unconventional Resources Technology Conference, 1144-1155.

Goldstein, R. and B. King, 2014, History of hydrothermal fluid flow in the Midcontinent: A key to understanding the origin and distribution of porosity: Search and Discovery Article #50958.

Holman, R., 2014, Seismic characterization of fractured rock fabric in Mississippian limestone, Payne county Oklahoma: M.S. thesis, Oklahoma State University.

Hunt, L., S. Reynolds, T. Brown, S. Hadley, J. Downton, and S. Chopra, 2010, Quantitative estimate of fracture density variations in the Nordegg with azimuthal AVO and curvature: A case study: The Leading Edge, v. 29, 1122–1137, doi:10.1190/1.3485773.

Hunt, L., S. Reynolds, T. Brown, S. Hadley, J. Downton,, and S. Chopra, 2011, Quantitative estimates of fracture density variations: further perspectives: Presentation: http://cseg.ca/technical/view/quantitative-estimates-of-fracture-density-variations-further-perspectives (accessed February 27, 2016).

Hurley, N., 2004, Borehole images: Basic Well Log Analysis, AAPG Methods in Exploration, v. 16, 151-163.

Lindzey, K., 2015, Geologically constrained seismic characterization and 3-D reservoir modeling of Mississippian reservoirs, north-central Anadarko shelf, Oklahoma: M.S. thesis, the University of Oklahoma.

Manger, W. L., 2011, Lower Mississippian Sequence Stratigraphy and Depositional Dynamics: Insights from the Outcrops, Northwestern Arkansas and Southwestern Missouri: Presentation, http://ogs.ou.edu/MEETINGS/Presentations/Miss2011/Manger.pdf (accessed August 21, 2013).

Manger, W.L., 2014, Tripolitic Chert Development in the Mississippian Lime: New Insights from SEM: AAPG Mississippi Lime Forum.

Marfurt, K.J., 2015, Techniques and best practices in multiattribute display: Interpretation, v. 3, no. 1, doi: 10.1190/INT-2014-0133.1.

Mazzullo, S.J., 2011, Mississippian oil reservoirs in the southern Midcontinent: new exploration concepts for a mature reservoir objective: Search and Discovery #10373.

Montgomery, S. L., J. C. Mullarkey, M. W. Longman, W. M. Colleary, and J. P. Rogers, 1998 Mississippian "Chat" Reservoirs, South Kansas: Low-Resistivity Pay in a Complex Chert Reservoir: AAPG Bulletin, v. 82, p. 187-205.

Motulsky, H.J., and L.A. Ransnas, 1987, Fitting curves to data using nonlinear regression: a practical and nonmathematical review: Federation of American Societies for Experimental Biology, v. 1, 365-374.

Nelson, R.A., 2001, Geologic analysis of naturally fractured reservoirs: Boston, Gulf Professional Pub.

Parham, K. and R. Northcutt, 1993, MS-3. Mississippian Chert and Carbonate and basal Pennsylvanian Sandstone-central Kansas Uplift and northern Oklahoma, in Bebout, D. G., W. A. White, and T. F. Hentz, eds., Atlas of Major Midcontinent Gas Reservoirs, Austin, Texas, Bureau of Economic Geology, p. 57.

Rogers, J. P. and M. W. Longman, 2001, An introduction to chert reservoirs of North America: AAPG Bulletin, v. 85, p. 1-5.

Rogers, J. P., M. W. Longman, and R. M. Lloyd, 1995, Spiculitic Chert Reservoir in Glick Field, South-Central Kansas: The Mountain Geologist, v. 32, p. 1-22.

Rogers, S. M., 2001, Deposition and diagenesis of Mississippian chat reservoirs, north central Oklahoma, AAPG bulletin, v. 85, p. 115-129.

Roy, A., B.L. Dowdell, and K.J. Marfurt, 2013, Characterizing a Mississippian tripolitic chert reservoir using 3D unsupervised and supervised mutliattribute seismic facies analysis: An example from Osage County, Oklahoma: Interpretation, v. 1, 109-124, doi: 10.1190/INT-2013-0023.1.

Scotese, C. R., 1999, Paleomap Project Web site: http://www.scotese.com/ (accessed February 13, 2016).

Singleton, S., S. Chi, C. Lapaire, L. Sanford, and P. Constance, 2015, Integration of microseismic with rock properties from multi-component seismic data, Mississippi Lime play, north-central Oklahoma: Presented at Unconventional Resources Technology Conference, 2085-2096.

Smyth, G.K., 2002, Nonlinear Regression, Encyclopedia of Environmetrics, Volume Three, p. 1405-1411.

Stearns, V.G., 2015, Fracture characterization of the Mississippi Lime utilizing whole core, horizontal borehole images, and 3D seismic data from a mature field in Noble County, Oklahoma: M.S. thesis, the University of Oklahoma.

Taner, M.T., 2001, Seismic Attributes: CSEG Recorder, v. 26, p. 48-56.

Taner, M.T., F. Koehler, and R.E. Sheriff, 1979, Complex seismic trace analysis: Geophysics, v. 44, 1041-1063.

Thomas, M.A., 1982, Petrology and diagenesis of the Lower Mississippian, Osagean Series, western Sedgwick basin, Kansas: Kansas Geological Survey, Open-file Report 82-24, p. 87.

Trumbo, D.B., 2014, A production calibrated reservoir characterization of the Mississippi Lime in a mature field utilizing reprocessed legacy 3D seismic data, Kay County, Oklahoma: M.S. thesis, the University of Oklahoma.

Turnini, A.M., 2015, Stratigraphic and structural controls on Mississippian limestone and tripolitic chert reservoir distribution using seismic-constrained reservoir characterization and modeling, northern Oklahoma: M.S. thesis, the University of Oklahoma.

Walden, A.T., and R.E. White, 1998, Seismic wavelet estimation: A frequency domain solution to a geophysical noisy input-output problem: IEEE Transactions on Geoscience and Remote Sensing, v. 36, 287-297.

Watney, W. L, W. J. Guy, and A. P. Byrnes, 2001, Characterization of the Mississippian chat in south-central Kansas: AAPG Bulletin, v. 85, p. 85-113.

White III, H.G, 2013, Fracturing of Mississippi Lime, Oklahoma: experimental, seismic attributes and image logs analysis: M.S. thesis, the University of Oklahoma.

Witzke, B.J., and B.J. Bunker, 1996, Relative sea-level changes during Middle Ordovician through Mississippian deposition in the Iowa area, North American craton, in B.J. Witske, G.A. Ludvigson, and J. Day, eds., Paleozoic sequence stratigraphy: views from the North American craton: Geological Society of America Special Paper v. 306, p. 307-330.

Yenugu, M., and K.J. Marfurt, 2011, Relation between seismic curvatures and fractures identified from image logs – application to the Mississippian reservoirs of

Oklahoma, USA: 81st Annual International Meeting, SEG, Expanded Abstracts, 995-998.

Young, E.M., 2010, Controls on reservoir character in carbonate-chert strata, Mississippian (Osagean-Meramecian), southeast Kansas: thesis, the University of Nebraska.

Zoback, M.D., 2016, Reservoir Geomechanics, In situ stress and rock mechanics applied to reservoir processes: gp202.class.stanford.edu, (accessed March 20, 2016).

Appendix A: Seismic Interpretation and Depth Conversion

Seismic horizon interpretation and well log interpretation were done on the Mississippian Limestone, along with a shallower and deeper formation in the section. From these interpretations, average velocity models were generated and the seismic was then depth converted. The velocity models, depth converted surfaces, and an isopach are included in this appendix.

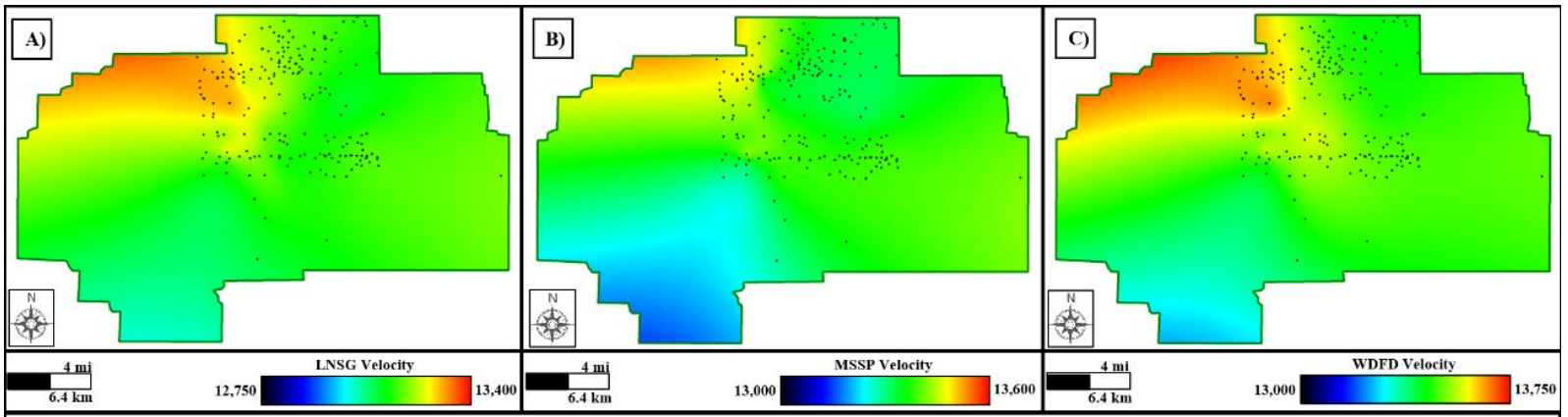

Figure A1. (A) The average velocity from the surface to the top of the Lansing Lime ranges from 13,030 ft/s in southern extents of the survey to 13,350 ft/s in the northwest. (B) The average velocity from the top of the Lansing Limestone to the top of the Mississippian Limestone ranges from 13,150 ft/s in the southwest to 13,530 ft/s in the northwest. (C) The average velocity for the entire Mississippian Limestone section ranges from 13,250 ft/s in the south to 13,700 ft/s in the northwest. The average velocity of the rock increases with depth.

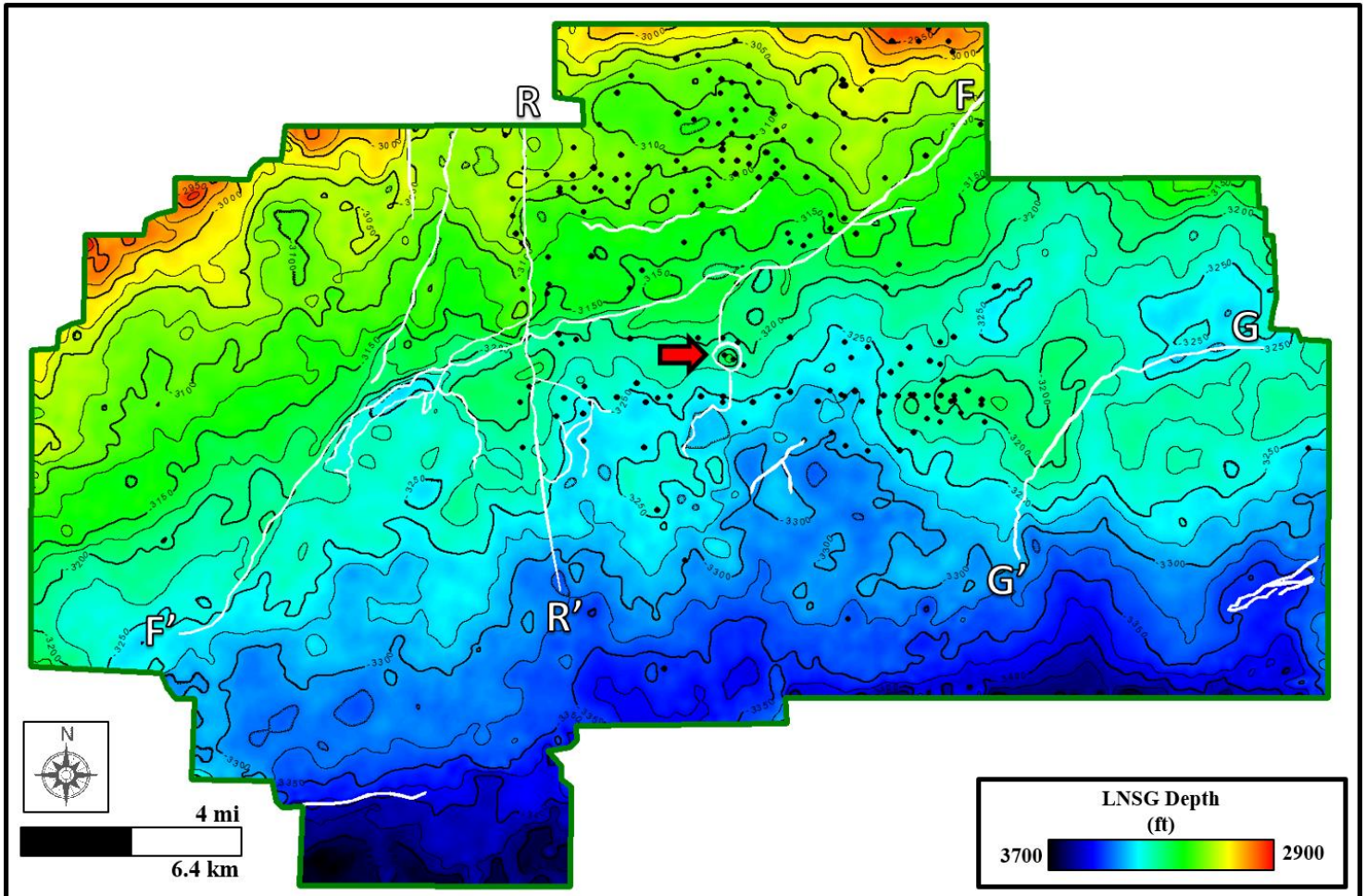

Figure A2. The depth structure map of the top of the Lansing Limestone, showing deepening to the south. The faulting seen at the Mississippian level (Figure 13), continues but exhibit less offset. The pop up structure in the center of the survey, highlighted with the red arrow, continues to shallower depths and penetrates the Lansing Limestone.

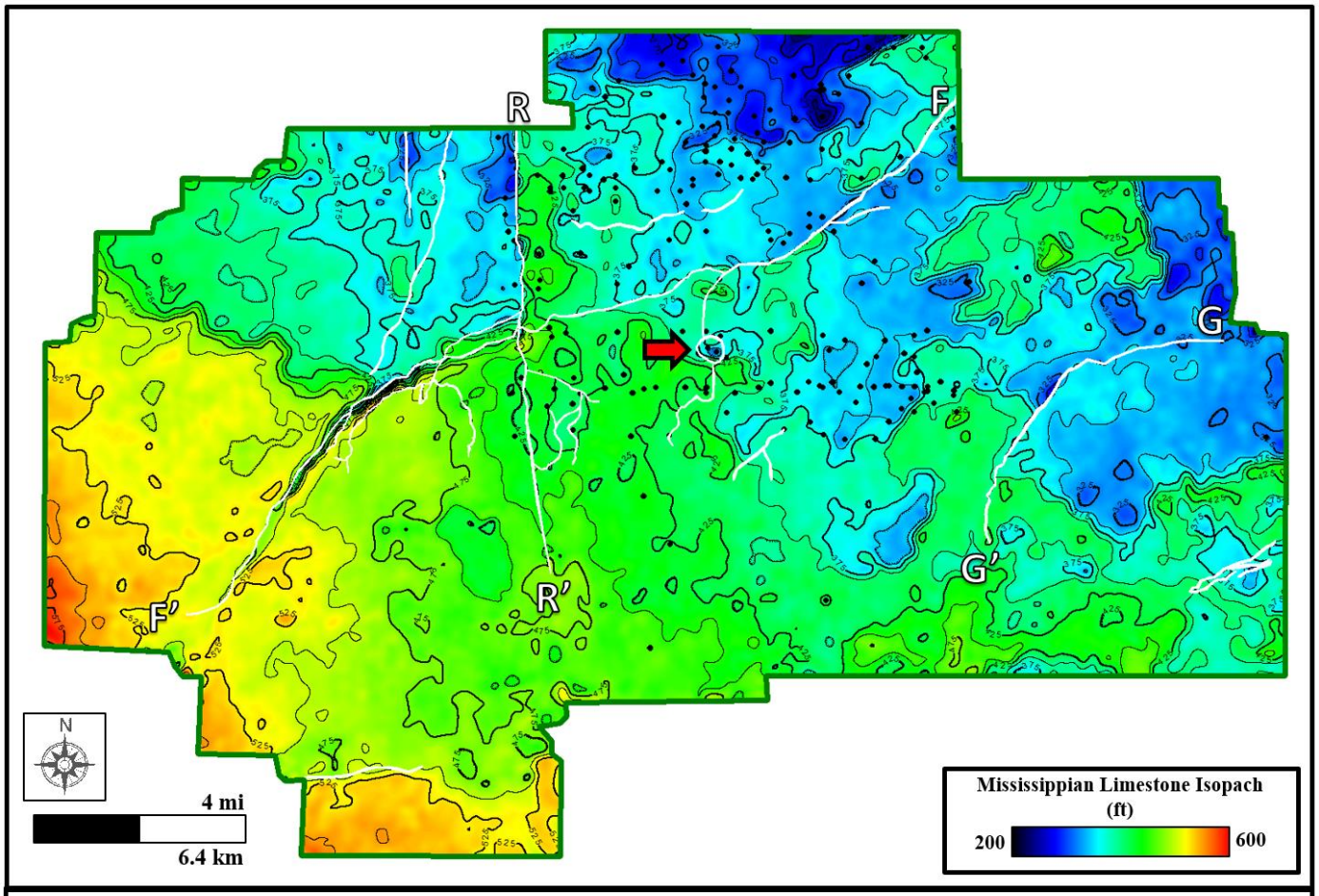

Figure A3. The thickness of the Mississippian Limestone, using the depth converted surfaces of the top of the Mississippian Limestone and the top of the Woodford Shale. The interpreted faults are displayed on top of the Mississippian Limestone isopach, highlighting the change in thickness from one side of the fault to the other. Especially the fault that runs from north to south in the north central portion of the study area is 100 ft thinner on the west side of the fault. The Mississippian Limestone ranges from 200 ft thick in the north to 600 ft in the southwest. The depth structure of the Mississippian Limestone is shown in Figure 13. The pop up structure in the center of the survey is highlighted by the red arrow.

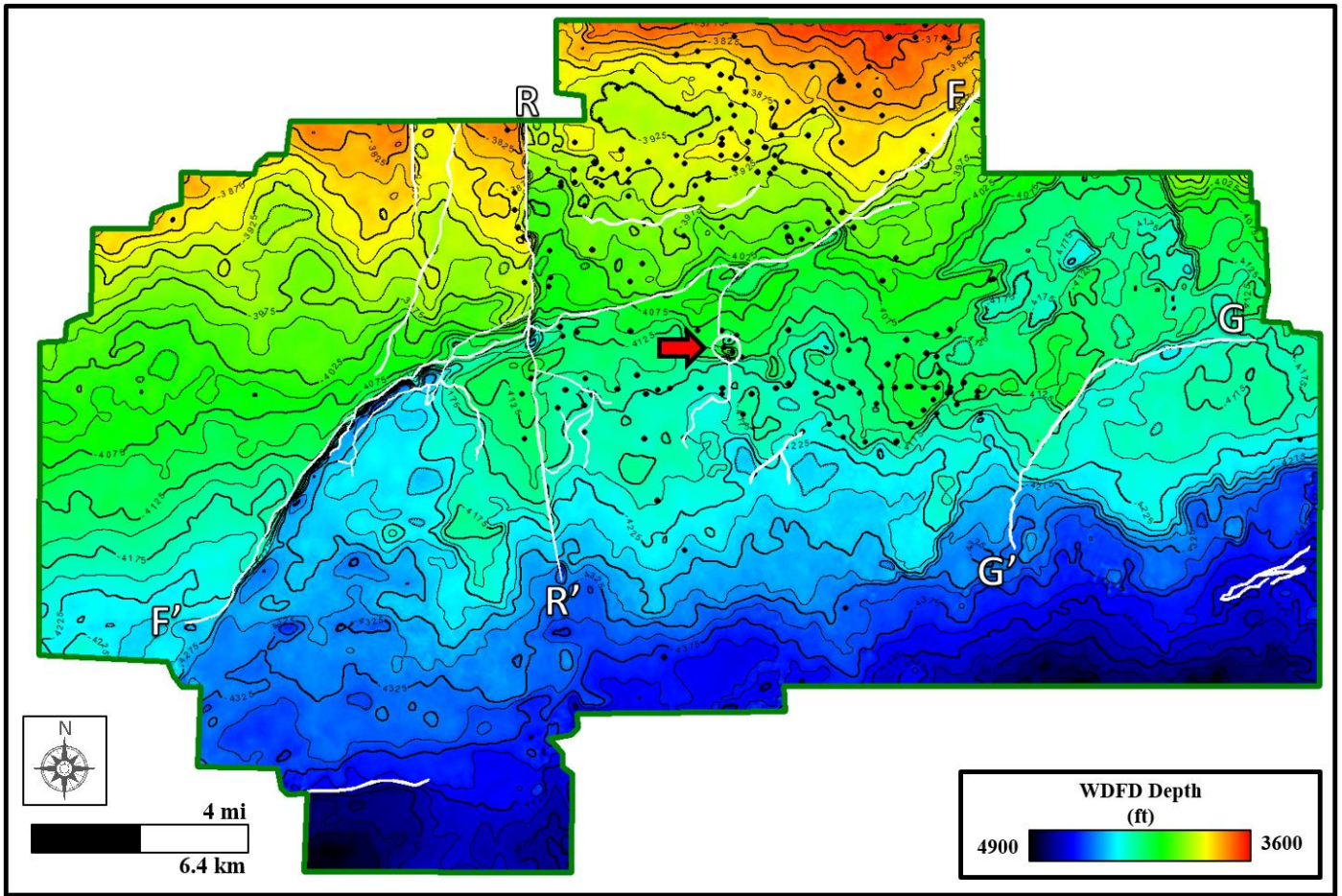

Figure A4. The depth converted structure map of the top of the Woodford Shale picked on seismic and then depth converted with formation top picks and an average velocity model. The structure map shows the Woodford Shale dipping deeper to the south to 4,900 ft subsea. The faulting in the study area has a larger offset in the Woodford Shale than in the shallower Mississippian Limestone. The pop up structure is also seen in the Woodford Shale, highlighted with the red arrow.

Appendix B: Borehole Image Interpretation

In this appendix I show the expression of conductive fractures. I also summarize several data limitations of borehole image interpretation. On borehole images, five lithology categories were created using visual and textural interpretation and confirmation with a photoelectric index log.

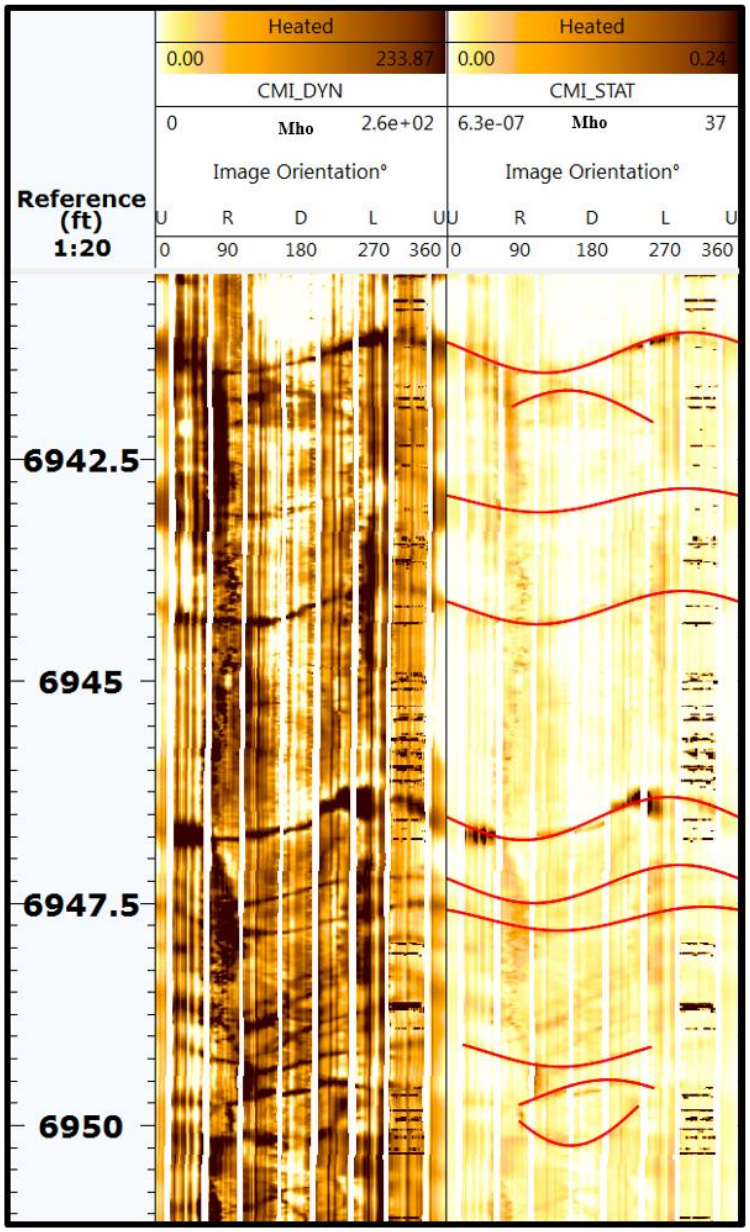

Figure B1. Limitation in interpreting fractures on borehole image logs. This particular borehole image had whitening in the image, making the image much less clear for picking fractures. The tool can only read a specific resistivity range. The whitening can result from really low mud resistivity.

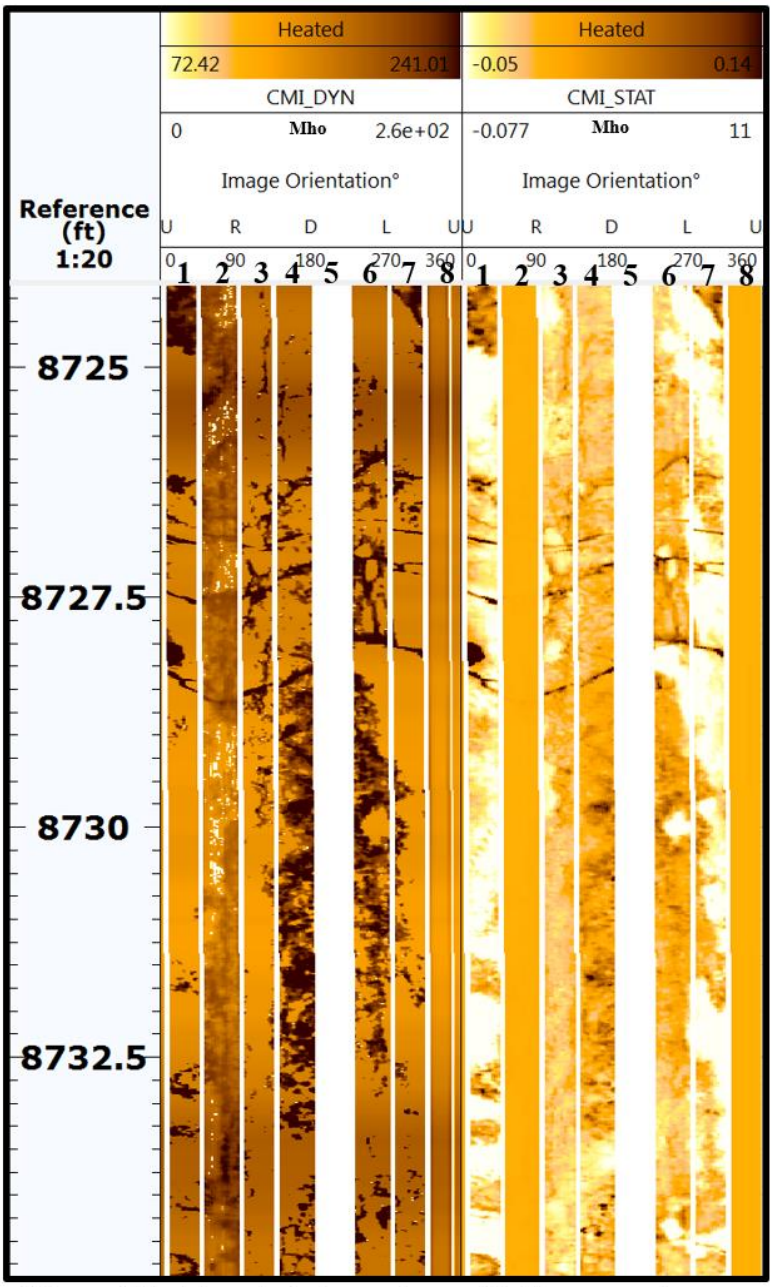

Figure B2. A borehole image log exhibiting several limitations when interpreting fractures. Track 5 on the image is missing. Tracks 2 and 8 of the image have corrupted resistivity images. This section is easier to interpret on the static image on the right, as opposed to the dynamic image on the left.

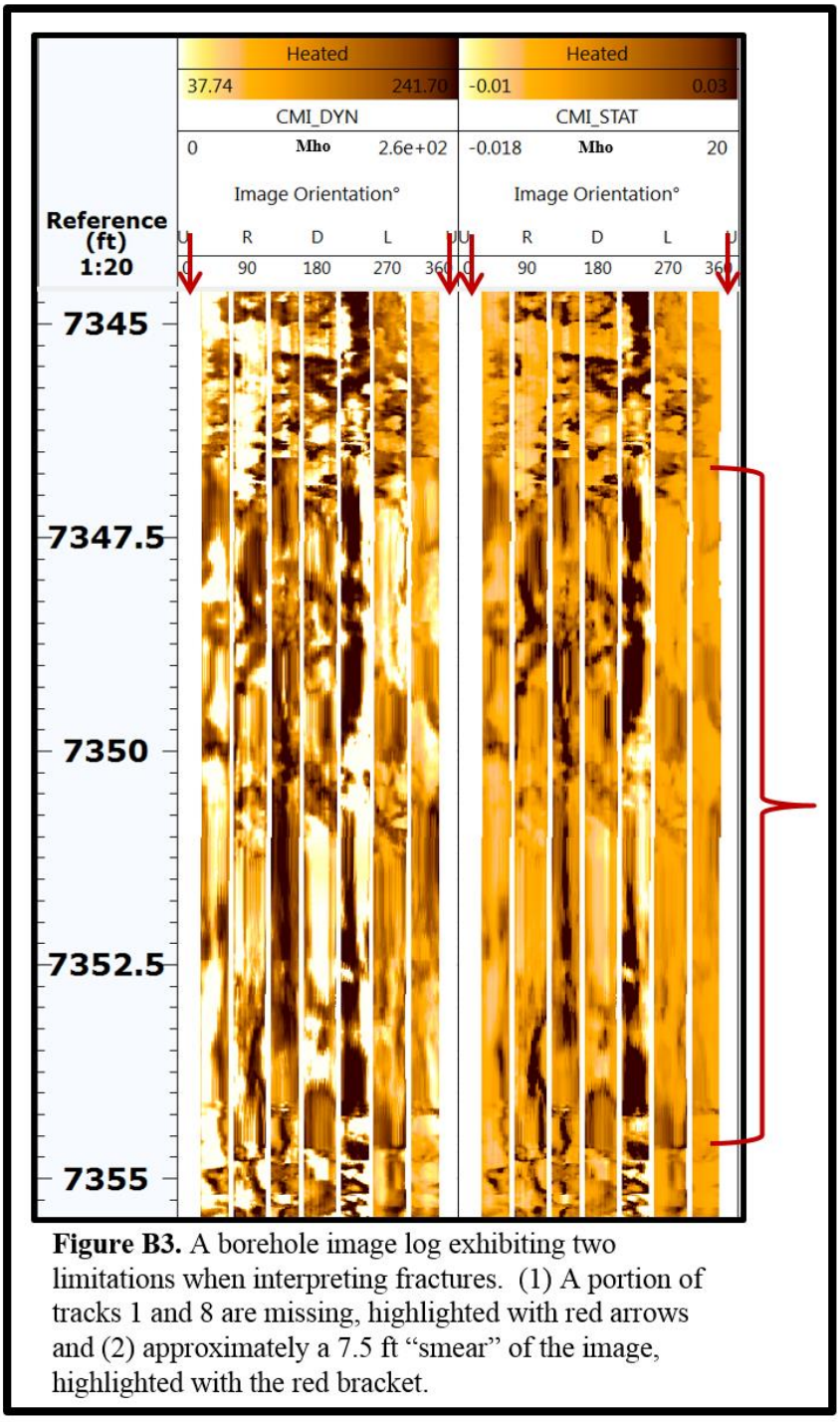

Figure B3. A borehole image log exhibiting two limitations when interpreting fractures. (1) A portion of tracks 1 and 8 are missing, highlighted with red arrows and (2) approximately a 7.5 ft "smear" of the image, highlighted with the red bracket.

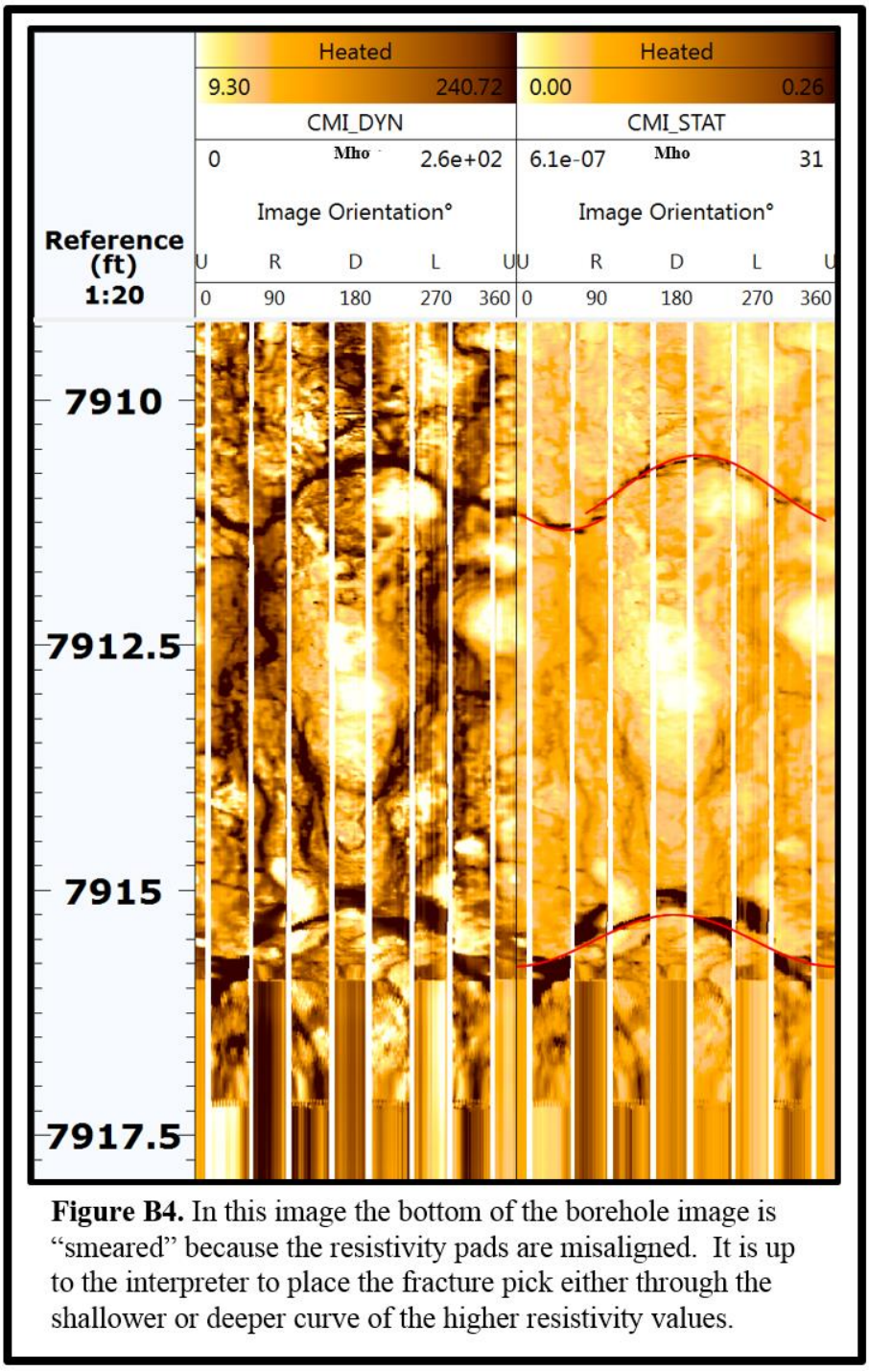

Figure B4. In this image the bottom of the borehole image is "smeared" because the resistivity pads are misaligned. It is up to the interpreter to place the fracture pick either through the shallower or deeper curve of the higher resistivity values.

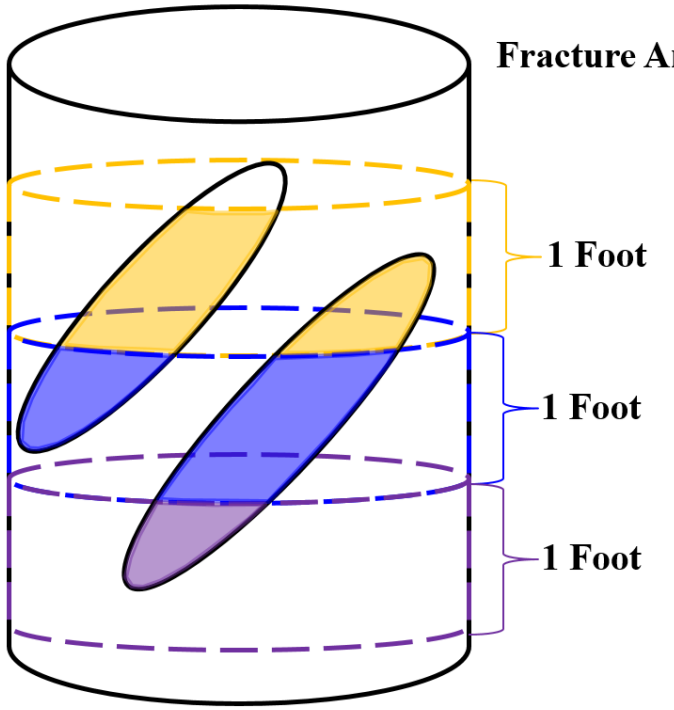

Figure B5. A schematic explaining the fracture area log that was generated based on the fracture interpretation. The fracture area logs were exported at 1 ft increment with a 1 ft step distance. Thus, the 1 ft of orange was exported out as the orange shaded area of fractures, divided by the volume of the orange cylinder.

Appendix C: Correlating 3D Seismic Data to Borehole Fractures

Five borehole images were interpreted and this section shows the difference between a conductive fracture and a mineralized, non-conductive fracture. Five lithology categories were created using visual and textural interpretation and confirmation with a photoelectric index log. The limitations of borehole image interpretation were described in this section, and can be seen in this appendix section. An explanation of the interpretation output, a fracture area log of the conductive fractures, is also illustrated in

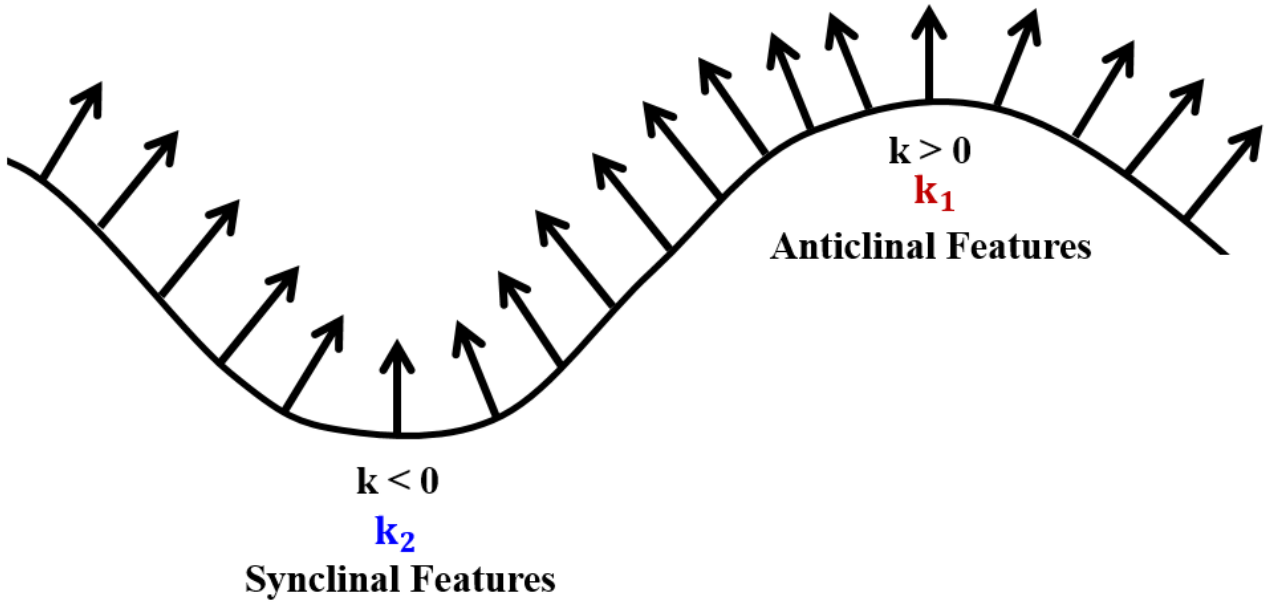

Figure C1. A schematic demonstrating most positive and most negative curvatures k_1 and k_2. Synclinal features are highlighted by k_2 and anticlinal features are highlighted by k_1. Both k_1 and k_2 were generated for both long wavelength and short wavelength to investigate statistically. The long wavelength volumes highlight large scale folds and features, while short wavelength volumes highlight small scale features (After Roberts, 2001).

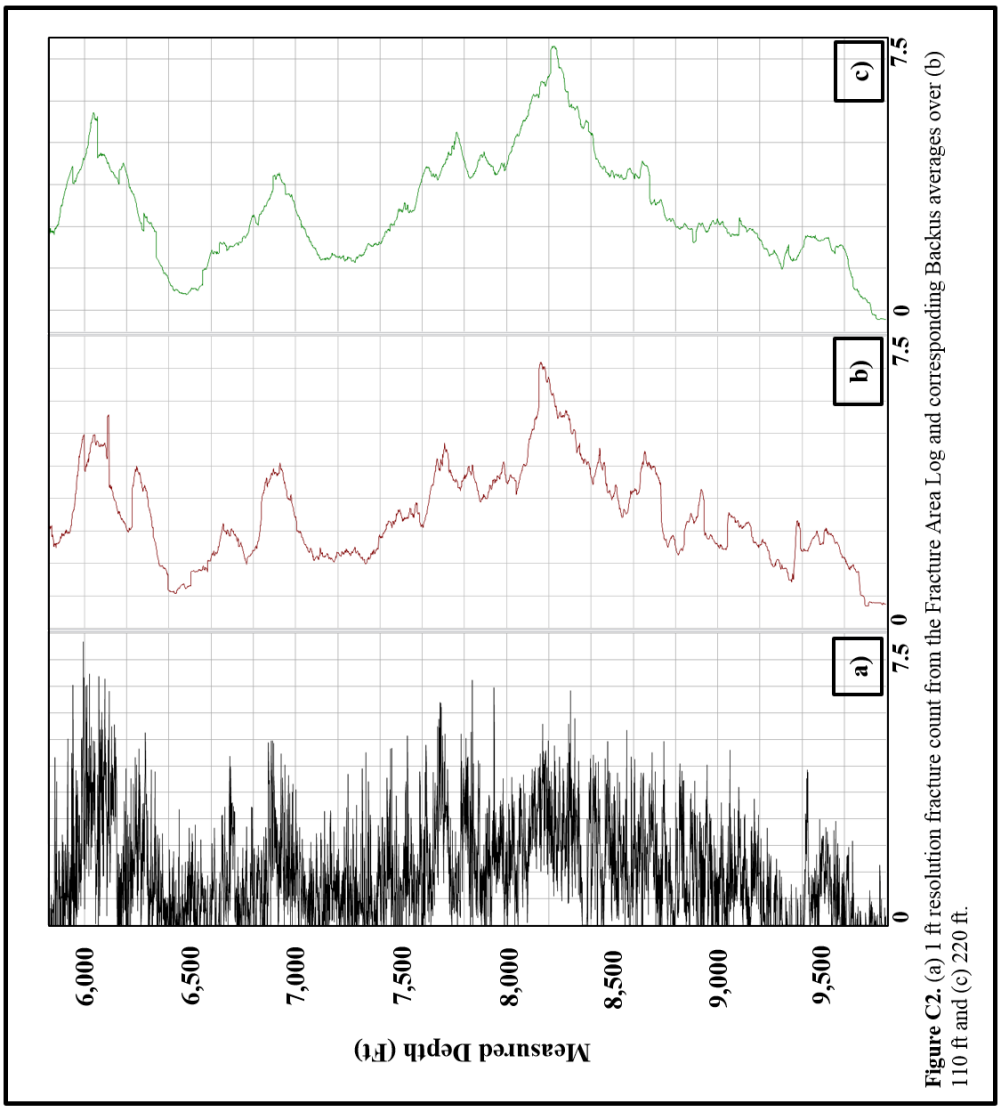

Figure C2. (a) 1 ft resolution fracture count from the Fracture Area Log and corresponding Backus averages over (b) 110 ft and (c) 220 ft.

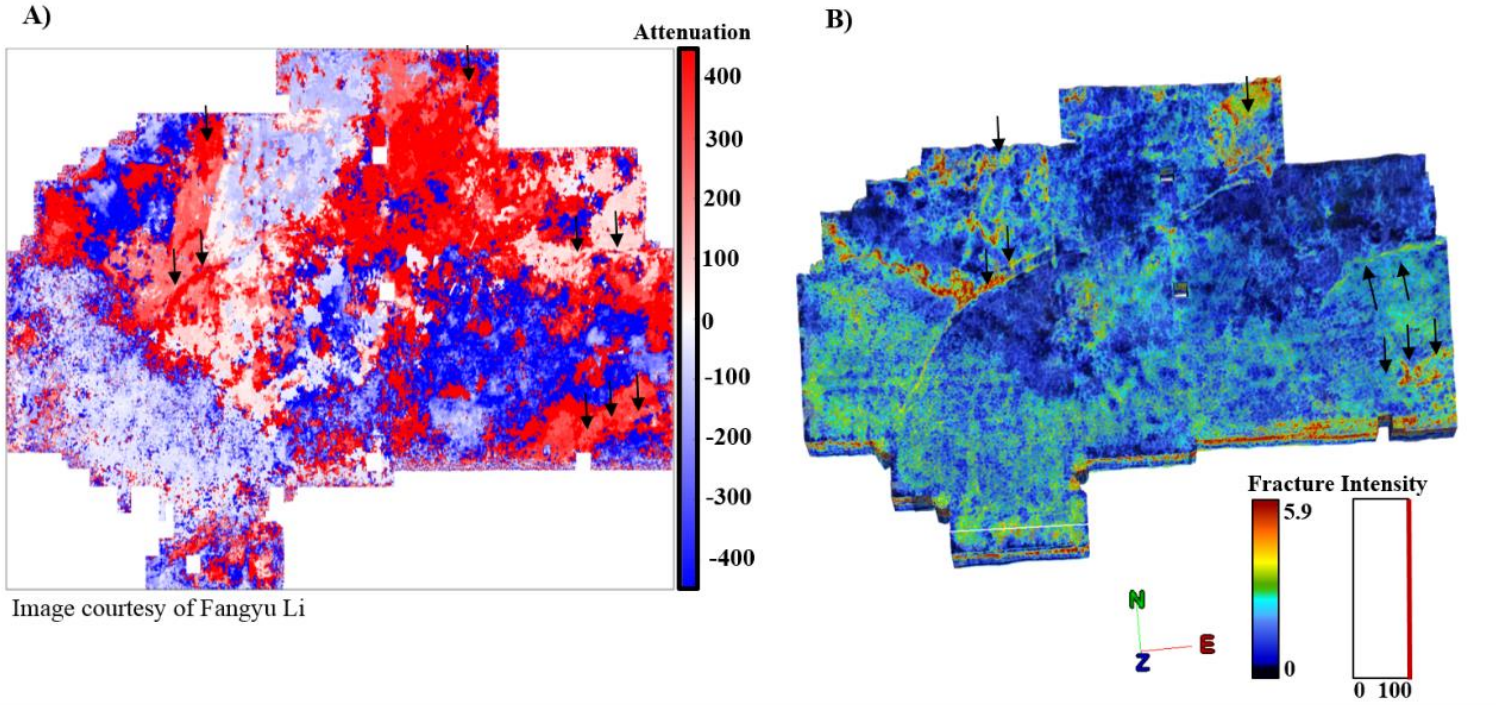

Image courtesy of Fangyu Li

Figure C3. Attenuation was calculated in the first 50 feet of the Mississippian with red areas highlighting areas that seismic energy was highly attenuated. The attenuation includes both intrinsic attenuation and scattering. With small fracture spacing, higher frequencies are attenuated. Arrows highlight areas where high attenuation (A) correlates with higher fracture intensity in the fracture model (B).

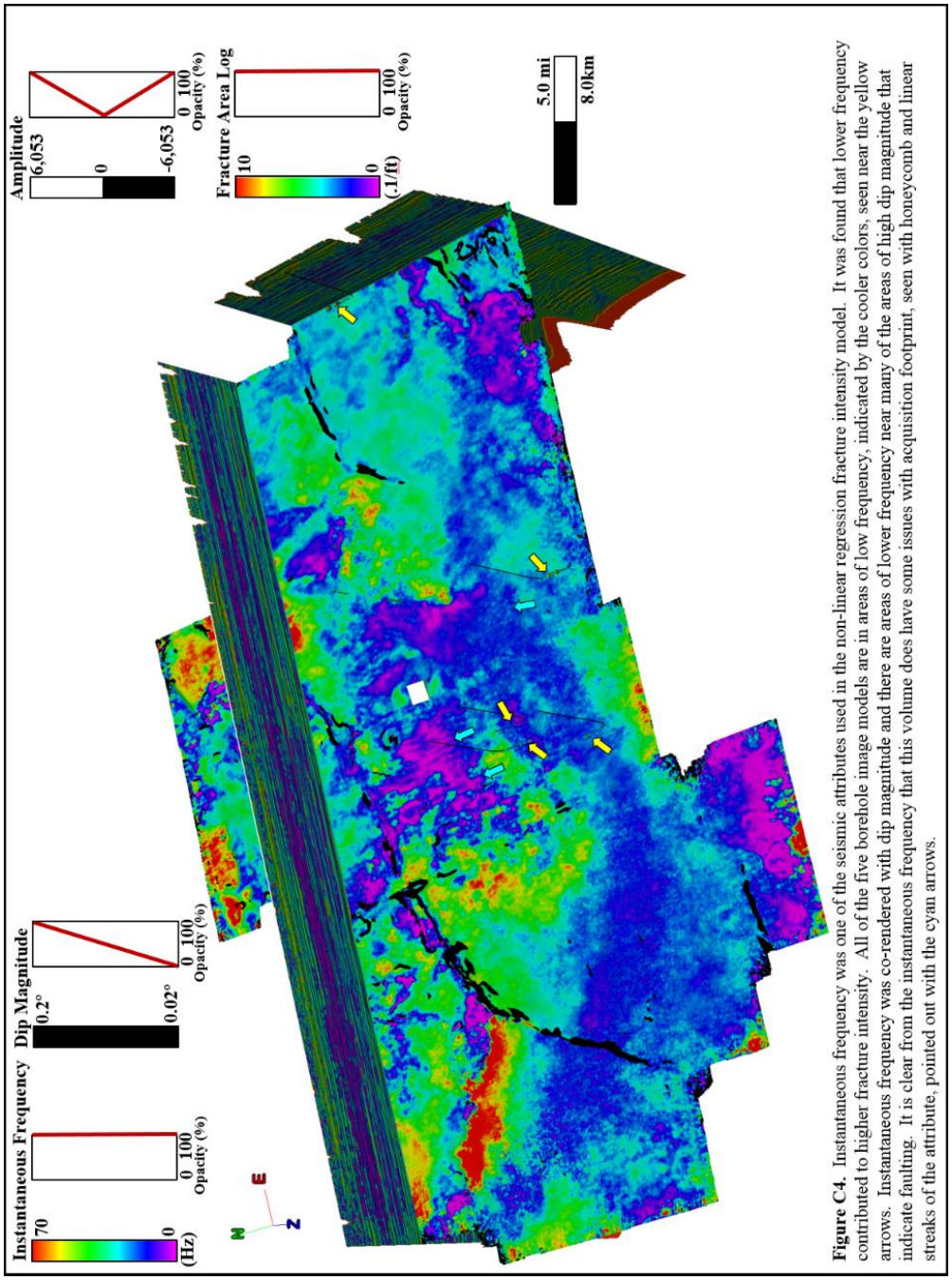

Figure C4. Instantaneous frequency was one of the seismic attributes used in the non-linear regression fracture intensity model. It was found that lower frequency contributed to higher fracture intensity. All of the five borehole image models are in areas of low frequency, indicated by the cooler colors, seen near the yellow arrows. Instantaneous frequency was co-rendered with dip magnitude and there are areas of lower frequency near many of the areas of high dip magnitude that indicate faulting. It is clear from the instantaneous frequency that this volume does have some issues with acquisition footprint, seen with honeycomb and linear streaks of the attribute, pointed out with the cyan arrows.